Machine Learning Focal Mechanism Inversion for Hydraulic Fracturing Induced Earthquakes

by

Megan L. MacDonald

Submitted in partial fulfilment of the requirements for the degree of Bachelor of Science in Earth Science and Physics

at

Dalhousie University
Halifax, Nova Scotia
April 2023

Supervisor: Dr Miao Zhang

Table of Contents

List of Figures

List of Tables

Abstract

Hydraulic fracturing has been found to be a major contributor to the increase in induced seismicity worldwide, with pore pressure, poroelasticity, and coulomb stress transfer identified as the three main triggering mechanisms. However, there is still much to be learned about how these mechanisms operate in hydraulic fracturing-induced earthquakes. The accurate discrimination of these mechanisms requires a complete and precise earthquake catalog, particularly with regards to focal mechanisms, which provide insight into the changes in stress in the area surrounding the hypocenter. Determining the polarities of first motions by hand is a traditional method for identifying earthquake focal mechanisms, but it is not suitable for microearthquakes due to their low signal-noise ratio and the large volume of data involved. Machine learning, on the other hand, provides a reliable and efficient way to classify polarities. Thus, in this study we apply a machine learning-based first motion classifier to automatically invert focal mechanisms for induced earthquakes in the Tony Creek Dual Microseismic Experiment (ToC2ME). We then discuss the accuracy and efficiency of the application of machine-learning-based first motion classifier – DiTingMotion for hydraulic fracturing-induced earthquakes and investigate the associated mechanisms for earthquake triggering during the hydraulic fracturing. We have demonstrated that DiTingMotion is capable of classifying the polarities of earthquake first motions and characterizing focal mechanisms for induced earthquakes. By analyzing three major earthquake sequences during the ToC2ME experiment, our results illustrate that pore pressure, poroelasticity, and coulomb stress transfer can coexist during the hydraulic fracturing, although each may dominate during different stages. We suggest that a comprehensive understanding of geological settings, hydraulic fracturing operations, and the distribution of pre-existing faults/fractures is critical to comprehending the triggering of induced earthquakes. These factors play important roles in seismic activity and comprehending them is essential to mitigate the seismic hazard associated with hydraulic fracturing and optimize shale gas production.

Keywords: Hydraulic Fracturing, Induced Seismicity, Machine Learning, Focal Mechanisms, Earthquake Triggering Mechanisms, Microearthquakes

Acknowledgements

I would like to thank my supervisor Dr. Miao Zhang and the Dalhousie Quake Group for all their assistance and guidance. I have enjoyed learning from each of you and appreciate the time you have taken to answer my questions. A big thank you to Dewei Li for helping me troubleshoot my codes. I would also like to thank Dr. Ruijia Wang for providing me with the ToC2ME data and helpful discussions, and Dr. Alexandre Plourde for reviewing this thesis. This project would not have been possible without those resources and supports.

Thank you to Tarah Wright for all her support and encouragement. Thank you to my family, although I did not appreciate the constant nagging, thank you for believing in me and my ability to get this done. And last but not least, thank you to my amazing friends and girlfriend for putting up with me stressing over this for the past few months. You have been the best support system and have helped relieve so much of my anxiety. Hannah, I am extremely grateful for your patience and for trying to keep me focused and on track when I was struggling to write.

Chapter 1: Introduction

1.1 Motivation

In recent years, hydraulic fracturing has led to an increase in induced seismicity worldwide (e.g., Schultz et al., 2022), especially in Fox Creek, Alberta (e.g., H. Zhang et al., 2019). Although most of these events have been of very low magnitude, less than M 3, some moderate events such as the 2015 Mw 3.9 earthquake (Bao & Eaton, 2016) and the 2016 M_L 4.8 earthquake (Reyes Canales et al., 2022) have caused concern due to their potential for property and land destruction.

Understanding the mechanisms behind earthquake triggering during hydraulic fracturing is of utmost importance. The three proposed mechanisms include pore pressure, poroelasticity, and coulomb stress transfer (e.g., Schultz et al. 2020). Available studies suggested each may play a distinct role in different regions. However, these variations could be caused by different tectonic settings, hydraulic fracturing operations, and, importantly, the incomplete and inaccurate earthquake catalogs and focal mechanism solutions. In this study, we focus on the Tony Creek dual Microseismic Experiment (ToC2ME; Eaton et al., 2018), which is a research-focused field dataset acquired by the University of Calgary consisting of 68 borehole stations within several kilometers, providing an exceptional opportunity for induced earthquake monitoring and analysis.

Using a machine-learning-based earthquake detection and location workflow (M. Zhang et al., 2022), F. Zhang et al. 2022 built a high-precision earthquake catalog consisting of 21,619 events with magnitudes as low as -2.0. The focal mechanisms of earthquakes in the region have not been investigated, with the exception of 530 events that were studied by H. Zhang et al. 2019. Focal mechanisms provide insight into the type of fault slip that occurred and the change of stresses in the region playing an important role in discrimination of triggering mechanisms. Small seismic events can be difficult to analyse using waveform-based inversion because of the high frequencies needed and inaccurate velocity models (Hardebeck and Shearer, 2002). In these cases, polarity-based inversion is often used which requires knowledge of the polarity of the P wave first motion. However, traditional manual methods are not suitable for microearthquakes due to the large volume of data and low signal-noise ratio (Hara et al., 2019). Machine learning algorithms, on the other hand, can process vast amounts of data with high efficiency and reliability, making them a promising approach to solving the focal mechanisms of microearthquakes. However, to date, they have not been utilized in hydraulic fracturing-induced earthquakes.

This study aims to demonstrate the efficiency and reliability of machine learning in classifying the polarities and characterizing the focal mechanisms of hydraulic fracturing-induced earthquakes and investigate the associated mechanism governing earthquake triggering during hydraulic fracturing. This research can provide valuable insights into the mechanisms and risks associated with hydraulic fracturing-induced seismicity.

1.2 Background

1.2.1 Hydraulic Fracturing

Hydraulic fracturing is the process of extracting oil and gas from rocks with low permeability, typically shale, by injecting high pressure fluids into existing small cracks (Schultz et al. 2020)**.** The fluid consists of water, chemicals, and sand grains and the pressure associated with its injection creates new fractures and extends existing ones (Aminzadeh, 2018; Figure 1). Although it has proven to be highly effective and has many economic benefits, it has been associated with several environmental concerns. One of these concerns is the activation of pre-existing fractures and faults, causing what is known as induced seismicity (Cao et al., 2022).

Cases of earthquakes induced by hydraulic fracturing have been well documented in Canada, the United States, and United Kingdom (Bao & Eaton, 2016). Hydraulic fracturing operations are widespread in western Canada, however only around 0.3% are linked to earthquakes with magnitudes greater than 3 (Eyre et al., 2019). Under normal circumstances, these types of operations create small-scale fracture events with very small magnitudes of less than 0 (Schultz et al., 2020)

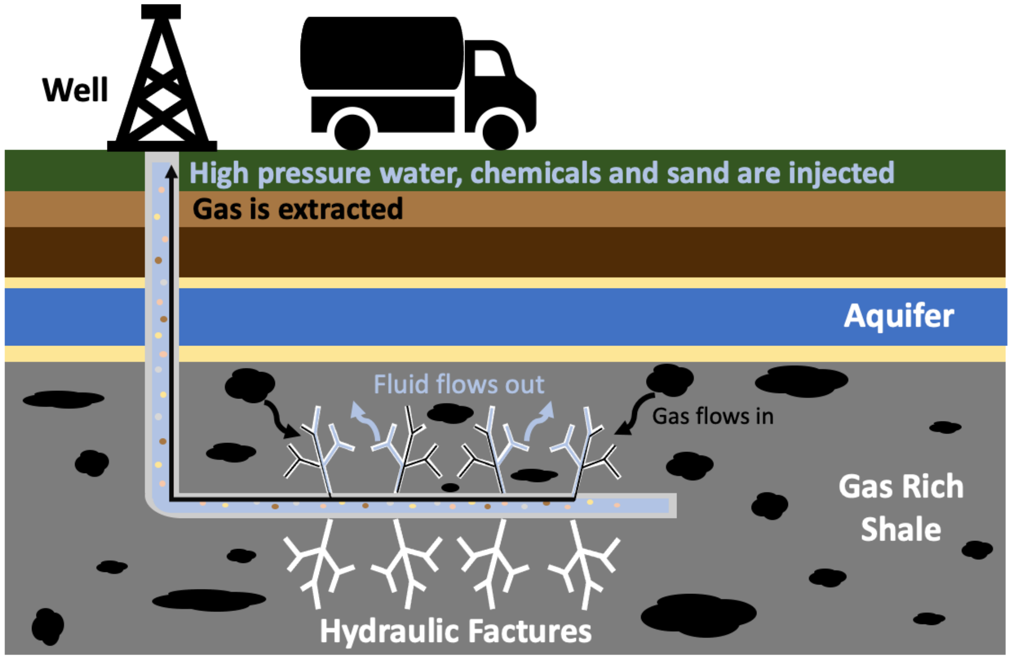

Figure 1: Cartoon illustrating the hydraulic fracturing process.

1.2.2 Induced Seismicity

Induced seismicity has become a growing concern, particularly in regions where fluid injection and wastewater disposal occur (e.g., Ellsworth, 2013). The study of these earthquakes is a fairly new field and there are several unknowns, such as the maximum distances and times between events, as well as the overall long-term consequences. Although the principals of the triggering mechanisms have been established, more research is needed to determine the contributions of each and how they interact during hydraulic fracturing cases. It is important we understand how these principals work so that we can better predict the impacts of induced seismicity.

The three main mechanisms for induced earthquakes are pore pressure, poroelasticity, and stress transfer. Determining which earthquake triggering mechanism is the most dominant is complex. Factors such as local stress, permeability and fracture and fault density need to be considered (Shah & Keller, 2017). An increase in pore pressure or a change in state of stresses can cause reactivation of faults and fractures (Atkinson et al., 2016), which is the most common mechanism in most circumstances. While regional structural geology and stratigraphic formation could also be primary factors in deciding the level of seismicity based on the investigation of hydraulic fracturing-induced earthquakes in western Canada (Wang et al., 2022). Additionally, induced seismicity is greatly influenced by the distance between a drilling site to a nearby fault, where regions with existing fractures have the greater potential to trigger earthquakes (Villa & Singh, 2020). Multiple mechanisms can govern the earthquake triggering in the same region, but with each mechanism dominating an individual stage. For example, Yeo et al. 2020 and Chang et al. 2020 proposed a comparable mechanism to clarify the induced earthquake sequence in the vicinity of Pohang, South Korea. According to their proposal, the foreshock sequence was set off by the activation of critically stressed faults in reaction to the heightened pore-fluid pressure during stimulation. Subsequently, the seismic activity during the later stages, including the M_W 5.5 mainshock, was prompted by the amplified Coulomb stress caused by the foreshock sequence.

1.2.2.1 Pore Pressure

Pore pressure deals with the pressure of fluids between pores in rocks and is a dominant mechanism for hydraulic fracturing induced earthquakes (Ellsworth, 2013; Schultz et al. 2020). The introduction of fluid into a system can alter the state of the principal stresses, which in turn can affect the behavior of a fault block. For a fault block to initiate movement, its shear stress component must exceed the product of its normal stress and the coefficient of friction, which is a constant value determined by the properties of the rock layer. Rocks that contain softer minerals like talc and chlorite typically have lower coefficients of friction than those with harder minerals like quartz and dolomite. The normal stress acts perpendicular to a plane, while the shear stress acts in parallel. When fluid is introduced to the system it reduces the normal stress by applying pressure in the opposite direction, potentially creating favorable conditions for the fault block to become active (Figure 2).

Pore pressures needed to activate faults and fractures are expected to only extend a few hundred meters from injection points for most hydraulic fracturing cases (Schultz et al., 2020). However, it can be argued that pore pressure can still act as a main trigger mechanism at larger distances if we consider the fact that preexisting fractures create more permeable pathways that can extend the effects of elevated pore pressures (Igonin et al., 2021).

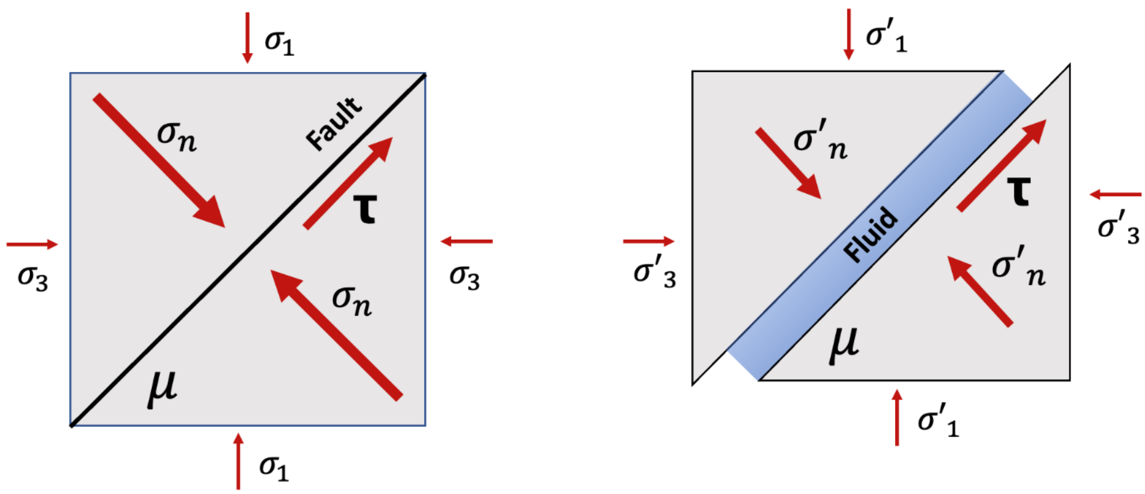

Figure 2: Pore pressure (adapted from Ge & Saar, 2022)
The normal force (σ_n) decreases as fluid is introduced to the system. The fault can be activated if its shear force (τ) is greater than the product of its coefficient of friction (μ) and its normal force. The principle stresses are indicated by σ_1, σ_2, and σ_3.

1.2.2.2 Poroelasticity

The theory of poroelasticity considers the coupling between deformation of a porous medium and evolution of pore fluid pressure, meaning that a change in pore pressure has the potential to deform rocks (Segall & Lu, 2015; Chang & Segall, 2016; Zhai et al. 2019; Figure 3). It suggests that volumetric changes of the pressurized zone can alter the stress field of the surrounding rocks by transmitting elastic forces further distances beyond the hydraulic injection site (Chang & Segall, 2016; Chang et al. 2020). Due to these properties, poroelasticity can be considered as a triggering mechanism at further distances from injection sites compared to simple pore pressure. This is further supported by Goebel et al. 2017, where a 2016 earthquake sequence in Oklahoma was examined and it was suggested that poroelasticity could play a significant role in triggering events at distances greater than 40 km from fluid injection sites.

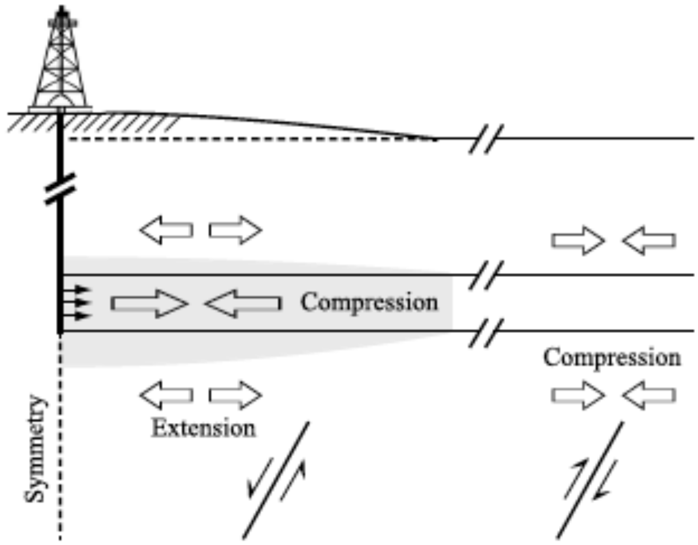

Figure 3: Poroelasticity (Chang & Segall, 2016)

1.2.2.3 Coulomb Stress Transfer

Coulomb stress transfer takes into consideration how earthquakes interact with and influence one another (Sumy et al., 2014; Schultz et al., 2020). It has the possibility to explain events that happen over small and large distances and timescales. When a fault is activated, the stresses surrounding it are changed. Some areas around that fault will experience an increase in stress and others will experience a decrease depending on where the pressure and mass have been relocated (Figure 4). The change in stress can then cause new areas to reach a critically stressed point, and hence trigger an earthquake.

For example, Galderisi & Galli 2020 hypothesized that two parallel fault systems in Italy, Mount Vettore and Norcia, can interact by transferring coulomb stress based on evidence from a Mw 6.6 earthquake in 2016. Medina & Cherkaoui 2017 analysed a sequence of earthquakes that occurred in South-Western Alboran in 2016 and suggested that they may have been triggered by coulomb stress transfer from earthquakes that had happened back in 1994 and 2004.

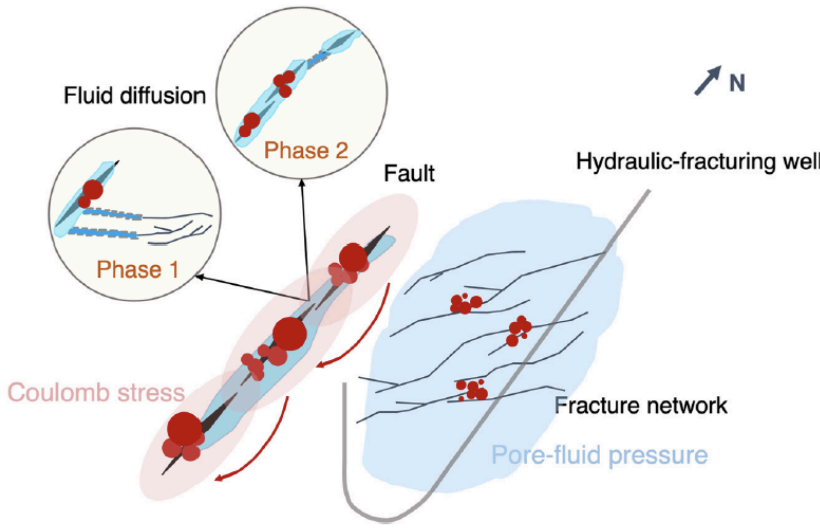

Figure 4: Coulomb Stress Transfer (F. Zhang et al., 2022)

Coulomb stress transfer modelling can provide insight about the likelihood of future earthquakes occurring in the surrounding area. A coulomb stress change map shows regions where stress has increased, which indicate areas more at risk for future earthquakes. Software has been developed to perform these calculations such Coulomb 3, a MATLAB program by Toda et al. 2011 that is widely used by seismologists. Another similar software AutoCoulomb was recently released (Wang et al., 2022), which was programmed with MATLAB, FORTRAN, and SHELL. Analysis of Coulomb stress change can help us to understand the complex interactions between faults and earthquakes, as well as the interactions between earthquakes and each other. It is utilized in conjunction with the other two mechanisms to identify the dominant mechanism.

1.2.3 Earthquake Monitoring and Focal Mechanisms

Seismic monitoring using geophones is one of the key tools for detecting and studying earthquakes. A geophone is a device that measures ground vibrations which are recorded and analysed. Geophone arrays have been shown to be useful for detecting earthquakes as well as map subsurface structures (Trow et al., 2018).

P waves (compression waves) are the first waves to arrive during seismic event detection (Figure 5). Using information on the polarity of the P wave, i.e., whether its first motion is ‘up’ or ‘down’, and location of sensor and source, we can determine if there was initial extension or compression in that direction.

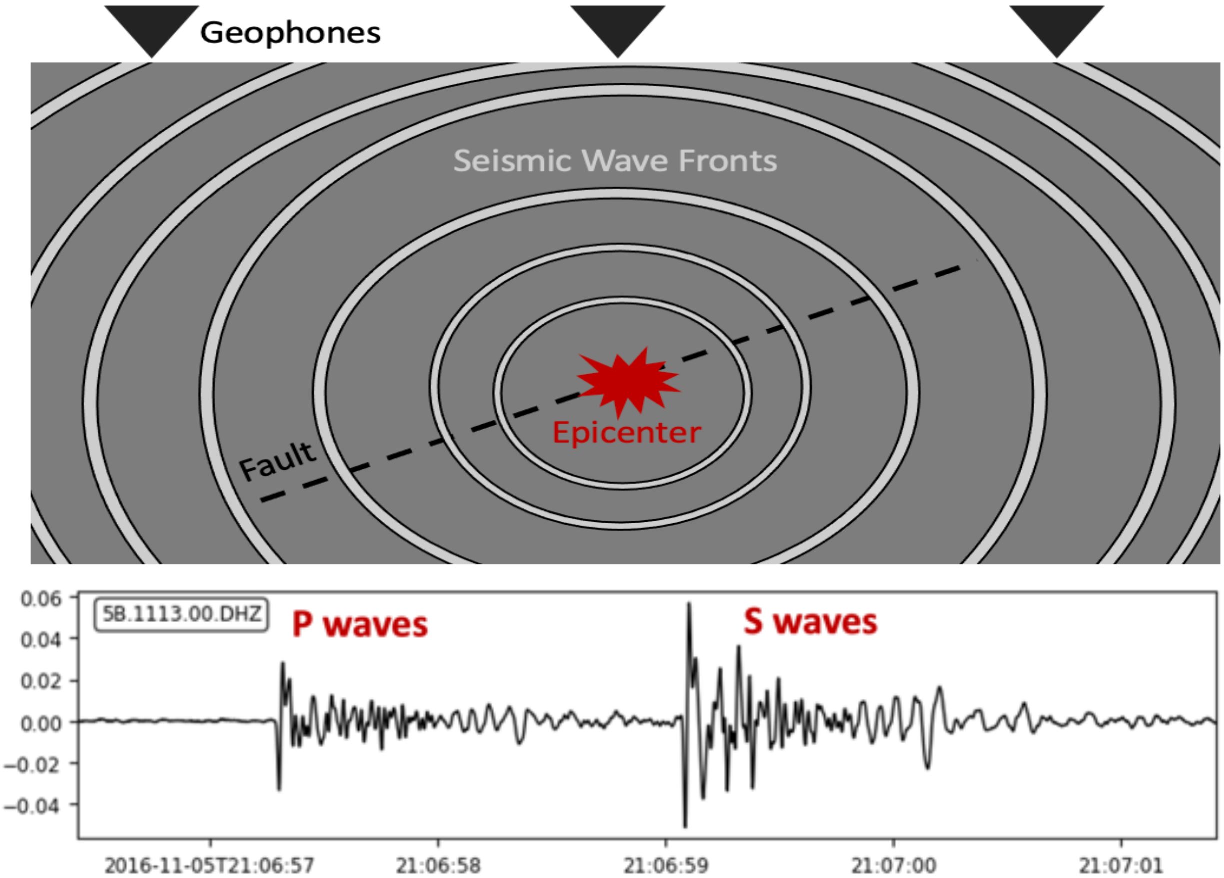

Figure 5: Example seismic waveform with P waves (compression waves) and S waves (surface waves) labeled

Focal mechanisms for small earthquakes provide information regarding the structure and kinematics of faults, as well as the stresses in that region (Hardebeck & Shearer, 2003). This is important for understanding seismic hazards and risk assessments. Focal mechanisms are represented by a sphere with four quadrants; two represent if wave motion was towards the source, and the other two represent if it was away (Hardebeck & Shearer, 2002; Figure 6). Constraining solutions for small earthquakes is an on-going challenge, despite the advancement in technology and equipment (Adinolfi et al., 2022).

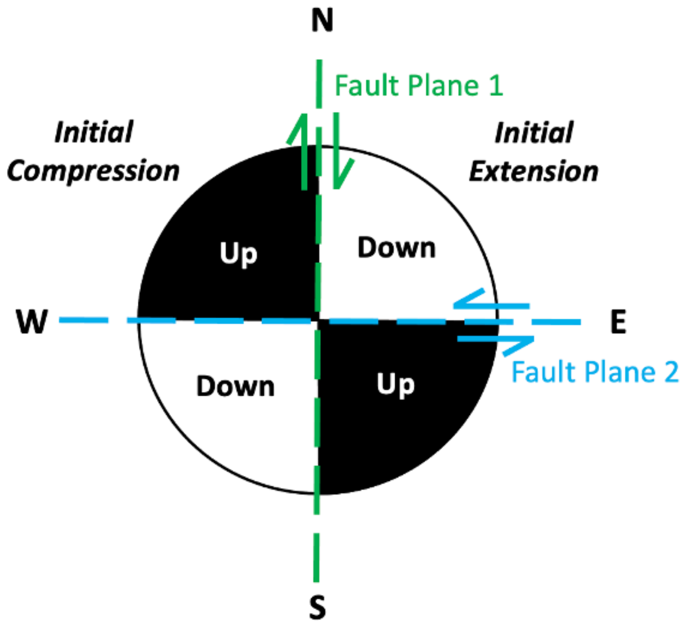

Figure 6: Examples of focal mechanism solutions based on P wave polarities

Focal mechanism solutions provide information about a fault's strike, dip, and rake (Figure 7). Strike is the direction of the line formed by intersection of the fault plane and surface. Dip is the angle between 0-90° that the fault plane is tilted at, measured from the horizontal. Rake is the direction of the fault motion with respect to its strike and ranges from -180 to 180°.

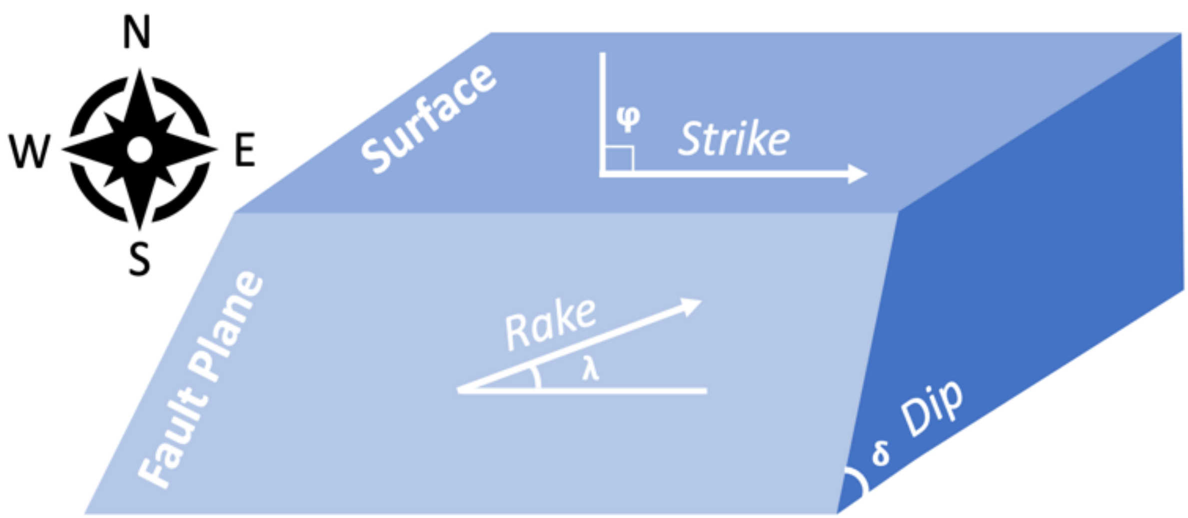

Figure 7: Strike, dip, and rake of a fault plane (adapted from Li 2021)

On a focal mechanism solution 'beachball' plot, the direction of the fault movement can be visualized by moving your hands towards the black regions and away from the white. This means that there are actually two possible fault plane solutions. In order for the correct one to be determined, information is required, for example, the local geology of the area and the distribution of earthquake locations.

1.2.4 Machine Learning

Machine learning has revolutionized the field of seismology by providing new tools in areas such as earthquake detection and signal processing (e.g., Kong et al., 2019). These algorithms allow for large volumes of seismic data to be processed and analysed. For instance, convolution neural networks (CNNs) are a type of machine learning architectural framework and are primarily applied to image or time series data (e.g., Perol et al., 2018). The goal of these networks is to classify the input based on its similarities to other features that have already been determined. CNNs have been used to automatically extract features from seismic data including the classification of P wave first motion polarities.

Several P wave first motion classifiers have been developed and trained with a variety of datasets. Ross et al. 2018 designed a CNN with a training dataset from Southern California Earthquake Data Center that contained 4 847 248 manually determined P wave picks and 2 530 857 first motion polarities. They found that their classifier chose more picks compared to the analysts and that the polarities had a precision of 95%. Their results using machine learning almost doubled the number focal mechanisms for that dataset. Hara et al. 2019 constructed CNN models to determine the polarities from 250 Hz and 100 Hz waveforms. They used waveforms from San-in and Northern Kinki in Japan to train the models, 127 200 waveforms at 250 Hz and 40 169 at 10 Hz. The model demonstrated high accuracy for both 250 Hz and 100 Hz waveform data, with 250 Hz being more accurate by 2.5%. The regional dependency of the model was examined there was found to be no need to retrain the CNN model by regions. Uchide 2020 developed a first motion classifier using a simple neural network model and applied it to analyse 110 000 earthquakes in Japan (Figure 8). The model was trained using 19341 earthquakes with P wave arrival times and polarities. By applying HASH by Hardebeck & Shearer 2002, Uchide was able to successfully determine the focal mechanisms for almost all events in the study area and found that they were mostly consistent with the stress regime on a large scale. Chakraborty et al. 2022 used autoencoder architecture to identify polarities (named: PolarCAP), which was trained using over 130 000 labels from the Italian seismic dataset INSTANCE. They found that PolarCAP slightly outperforms the accuracy of Ross et al. 2018, Hara et al. 2019, and Uchide 2020. Most recently, Zhao et al. 2023 developed a new machine-learning-based first motion classifier – DiTingMotion, which was trained using over 2.7 million samples from the Chinese dataset - DiTing and over 2.4 million samples from the Southern California dataset - SCSM-FMP. They showed that DiTingMotion can reliably identify the first motion polarities with ~97% accuracy compared to the manually picked labels for both training datasets.

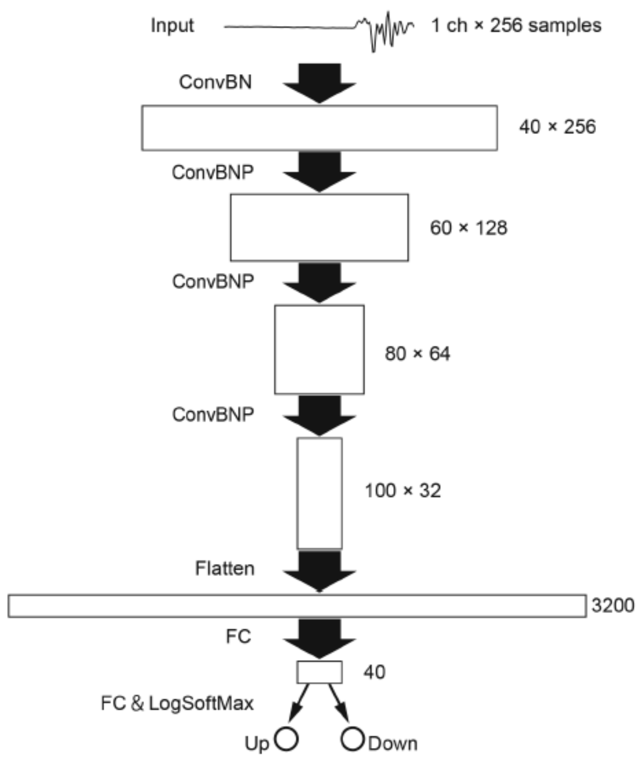

Figure 8: Convolution neural network for first motion classifier (Uchide, 2020)
The input seismogram is convolved through a series of six layers before the first motion is either classified as up or down. See Uchide 2020 for specific layer explanations.

1.3 Study Area

Since 2011, Alberta has experienced an increase in recorded seismic events, many of which are associated with hydraulic fracturing and waste-water injection wells (Reyes Canales et al., 2022). The region of Fox Creek has been of particular interest due to its surge in seismicity and because larger magnitude events (as high as M 4.8) have been recorded in the area (Reyes Canales et al., 2022).

1.3.1 Tony Creek Dual Microseismic Experiment

The Tony Creek Dual Microseismic Experiment (ToC2ME) was led by the University of Calgary (Eaton et al., 2018). It recorded hydraulic fracturing operations at a four-well pad west of Fox Creek, Alberta between October 25th to December 15,th 2016 (Eaton & Eyre, 2018). A combination of a shallow-borehole array of 68 geophones, 6 direct-burial broadband seismometers, and 1 strong-motion accelerometer was used to record seismic activity (Eaton & Eyre, 2018; Figures 9 and 10). Well C was stimulated first, and then remaining wells were stimulated after November 16th, 2016 (Eaton et al., 2018).

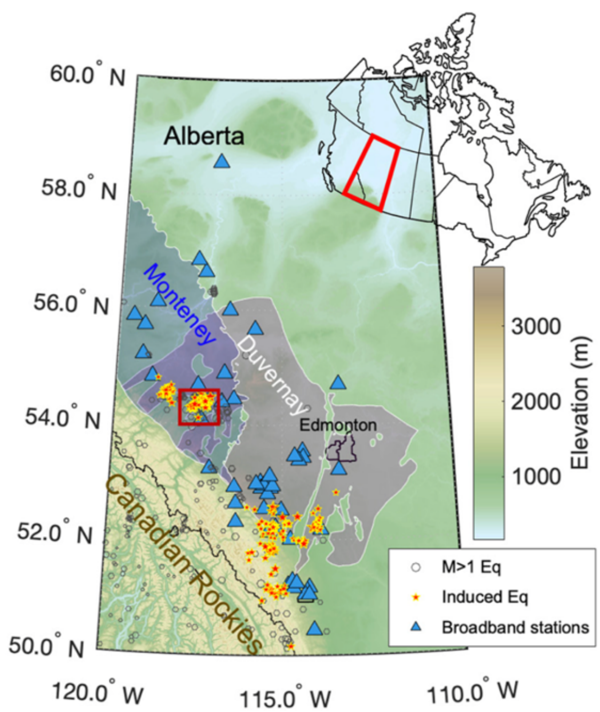

Figure 9: Study area with a large background (F. Zhang et al. 2022)

Several studies have been conducted using the data collected from this project. The moment-tensors for 530 events with M > 0.2 were calculated by H. Zhang et al. 2019. The change in pore pressure that would be required to activate the north-south trending strike-slip faults was also determined in that study. Igonin et al. 2021 showed that pre-existing fracture networks are instrumental for transferring fluid pressure to larger faults, which is where earthquakes occur. These fractures have the potential to increase the volume of rock affected by pore-pressure increase, and in doing so increase the probability of induced seismicity. F. Zhang et al. 2022 used the machine learning seismic detection and workflow LOC-FLOW (M. Zhang et al., 2022) to improve the previous catalog by Igonin et al 2021. This new catalog now contains 21 619 events with more precise locations and timings (Figure 10). Future projects using this new dataset, such as this study, will allow for more detailed analysis of these microearthquakes.

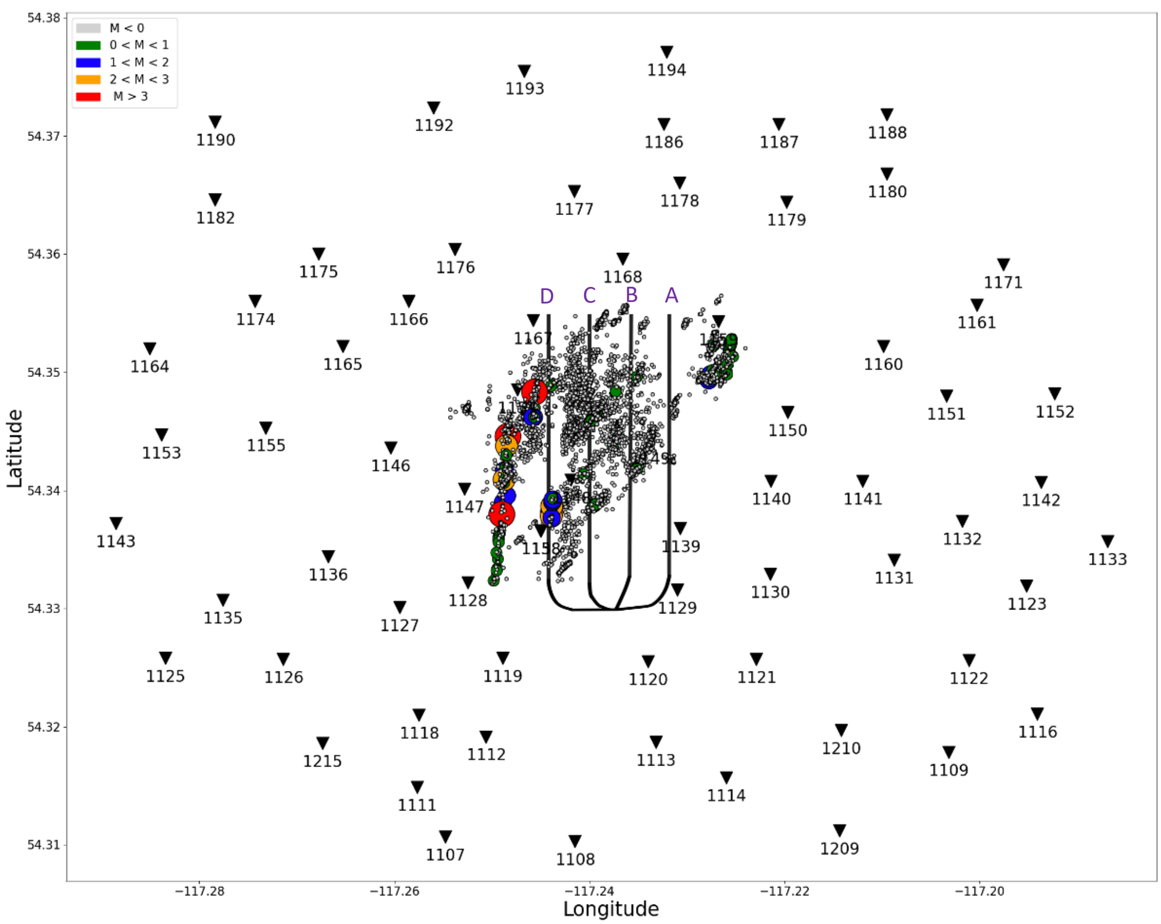

Figure 10: ToC2ME seismic event distribution and station locations

Triangles: seismic stations; Dots: earthquakes colored and scaled by magnitudes; Traces: four injection wells for hydraulic fracturing.

1.3.2 Fox Creek and Duvernay Formation

Hydraulic fracturing at Fox Creek is performed in the Upper Devonian Duvernay Formation, which is a major hydrocarbon source in the Western Canadian Sedimentary Basin (Dong et al., 2019). It contains a significant amount of quartz and limestone (Yehya et al., 2022) and is composed of dark brown bituminous shale and limestone (Switzer et al., 1994). There have been more than 290 horizontal well completions between 2.6 -4.0 km depth in the Fox Creek area, with cases of induced seismicity in the region beginning in December of 2013 (Bao & Eaton, 2016). Overall, the hydraulic fracturing induced earthquakes in the Duvernay Formation have been among the largest magnitudes for this type in the world (Schultz et al., 2018).

1.4 Introduction to the Study

We aim to show that machine learning can be used to reliably and efficiently determine the first motion polarity of P waves and solve for the focal mechanisms recorded through the ToC2ME experiment. Using the data collected by the ToC2ME project, this study will investigate the following questions:

1. *To what extent can machine learning be used to characterize focal mechanisms for hydraulic fracturing induced earthquakes near Fox Creek, Alberta?*

2. *Based on these focal mechanism solutions, which mechanism for induced seismicity (pore pressure, poroelasticity, stress transfer) governs earthquake triggering during hydraulic fracturing?*

The project aims to test the reliability of machine-learning-based first motions for induced earthquakes and improve our understanding of earthquake triggering mechanisms during hydraulic fracturing.

1.5 Summary of Approach

The DiTingMotion machine learning first motion classifier by Zhao et al. 2023 will be applied to the F. Zhang et al. 2022 earthquake catalog. 254 events with magnitudes larger than 0 will be considered to increase the reliability (Figure 11). Using this data, HASH software by Hardebeck & Shearer 2002 will then be used to determine the focal mechanism solutions. From there, the seismic faults will be identified through the combination of earthquake locations and focal mechanism solutions, and the stress changes will be calculated from the Coulomb 3 software. Finally, the potential triggering mechanisms will be analysed based on the stress changes.

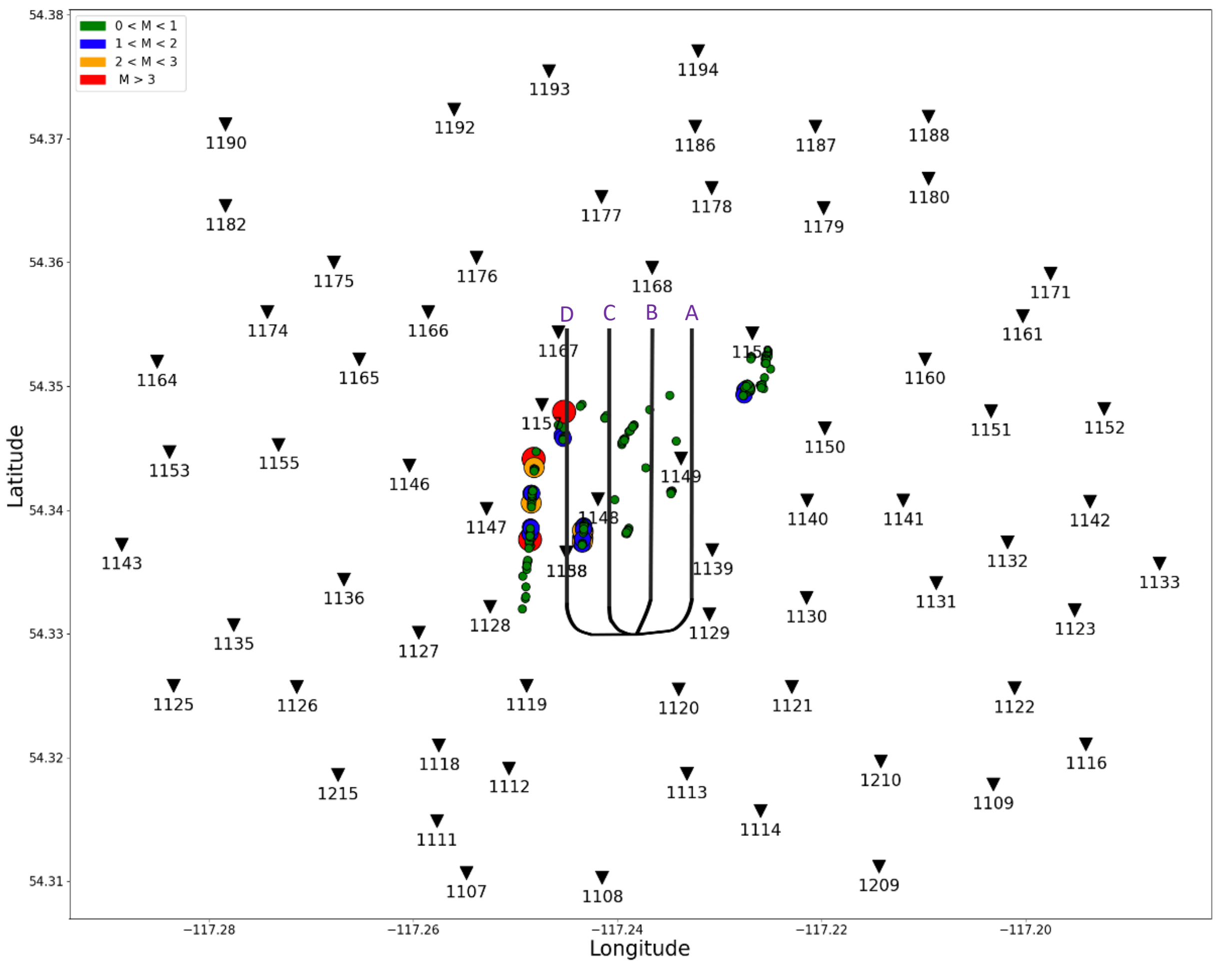

Figure 11: Distribution of the 254 M>0 events used in this study

Chapter 2: Methodology

2.1 Overview

This study aimed to determine the extent to which machine learning can be used to characterize focal mechanisms for hydraulic fracturing induced earthquakes near Fox Creek, Alberta. The DiTingMotion first-motion classifier by Zhao et al 2023 was applied to the F Zhang et al 2022 earthquake catalogue from the ToC2ME project. Analysis was focused on the 254 events with magnitudes greater than zero (Figure 12). The focal mechanism solutions were obtained by running HASH by Hardebeck & Shearer 2002. The solutions were then compiled and plotted in accordance with their location and magnitudes. The Kagan values were calculated in order to compare the angle between these solutions and the moment tensors calculated by H Zhang et al 2019. Coulomb 3.4 software for MATLAB was used to calculate the coulomb stress change for three major event sequences. The triggering mechanisms were investigated and discussed by combining the stress changes of the three major events, the locations of early following aftershocks (from the whole catalog), and the distances from the nearest wells (Figure 12). A detailed workflow can be found in Figure 13.

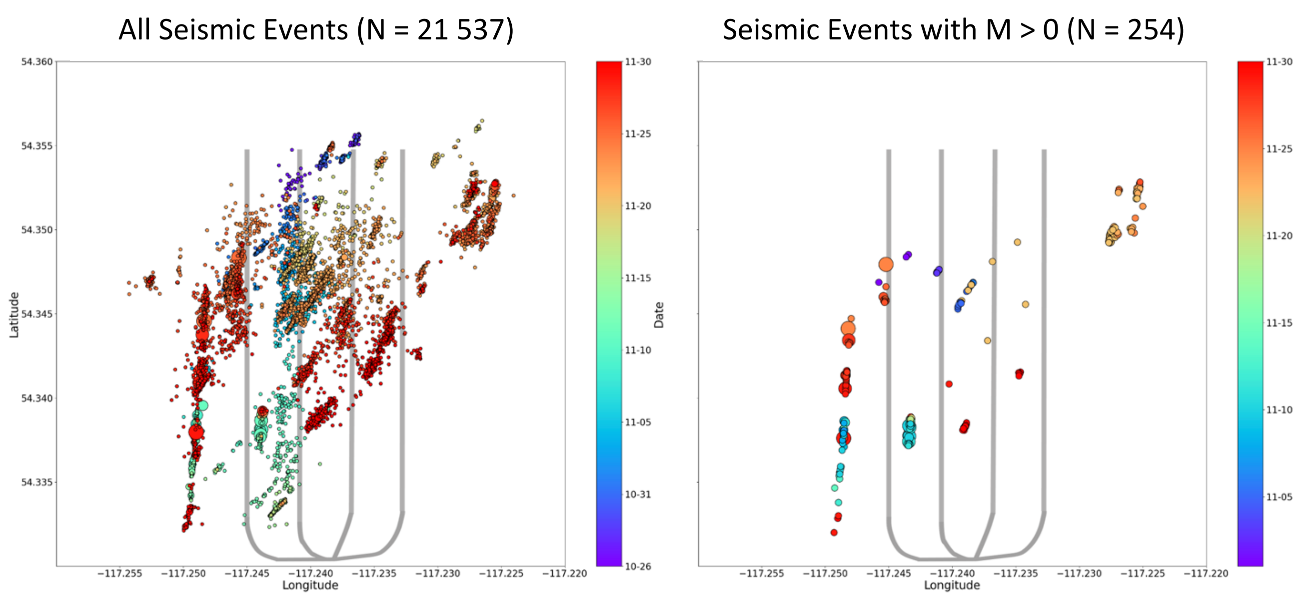

Figure 12: Distribution of seismic events over time

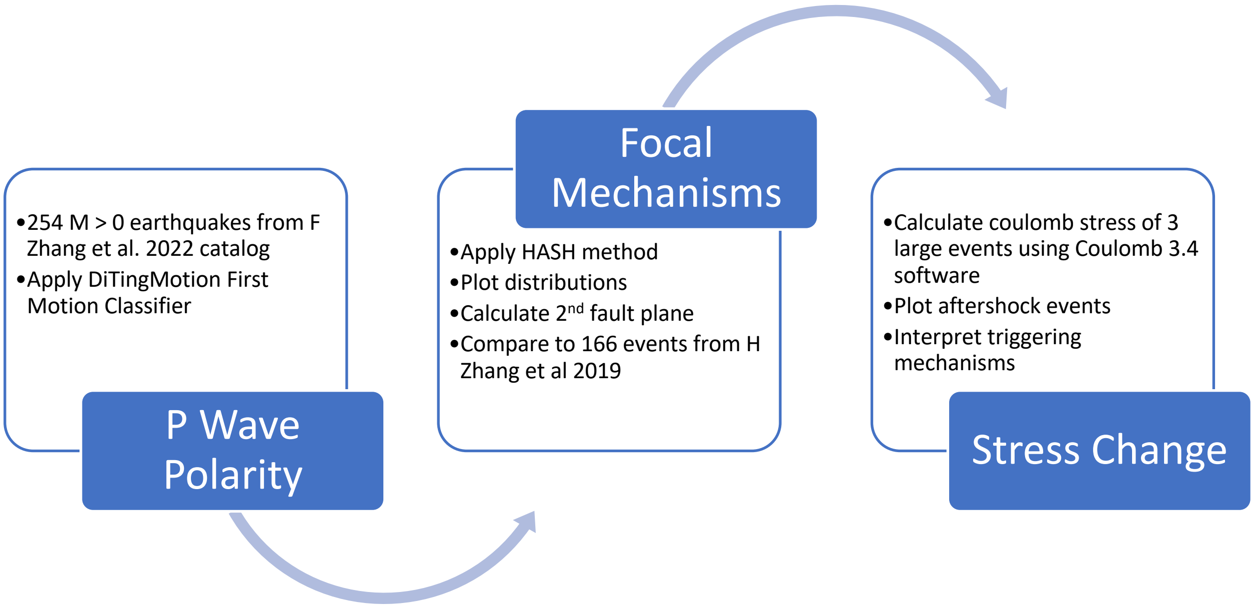

Figure 13: General methods workflow

2.2 DiTingMotion

DiTingMotion is a machine learning P wave first motion classifier developed by Zhao et al. 2023. In this method, a CNN with side-output layers was used for first motion classification (Figure 14). The focal loss was adopted for training to improve the performance, which differs from available other methods that used classic cross-entropy.

The model was trained using two large datasets: DiTing and SCSM-FMP. The DiTing dataset contains 2 734 748 three-component waveforms which correspond to 787 010 events recorded between 2013 to 2020 in China. It includes 641 025 P wave first motion polarity labels for earthquakes with magnitudes ranging from 0 to 7.7 (Zhao et al., 2022). Approximately 2.49 million samples were used for training from the Southern California Seismic Network-First Motion Polarity (SCSN-FMP) dataset (Zhao et al., 2023). They showed that DiTingMotion can reliably identify the first motion polarities with ~97% accuracy compared to the manually picked labels for both training datasets (Figure 15).

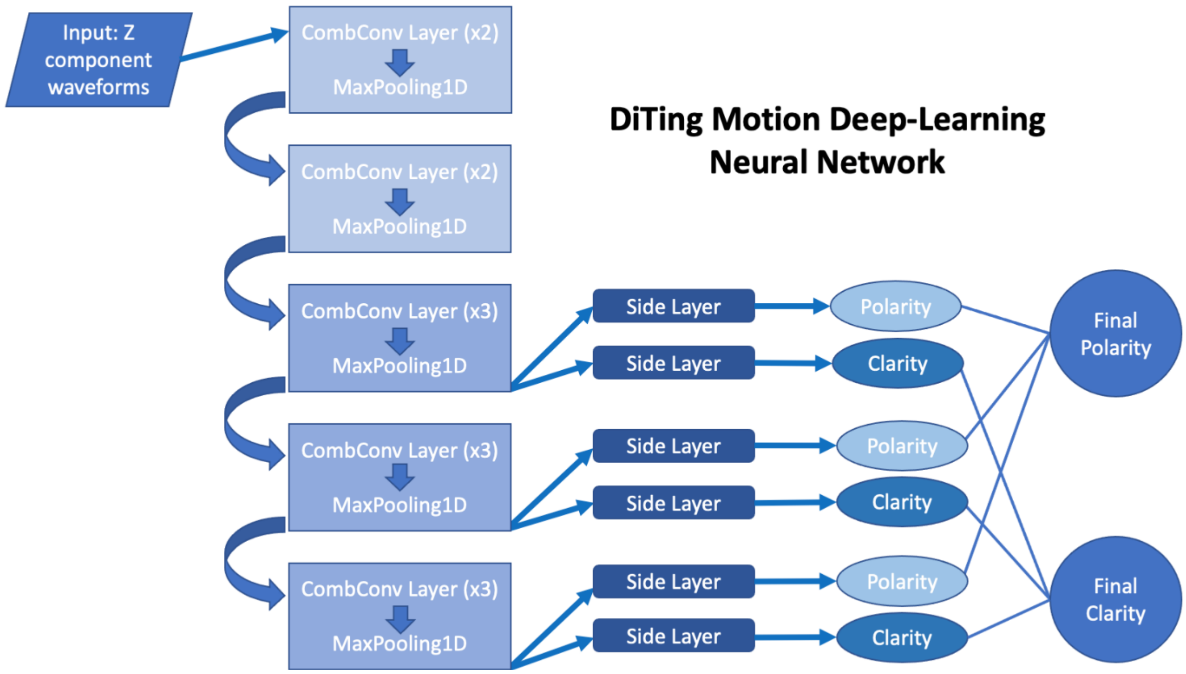

Figure 14: Neural network design for DiTingMotion (adapted from Zhao et al. 2023)

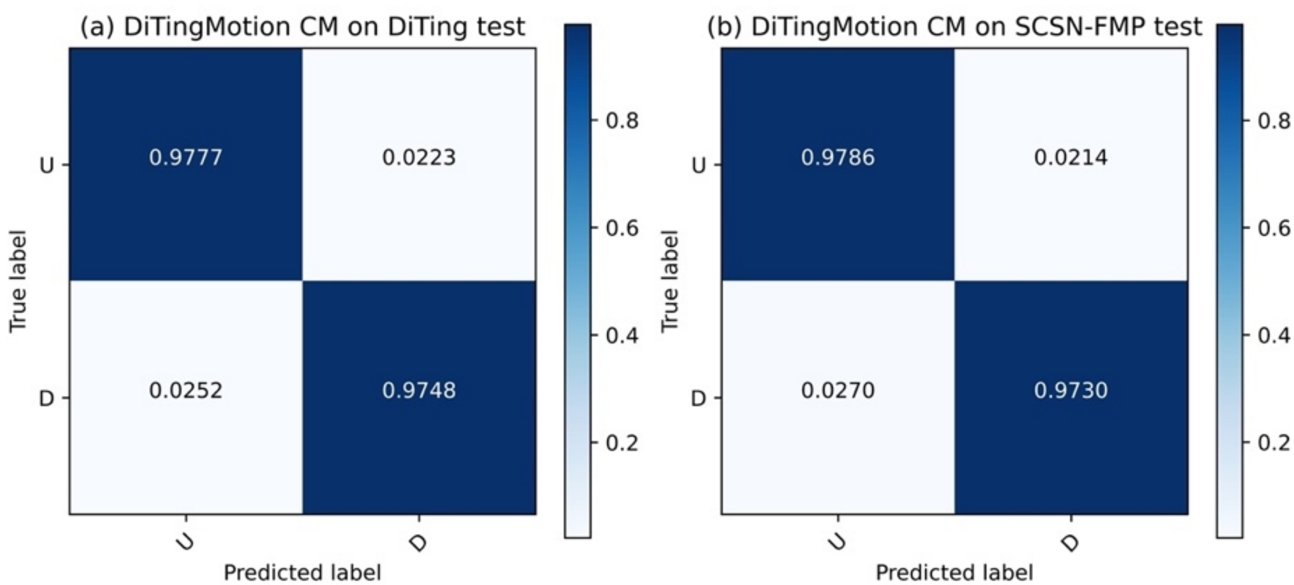

Figure 15: DiTingMotion Confusion Matrix (Zhao et al. 2023)

2.3 HASH

HASH by Hardebeck & Shearer 2002, 2003 is a method used to determine earthquake focal mechanisms from P wave first motion polarities (Figure 16). Different from other methods, HASH considers the uncertainties of first motions, earthquake locations, and velocity models during the focal mechanism inversion. It tolerates false first motions via assuming that a certainty number of false polarities are potentially existed during the inversion. To mitigate the effects from inaccurate earthquake locations and velocity models, HASH randomly perturbates the take-off angles within a small range. The model can be run using Python and the general workflow is illustrated below.

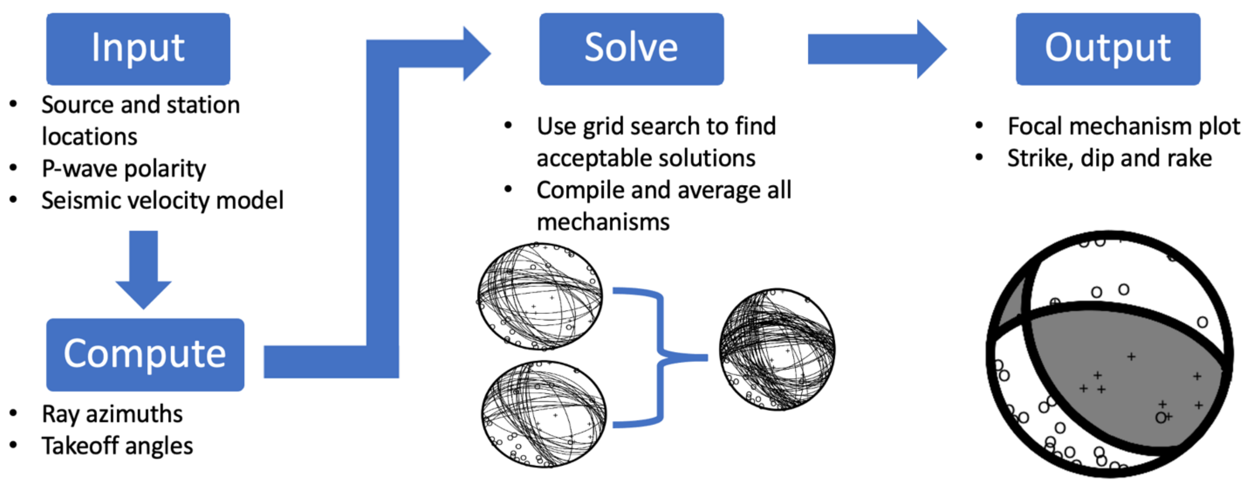

Figure 16: HASH workflow (adapted from Hardebeck & Shearer 2002)

2.4 Procedures and Data Description

2.4.1 Data Preparation

The provided ToC2ME data included: earthquake catalog, phase file for all events, event waveforms, stations IDs and locations, and the seismic velocity model. Many of these needed to be reformatted in order to run DiTingMotion and HASH properly (Table 1). First, the velocity model was condensed to only include depths up of 35 km rather than to 6371 km (the inner core) since the earthquakes occur at depths only a few kilometers below the surface. Only the P wave velocities were considered because we only use the P phases. Next, the phase file had to be converted to DiTing format. At last, the station file had to be converted to a form accepted by HASH.

Data	Format and Example
Waveforms for events M > 0 *Separate folders that contain 207 waveforms for each event*	**Folder Name:** *Year-Month-Day-Hour-Minute-Second* (ex. 2016112512400.760) **File Name:** *StationCode.StationID.DH** where * = 1, 2 or Z. (ex. 5B.1107.DHZ) 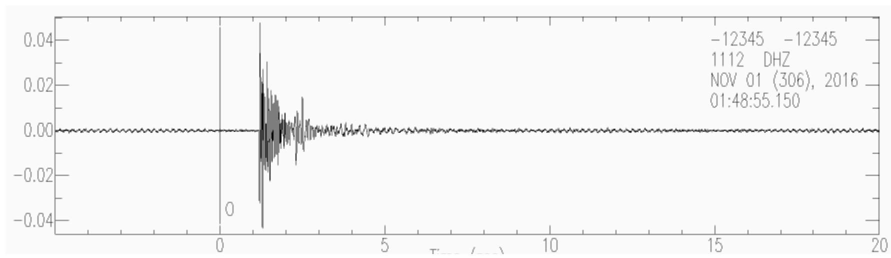

Phase file for all events
Arrival times of either the P or S waves
	# Year Month Day Hour Minute Second Latitude Longitude Depth Magnitude
	Station ID Arrival time ML Pick Probability P or S wave
	`# 2016 10 26 15 42 18.609 54.3620 -117.2411 0.00 2.825`
	`1147 0.8270 0.5530 P`
	`1146 1.5070 0.7390 S`
	`1146 0.7450 0.8060 P`
	`1125 3.1130 0.4830 S`
	`1143 2.5650 0.4740 S`

Event Catalog for events M > 0	*Year/Month/Data Hour:Minute:Second Latitude Longitude Depth Magnitude*
	`1 2016/11/25 21:24:00.760 54.347937 -117.245207 3.285 M 3.21`
	`2 2016/11/29 10:15:25.670 54.337606 -117.248543 3.265 M 3.2`
	`3 2016/11/25 05:31:25.250 54.344124 -117.248193 3.27 M 3.15`

Velocity Model
Time taken for signal to travel through the earth
	Depth, Vp, Vs, Density, Qp, Qs
	`1 0.00 2.5000 1.0345 2.2650 79.0 36.0`
	`2 0.37 3.0521 1.4483 2.2650 79.0 36.0`
	`3 0.41 3.1904 1.5510 2.2650 79.0 36.0`

Stations
Contains station location information
	Longitude Latitude Station Code Station ID File Type Elevation
	`1 -117.201103 54.325600 5B 1122 DHZ 0.937`
	`2 -117.225998 54.315701 5B 1114 DHZ 0.895`
	`3 -117.254799 54.310699 5B 1107 DHZ 0.944`

Table 1: Initial data formats and examples

2.4.2 Running DiTingMotion and HASH

Before running DiTingMotion, several variables had to be changed. First, only vertical waveforms were used because P waves are best displayed in the vertical direction (up and down) due to the large amplitude. Therefore, the code was updated to search only for the event waveforms ending in "DHZ". Second, DiTingMotion was trained using data with a 100 Hz sampling rate whereas the geophones for ToC2ME had a 500 Hz sampling rate. This meant that the bounds to determine the P wave pick window had to be adjusted from ±0.64 to ± 0.128 seconds (i.e., scaled by five times).

The output of DiTing Motion contained the folder ID, date, time, latitude, longitude, depth, magnitude, first motion pick (D, U, or X) and the clarity (I, E or -). The first motion pick indicates where the P wave polarity is "down", "up", or "uncertain". The clarity indicates "impulsive", "emergent", or "uncertain" (Zhao et al., 2023). A script was written to determine the total counts for each pick type for each individual event and for the overall dataset.

The inputs of HASH included the first motion polarities, velocity model station and source locations. These parameters were updated to include the results from DiTingMotion and the re-formatted data from the initial steps. HASH created new folders for each individual event, which contained several files such as the focal mechanism solution plot with the calculated strike, dip, and rake of one fault plane solution.

2.4.3 Plotting Focal Mechanisms

Before the focal mechanisms could be plotted, a new catalog was created to include the fault plane solutions (strike, dip, and rake) from the HASH outputs. This was done by writing a code that stores the Event ID and output in a new file as they are being calculated by HASH and combining this information with the previous catalog by matching the corresponding IDs. To plot the focal mechanisms a Python script was written using the open-source seismological signal processing library ObsPy. The 'beachballs' were plotted based on their location (longitude, latitude), and were scaled and coloured based on their magnitude. The location of the hydraulic fracturing well site was plotted as well. Based on the focal mechanism solutions, larger fault structures can be defined. If we observe that there are multiple mechanisms in a row with a similar orientation, we can assume that there is a fault system that runs along that region.

2.4.4 Calculating Kagan Angles

Kagan angles are used to describe the 3-dimensional angle between focal mechanism solutions. Essentially, the algorithm defines at what angle the Solution 1 would be to be rotated to match Solution 2 (Kagan, 2007). Knowing this value allows us to compare how similar solutions are to each other.

H Zhang et al. 2019 calculated the moment tenors for 530 ToC2ME events. A moment tensor is a method of representing focal mechanism solution in the form of 3x3 matrix, including both double-couple components (i.e., pure shear rupture along the fault) and non-double-couple components (e.g., crack opening or multiple faults are simultaneously ruptured). It was found that a total of 165 events corresponded with my set. In order to compare the two datasets, the moment tensors were converted to two fault plane solutions (strike, dip, and rake) using Pyrocko tools, which is an open-source Python library for seismology. The second fault plane solutions for my focal mechanisms were also calculated using a similar method. The Kagan angles between a similar set of fault plane solutions were then determined using the Kagan function from the SeismoTectonic Regime Earthquake Calculator (STREC) package for Python.

2.4.5 Calculating Stress Changes of Major Events

The seismic data from F Zhang et al. 2022 was used to plot the distribution of magnitudes over time for over 21 000 events. This was used to visualize the aftershocks after larger magnitude events. A selection of three major event sequences were chosen, which cover the early stimulation stage along well C and the late situation stage along wells A, B, and D. Scripts were written to isolate and plot the earthquake locations between these time windows. Using Coulomb 3.4 software for MATLAB, the coulomb stress changes were plotted for the largest events in the chosen sequences. The well site and earthquake locations were plotted overtop the stress change plots and were examined to suggest the possible induced seismicity trigger mechanisms at play. When examining the final outputs, the following general ideas were applied to aid with interpretation:

1. Earthquakes induced by coulomb stress transfer are most likely to occur in the warmer coloured regions on the graph, which are regions that represent increased stress after the initial event. These events can occur over short and long distances from the well site.
2. Pore pressure increases are typically most significant near the well site, therefore events clustered along the wells are likely a direct result of fluid injection by hydraulic fracturing operations with some potential effects of coulomb stress transfer if also located in a zone of increased stress.
3. Events which occur further from the well site but not within a zone of increased stress may be a result of poroelasticity.

Chapter 3: Results

3.1 DiTingMotion Polarities

A total of 14 791 P wave first motion polarities were determined using DiTingMotion, and 5.5% of these were classified as 'undetermined'. 50.6% were labeled as "Down" and 43.9% as "Up" (Table 2).

Down Pick	Up Pick	Undetermined Pick	Total Picks
7 480	6 492	819	14 791

Table 2: Results of DiTingMotion polarities

The total pick counts for each event were calculated and their distributions were plotted (Figure 17). The averages were rounded to the closest integer, with an average of 58 polarity picks per event. There were more 'Down' picks with an average of 30, compared to 'Up' which had an average of 26. The average number of "Undetermined" picks was found to be 3. See Appendix B for full descriptions of each event.

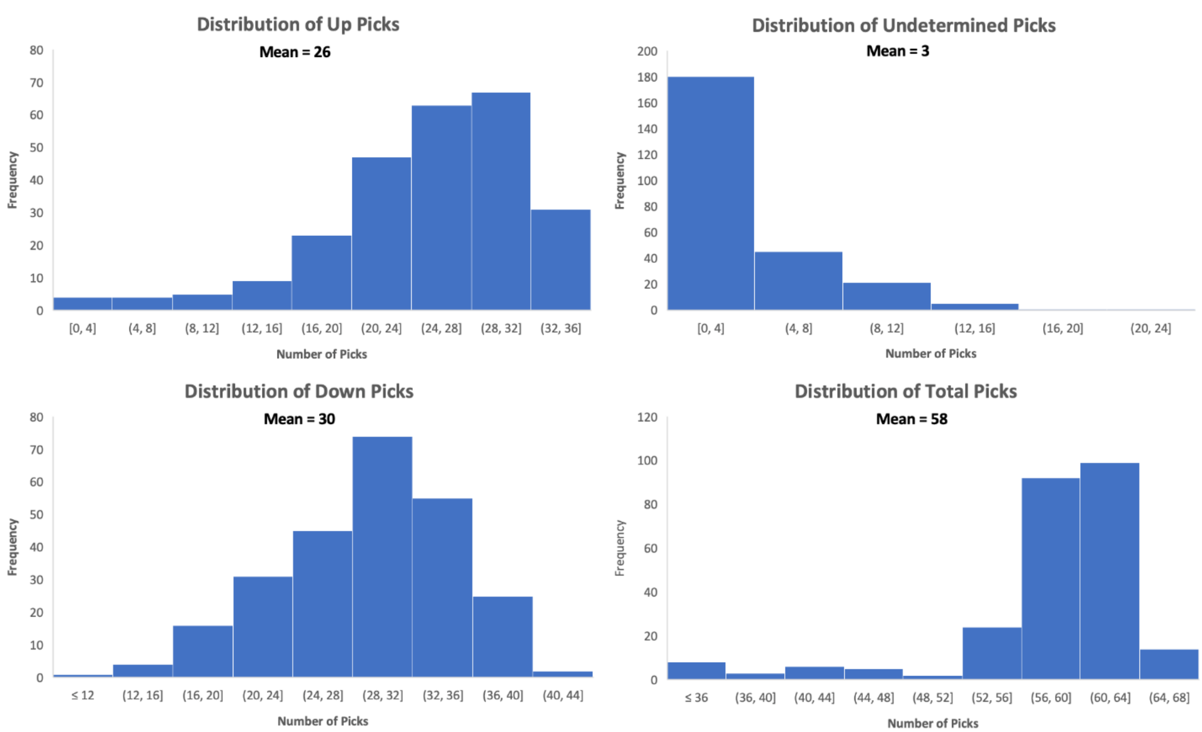

Figure 17: Distribution of up, down, undetermined, and total picks per event

DiTingMotion produced a figure for each event which contained information on the polarity and clarity pick for each station (Figure 18). The waveform displayed has been scaled and stretched to focus in the first motion. This allowed for visual confirmation that the “D” or “U” pick matches the waveform. For detailed outputs for each event, please refer to the supplementary material in Appendix G.

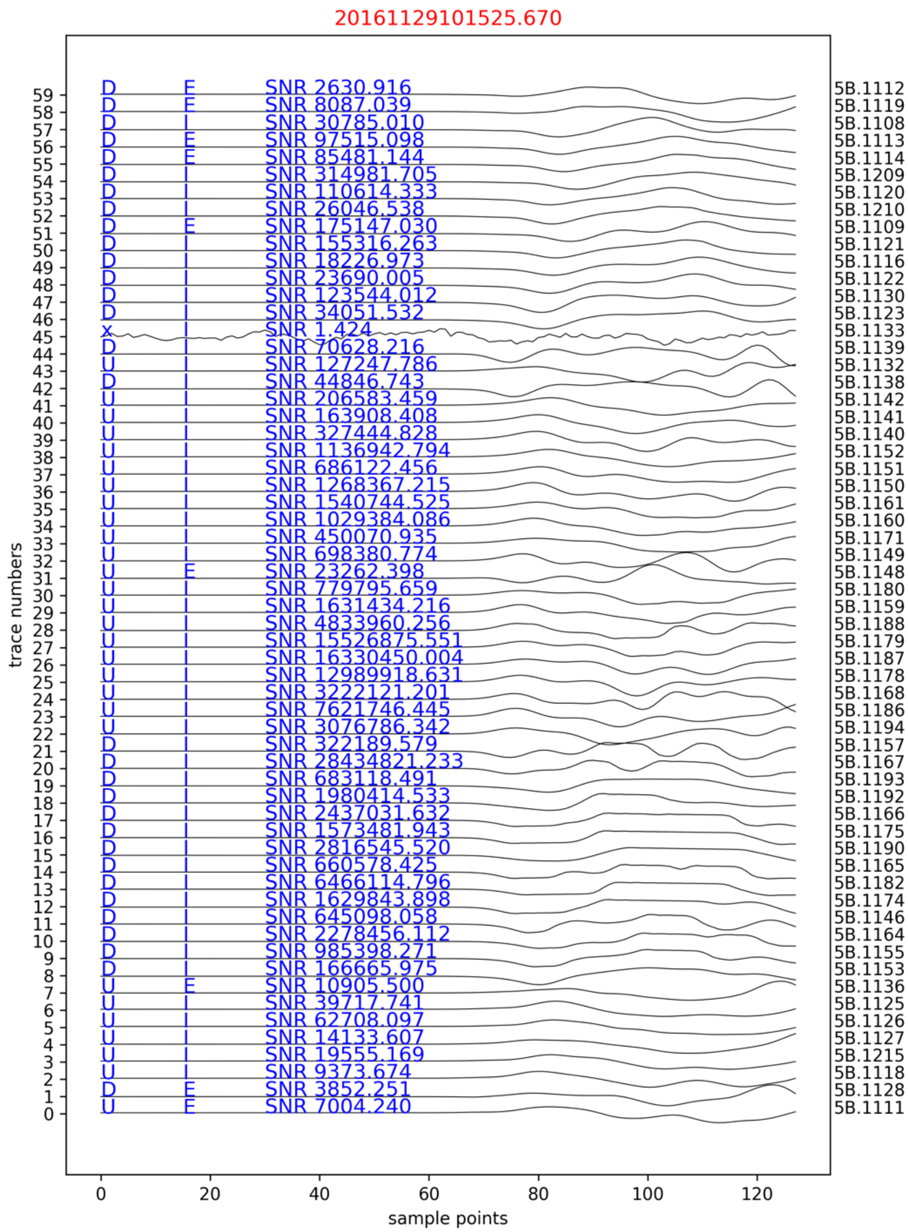

Figure 18: Example of DiTingMotion output

D = Down, U = Up, X = Undetermined

SNR refers to the Signal Power/Noise Power.

3.2 Focal Mechanisms

3.2.1 Distribution of Focal Mechanism Solutions

Focal mechanism solutions were plotted based on their locations and were scaled and coloured according to their magnitudes (Figure 19). The hydraulic fracturing well was also plotted for reference. See Appendix B and C for detailed results for individual focal mechanisms.

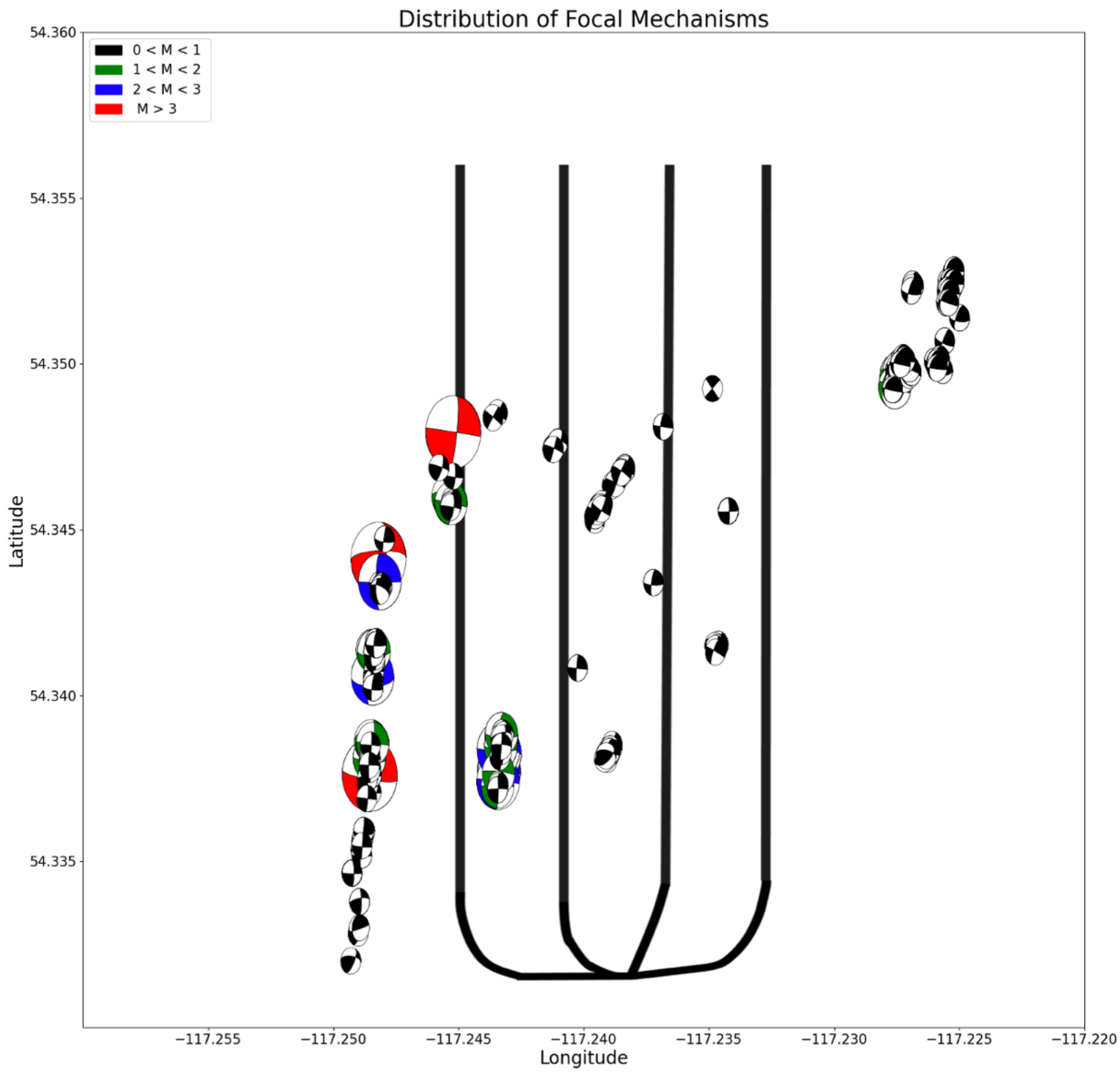

Figure 19: Distribution of focal mechanism solutions

3.2.2 Distribution of RMS Values

HASH calculated the root mean squared (RMS) values for each input, which measures the uncertainty in degree from the averaged solution (HASH selects the best solution from a solution pool). The distribution of the values was plotted, and the mean was found to be an RMS of 10 (Figure 20). A list of the 17 events with RMS values higher than 25 (Table 3) was compiled and then plotted relative to the well and stations for further analysis (see Section 4.2.2).

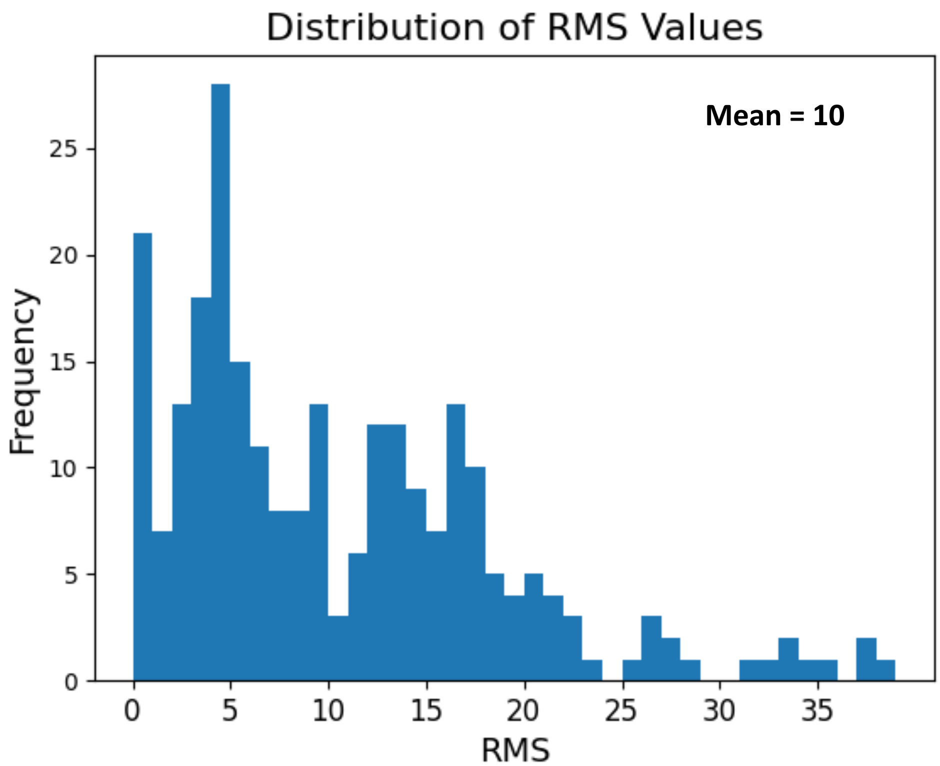

Figure 20: Distribution of misfit root mean squared values

Events with RMS values greater than 25	
20161105170516.800	20161130190244.000
20161119104654.440	20161130212808.740
20161122171549.980	20161130215417.720
20161124114121.020	20161130194507.780
20161122112111.190	20161130193138.840
20161130222325.340	20161130192340.520
20161130202045.220	20161130184305.740
20161130191429.200	20161130224708.240
20161130231829.880	

Table 3: List of events with RMS value above 25

3.2.3 Distribution of Strike, Dip, and Rake

The distribution of strike, dip, and rake values for both possible focal mechanisms were plotted and analysed (Figure 21). For fault plane 1, two strike clusters were observed. The first cluster ranged from 85-120° and the other from 255-305°. For rake, values were clustered between -110 – -180° and 110 - 180°. The dip angles average 77°. For fault plane 2, again two clusters for strike. The first ranged between 0-60° and the other from 180-215°. The average dip angle was 60° and average rake was 14°. See Appendix F for full description of the possible fault plane solutions for each event.

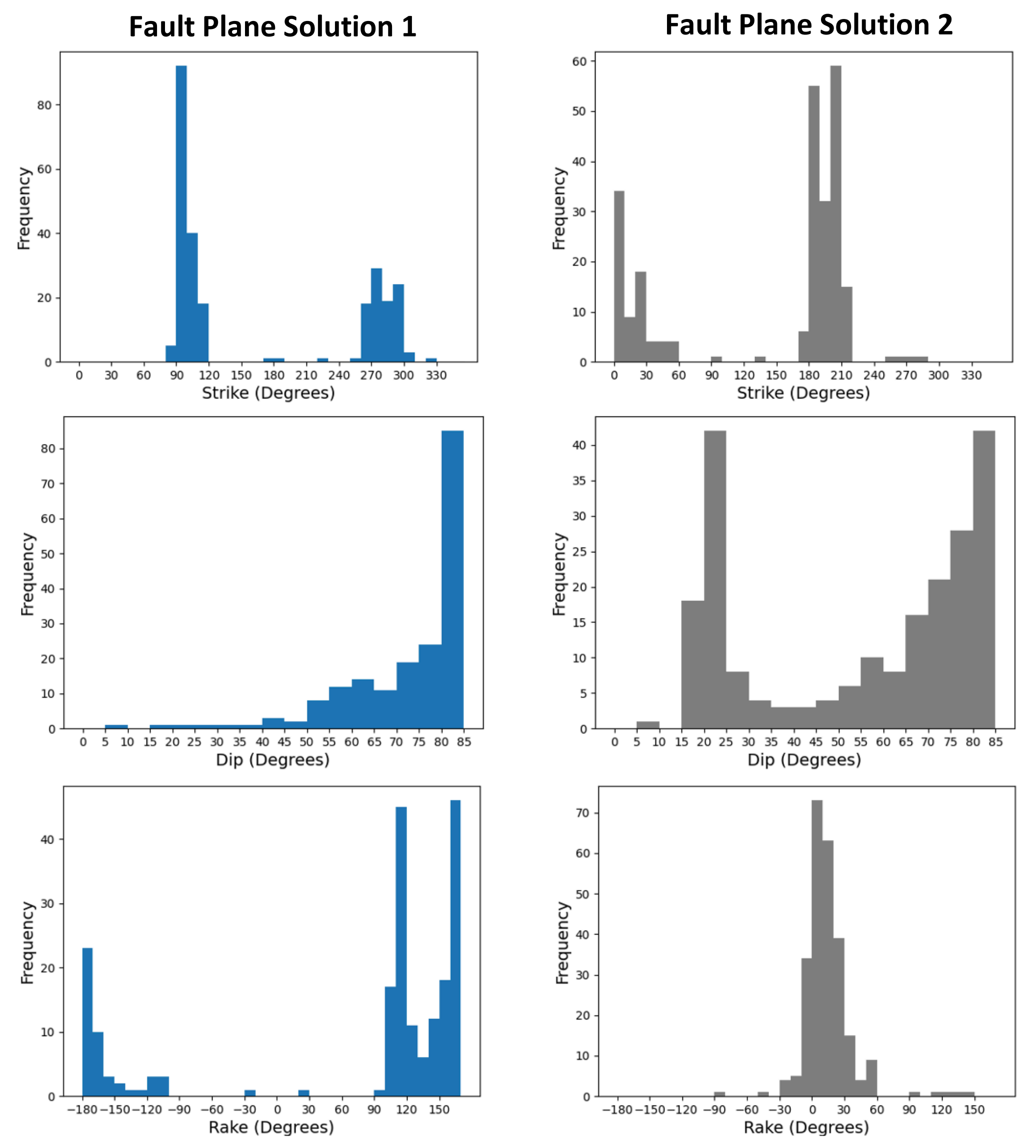

Figure 21: Distribution of strike, dip, and rake for both possible fault plane solutions

3.2.4 Comparison to H Zhang et al 2019 Moment Tensor Solutions

The distributions focal mechanism solutions for the 166 common events are displayed in Figure 22 and Figure 23

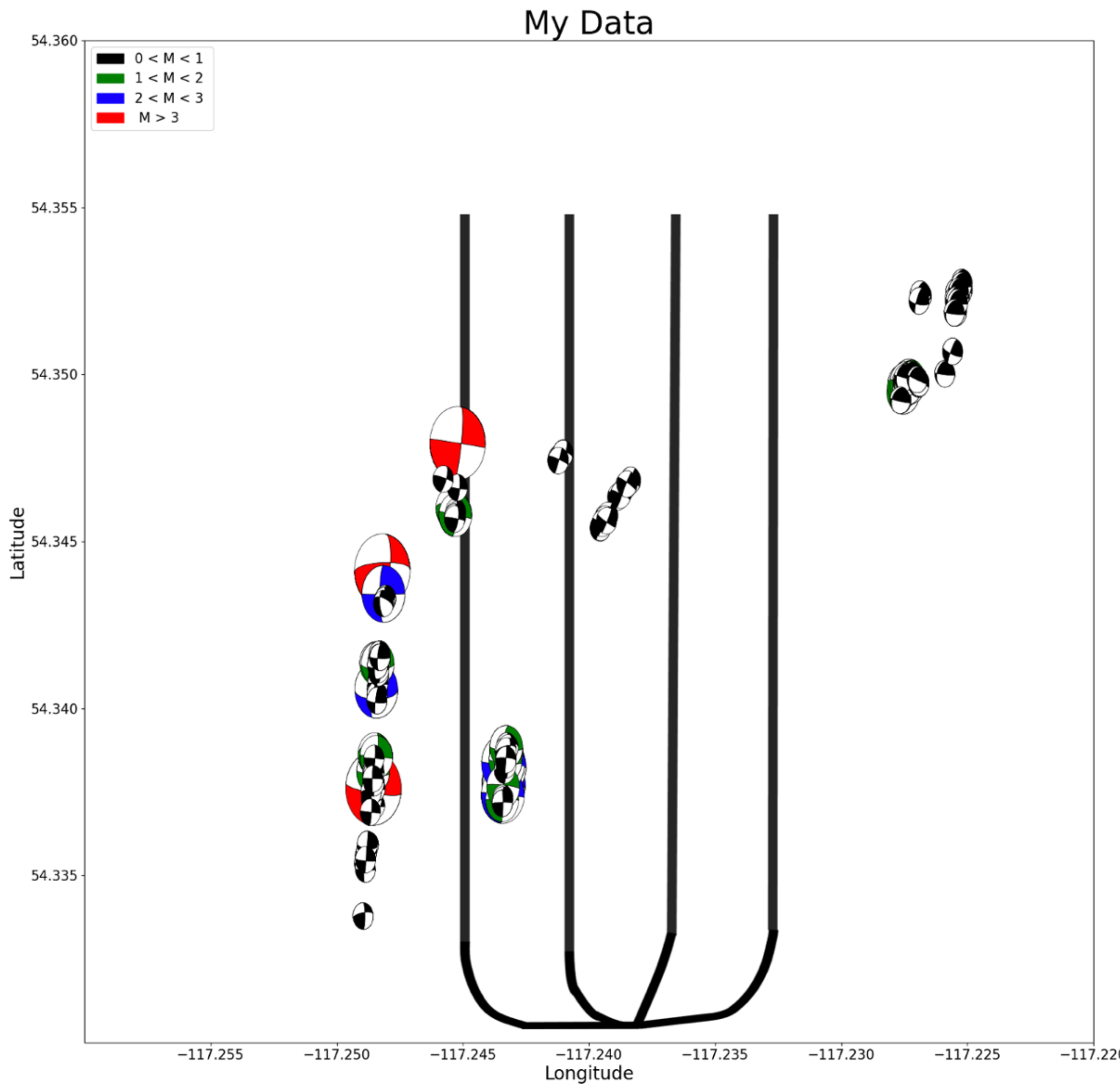

Figure 22: Focal mechanisms used for comparison

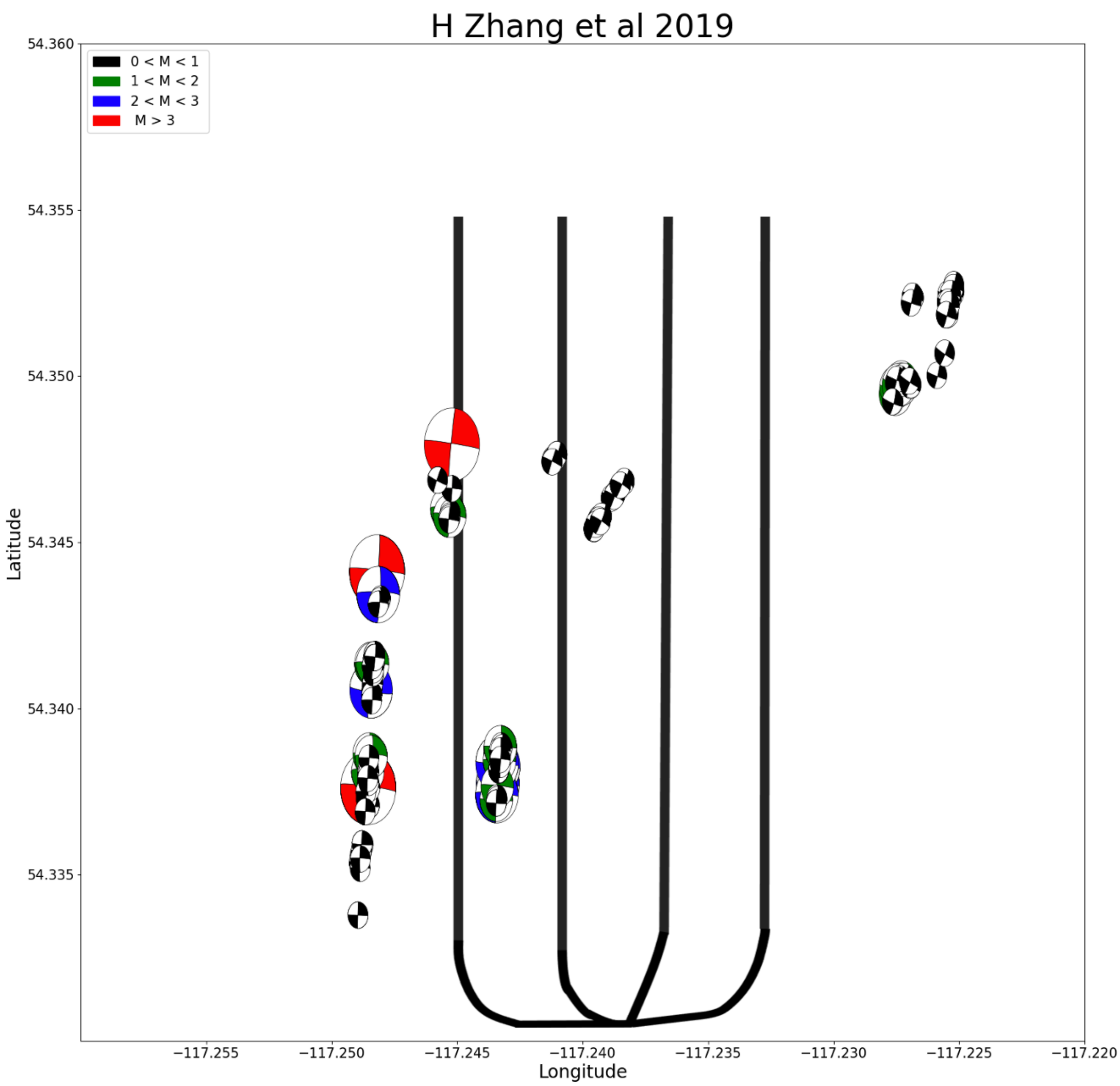

Figure 23: H Zhang et al focal mechanisms used for comparison

3.2.4.1 Distribution of Strike, Dip, and Rake

The distributions of strike, dip, and rake were plotted for both fault plane solutions for 166 common events between my data and the moment tensor data from H Zhang et al. 2019.

Fault Plane 1

There is similar clustering for strike values, with the two main groups being between 85- 125° and 270 - 300° (Figure 24). My data has a spike around 90-95°, whereas theirs has one around 270-275°. For dip, both datasets are more concentrated between 80-90°, although my dataset has a greater variation. As with strike, the clustering of rake values can be broken into two main groups. The lower end group is between -180 - -150°, with their dataset having a higher spike between -170- -80°. The upper group ranges from 100-180° for my set and is highly concentrated between 170-180° for their set.

Fault Plane 2

Again, we observe two cluster groups for strike (Figure 25). My first cluster is between 0-30° whereas theirs is more tightly clustered between 0-10°. The second cluster is between 170-220° for both, with theirs have a larger spike between 170-180°. My dip angles are spread out with no main spike, compared to theirs which as a main spike between 85-90°. For rake, my angles are concentrated between -10 - 30° and theirs are heavily concentrated around -5 - 5° with some variations.

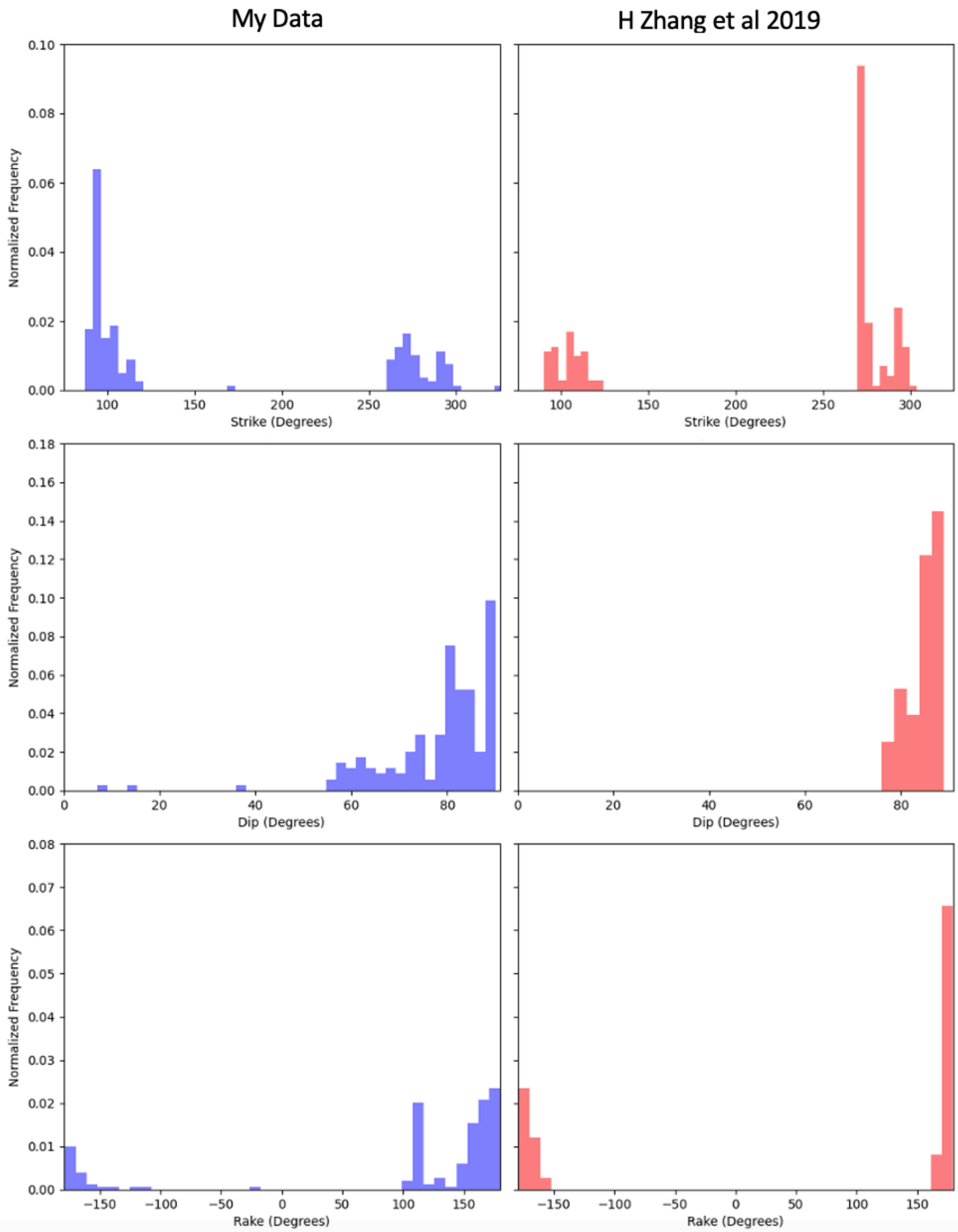

Figure 24: Fault plane 1 comparison of the strike, dip, and rake with H Zhang et al 2019

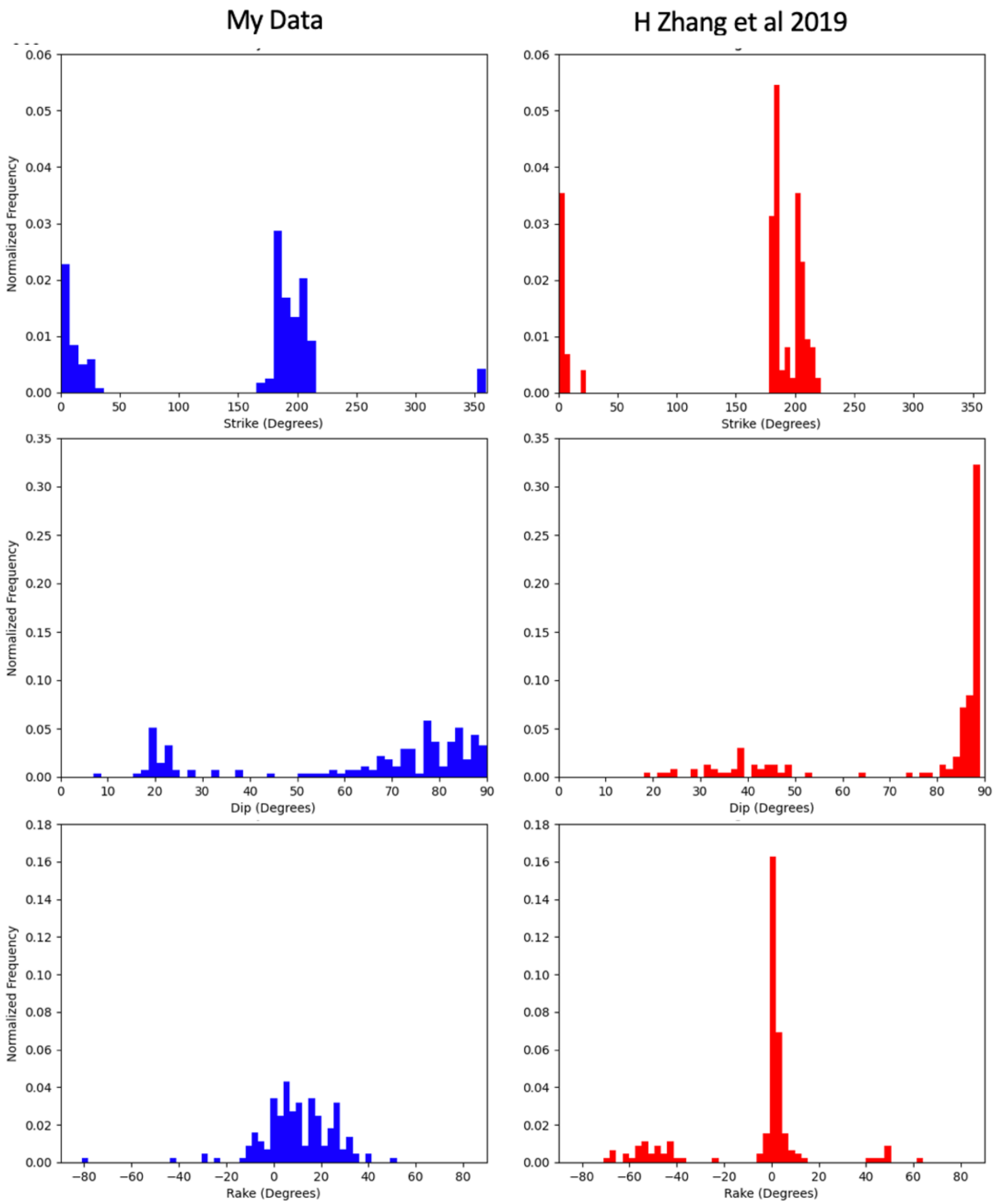

Figure 25: Fault plane 2 comparison of the strike, dip, and rake with H Zhang et al 2019

3.2.4.2 Kagan Values

The Kagan angles for fault plane 2 (equivalently to fault plane 1, thus either one is fine for analysis) were calculated for the 166 common events between both datasets and the distribution was plotted (Figure 26). The mean value was found to be 31.72 °. See Appendix E for Kagan values for each individual event.

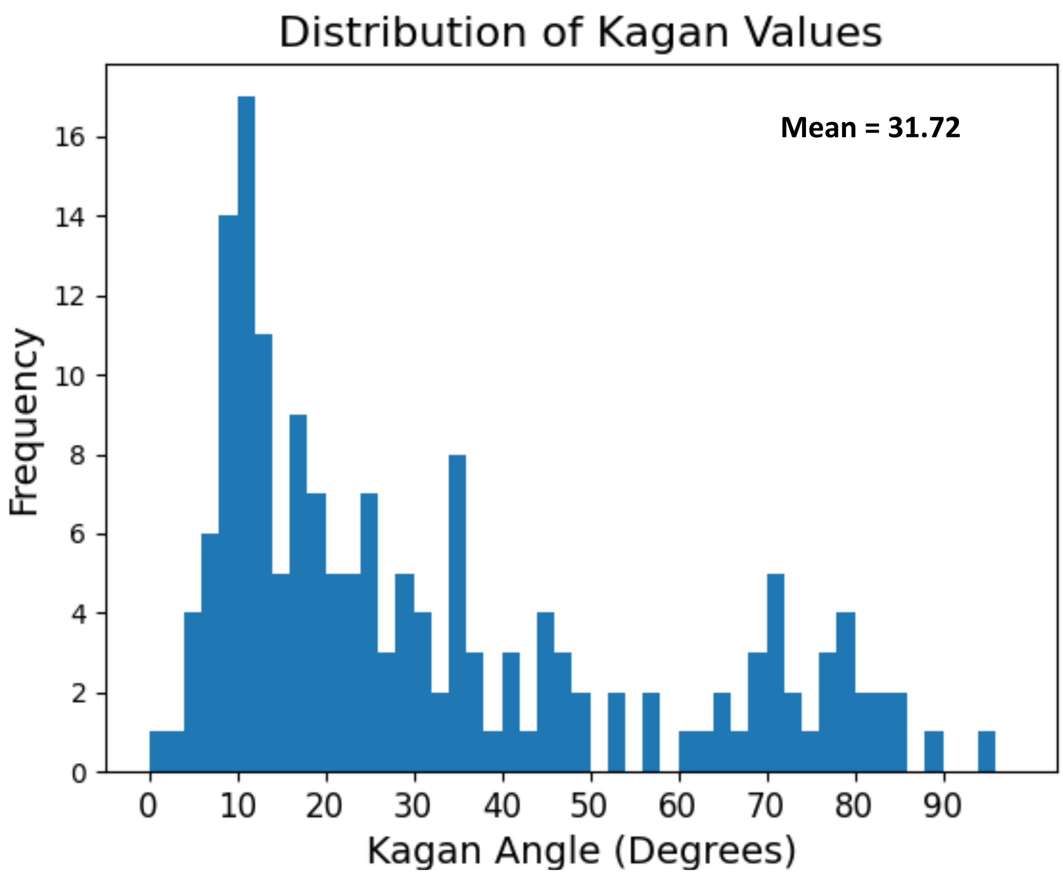

Figure 26: Distribution of Kagan values

The locations of events with Kagan values larger than 50 were plotted with reference to the well site and station locations, which shows that they are part of the cluster in the top right of the study area (Figure 27). The imperfect station coverage may be a reason for the discrepancy between the two solutions.

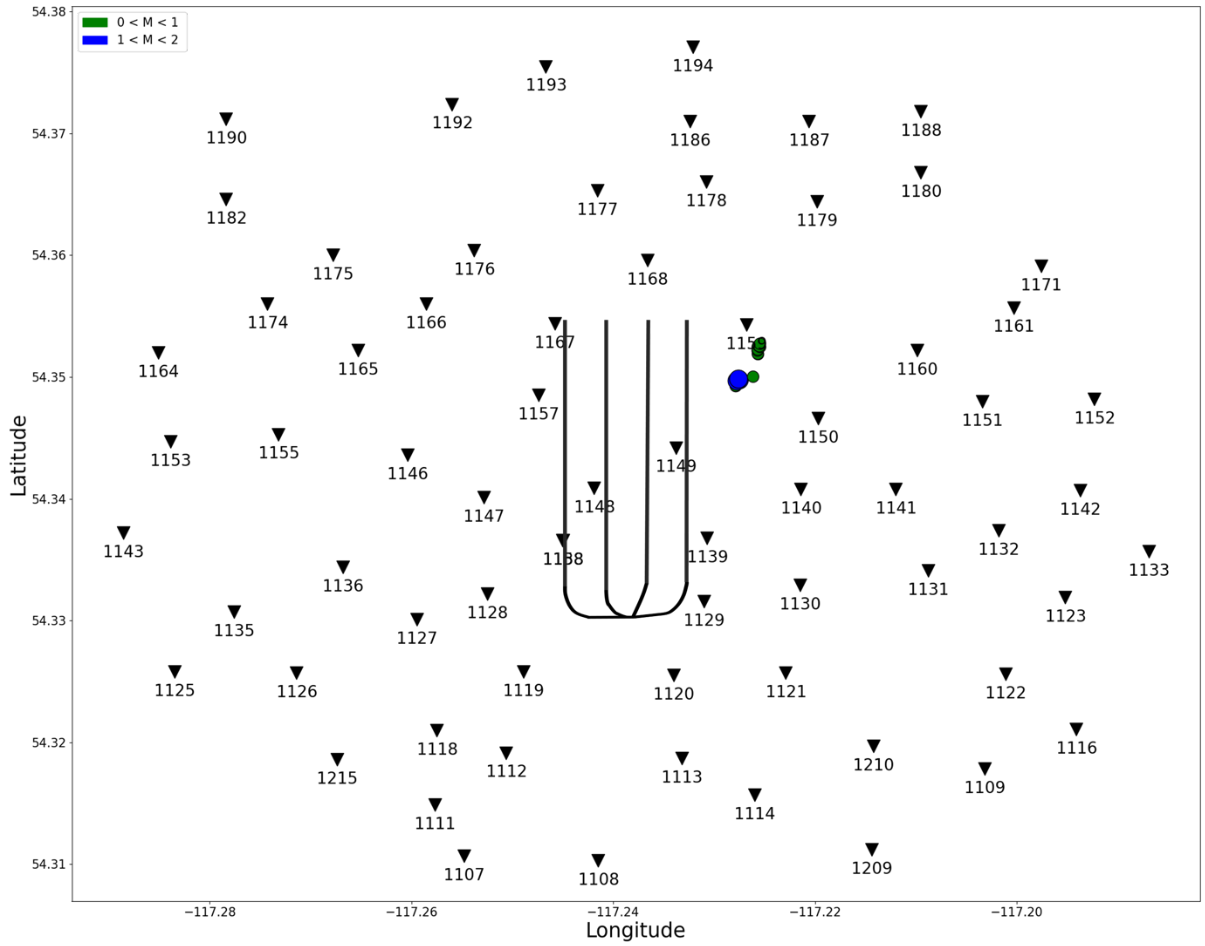

Figure 27: Location of events with Kagan values greater than 50

3.3 Coulomb Stress Changes

The distribution of magnitude versus time was plotted for over 21 000 events from the F Zhang et al 2022 catalog. A selection of three major earthquake sequences were identified and were used for stress change analysis (Figures 28 and 29). The parameters for the largest event in each were used to create the Coulomb stress change plots with the Coulomb 3.4 software. The spatial resolution is limited to be 0.001° by the software. The friction coefficient of 0.4 was adopted as suggested by most studies. The second fault plane solution was considered for the stress calculation. The fault length and width were empirically estimated by the in-built function, which relies on the magnitudes of the earthquakes. The earthquakes within the sequence time intervals were extracted and plotted, as well as the hydraulic fracturing well site for reference and analysis.

The earthquake sequence 1 occurred during the first stage of stimulation along well C and the other two sequences occurred during the second stage of stimulation along wells A, B, and D (Figures 28 and 29). In sequence 1 we consider the M 2.82 earthquake that occurred between wells C and D on November 10th (Figure 30). Sequence 2 considers the largest event of the catalog, an M 3.21 event located near the top of well D that occurred on November 25th (Figure 31). Finally, sequence 3 considers the M 3.1 event to the bottom left side of well D that occurred on November 29th (Figure 30). The spatial stress distribution reflects the rupture direction (i.e., rake) of the earthquake along a defined fault plane (i.e., strike and dip). It exhibits a more complex pattern than the focal mechanism solutions due to their different source models (finite fault vs. point source). Only four quadrants are available for the point source model that is used in focal mechanism solution; however, 3D stress could be inferred from a finite fault model with fault length and width that is used in Coulomb stress calculation, providing much more detailed information. Overall, earthquakes occurred around the injection wells and their nearby regions. The relative locations of the late earthquakes and the stress change of their prior major events provide a clue to interpret their triggering mechanisms, along with the distance from the nearest wells and identified fault zones. Detailed triggering mechanisms will be discussed in Section 4.3.

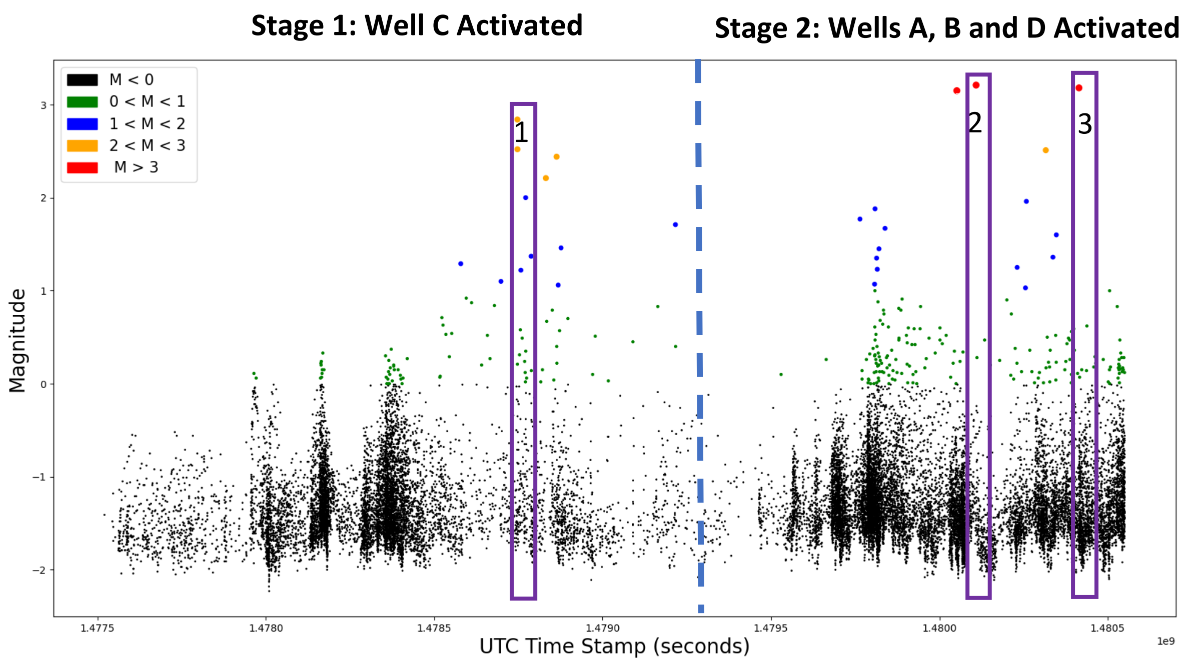

Figure 28: Distribution of magnitudes over time for full catalog
The three major earthquakes chosen for coulomb stress analysis are labeled.

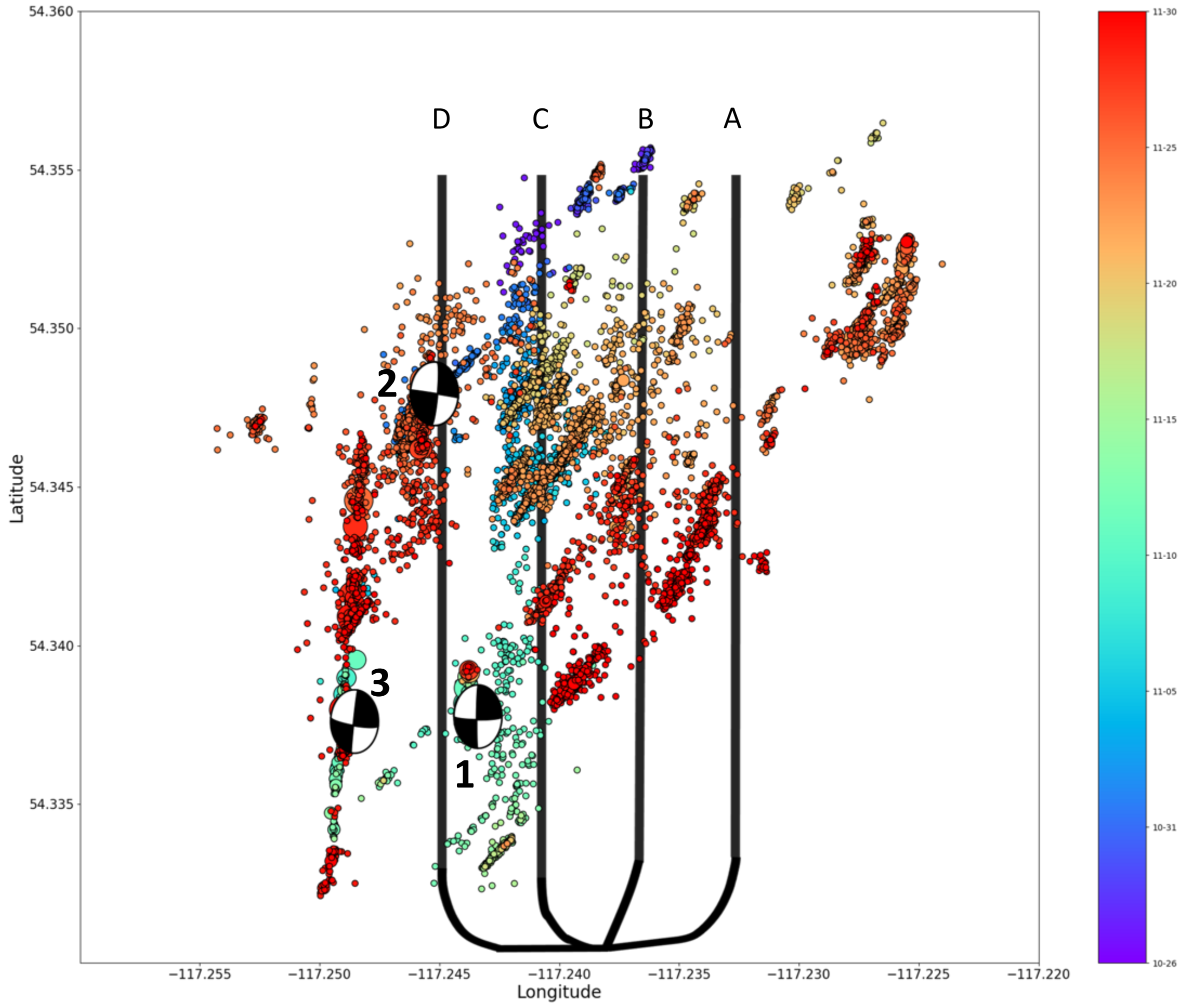

Figure 29: Location of focal mechanism with reference to the seismic events used for stress change analysis

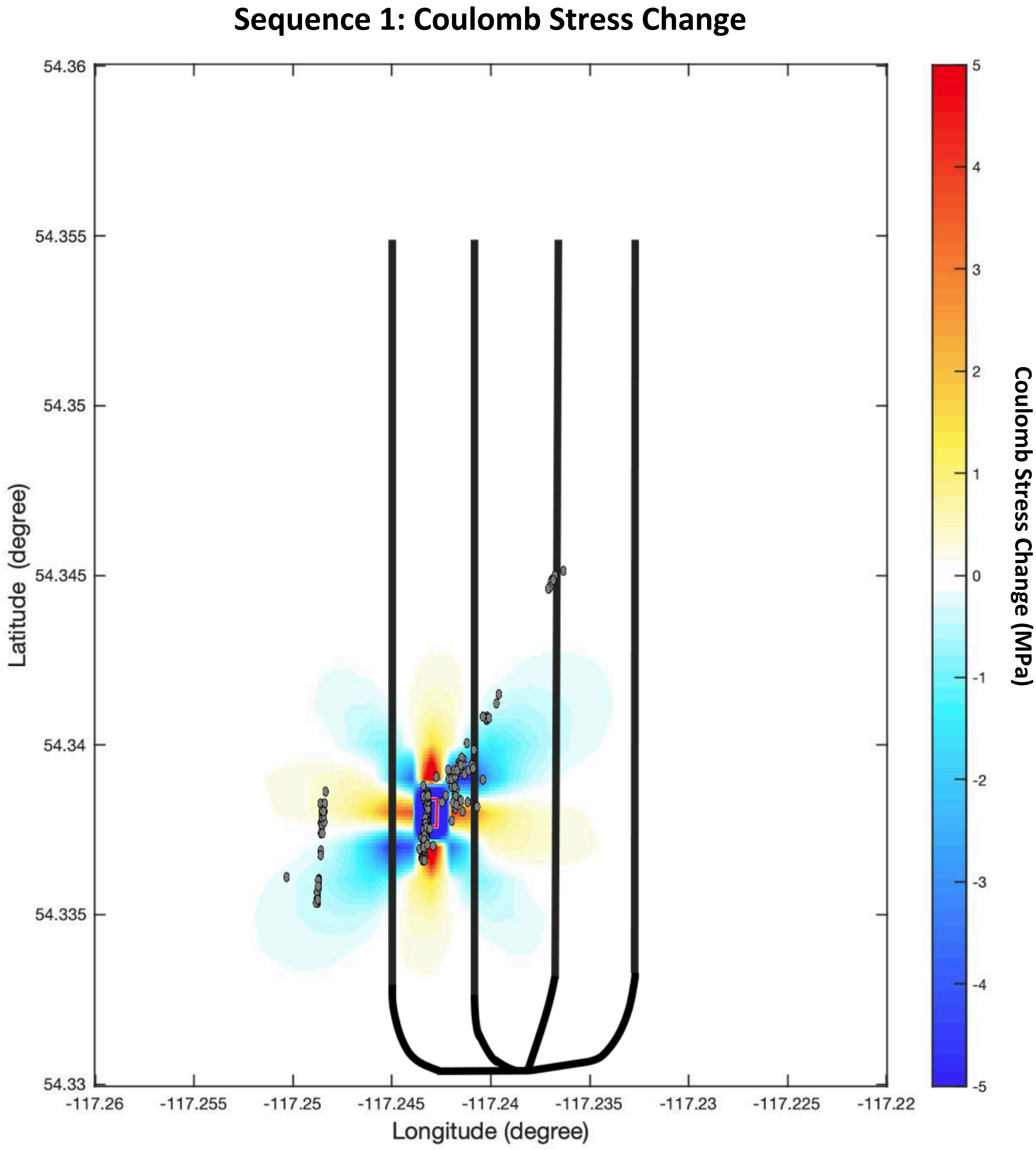

Figure 30: Coulomb stress change for Sequence 1
Future rupture along a modeled fault is favoured in regions of increased stress change (warmer colours)

Sequence 2: Coulomb Stress Change

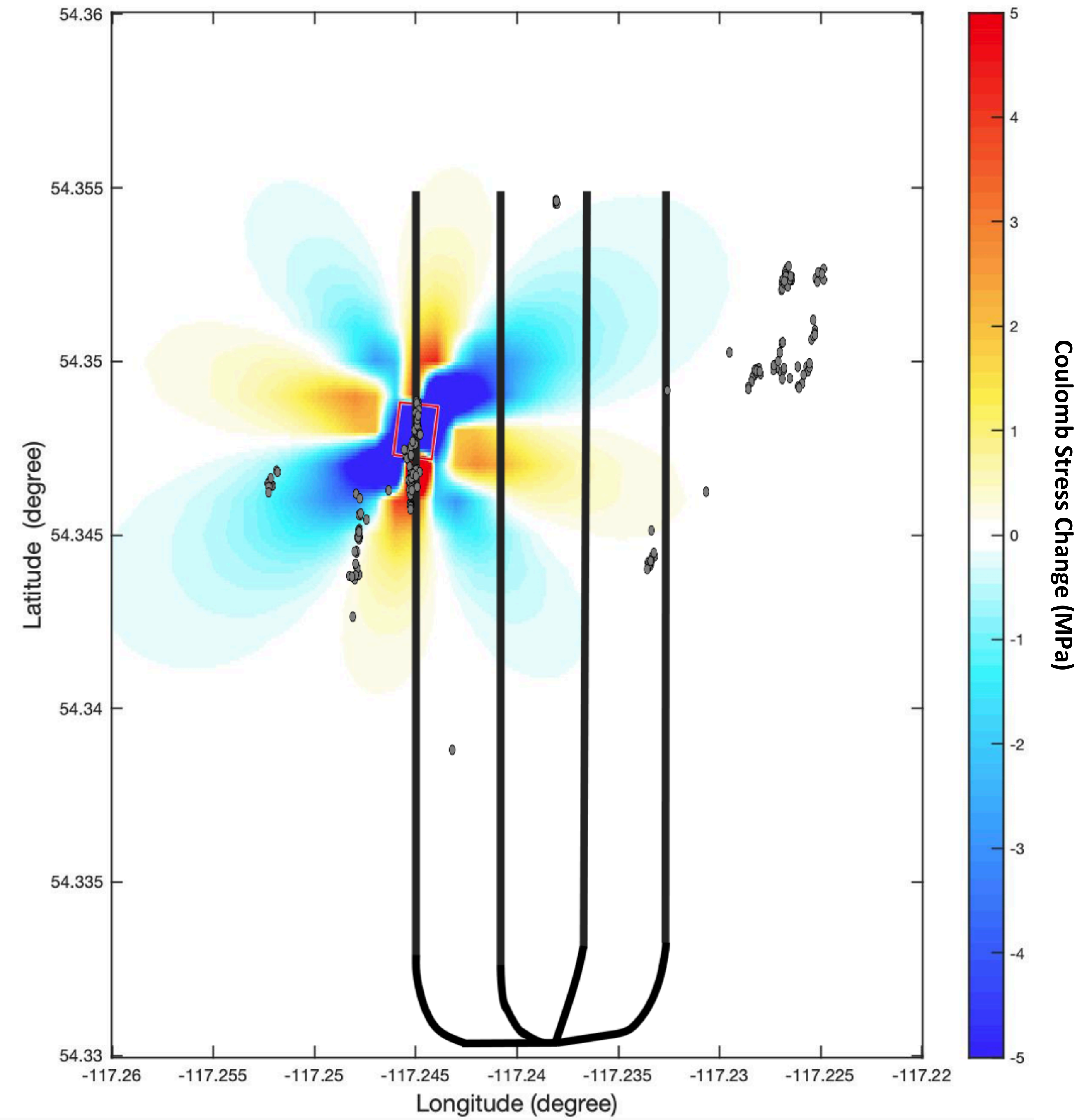

Figure 31: Coulomb stress change for Sequence 2

Sequence 3: Coulomb Stress Change

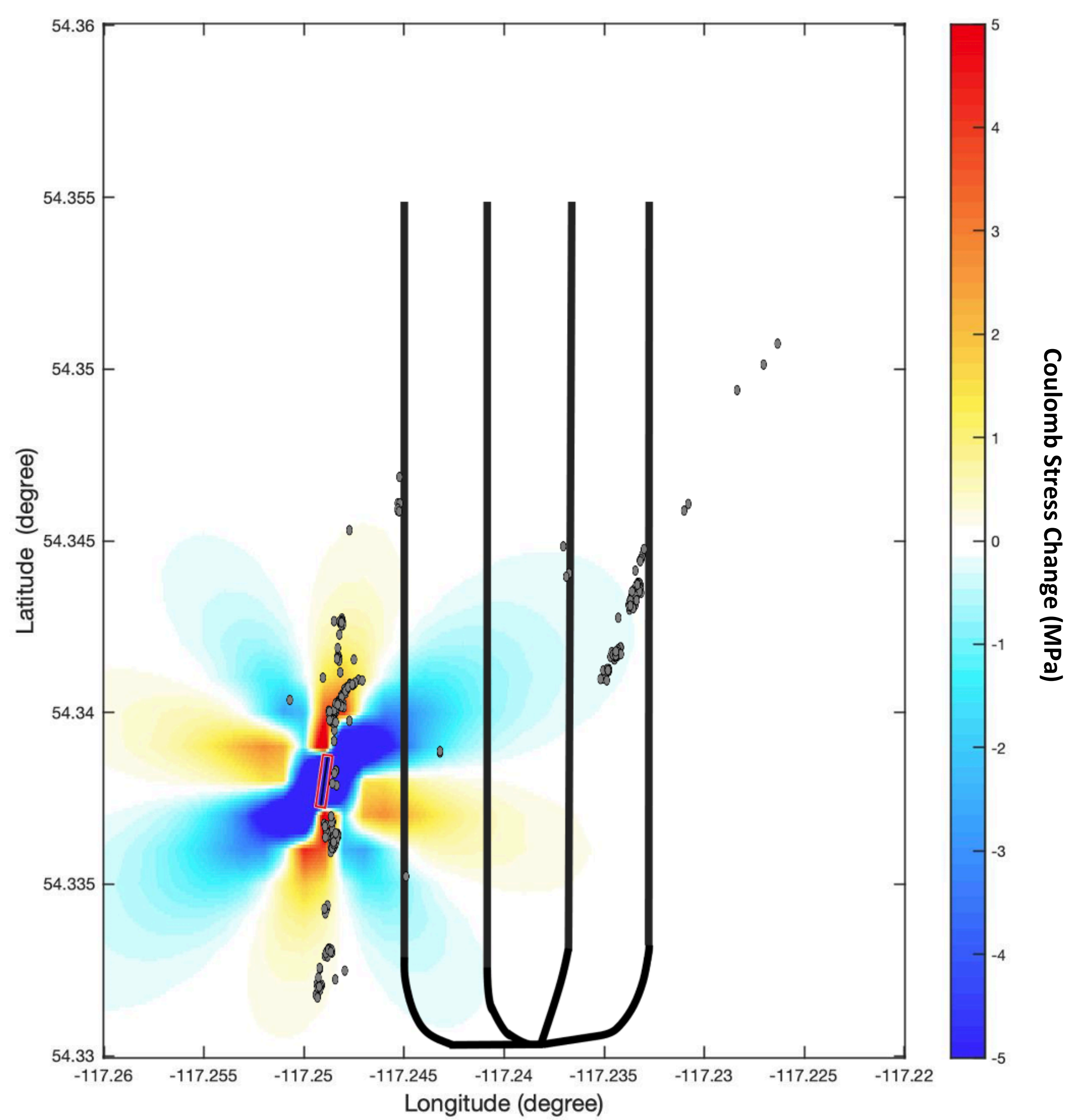

Figure 32: Coulomb stress change for Sequence 3

Chapter 4: Discussion

4.1 P Wave First Motion Polarities

In terms of efficiency, DiTingMotion took approximately 40 minutes to determine the polarities for almost 15 000 waveforms. This is substantially less time than it would take for a human to go through and analyse each waveform individually. To test the reliability of first motion picks, a selection of polarity pick waveform plots were analysed (see supplementary material for all data). Due to the nature and timeline of this study it was not feasible to confirm each event so the initial focus was on events that were found to have multiple “undetermined (X)” picks. Calculations for total pick counts for each event are shown in Appendix A.

Initial visual analysis showed that many of the picks that were classified as “X” were associated with low SNR values (in this case under 150). SNR represents the signal to noise ratio, which is a measure of how strong the earthquake event signal is compared to the background noise. Microearthquakes, such as those related to hydraulic fracturing activities, are often associated with low SNR values, which can lead to inaccurate arrival time picks and polarities (Huang et al., 2017).

For example, this ‘X’ pick for event 20161129164710.560 has a very low SNR of 3.200 (Figure 33). When plotting the waveform for its station 5B.1130, we can see that there is not a clear beginning for the event. Therefore, it is reasonable that the program was unable to determine its polarity.

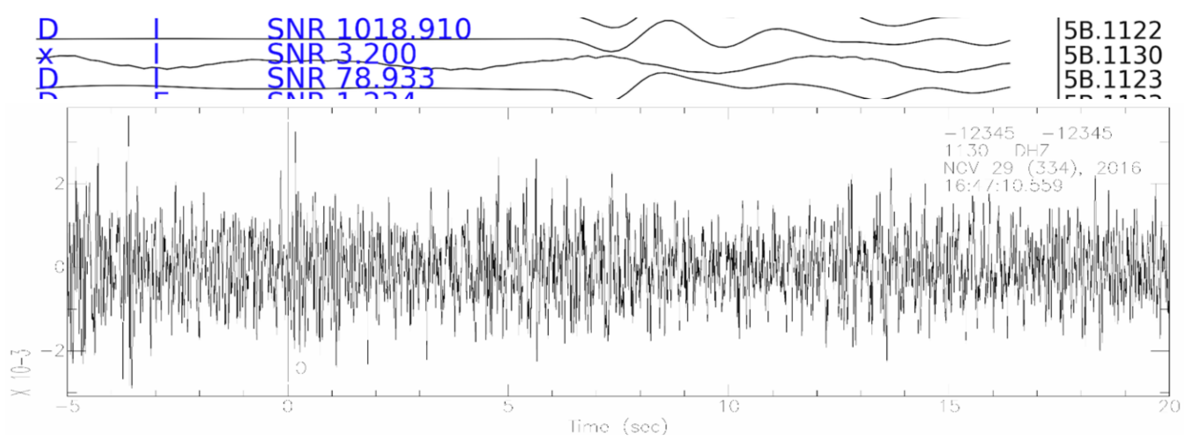

Figure 33: Example of low SNR “X” polarity waveform

Although the model was able to successfully classify some "up (U)" and "down (D)" polarities from waveforms with low SNR values, this was not always the case and there are examples of the wrong polarity being chosen. Taking a closer look at event 20161109133343.450 shows that the highlighted "U" pick is more similar to an initial "D" pick instead (Figure 34).

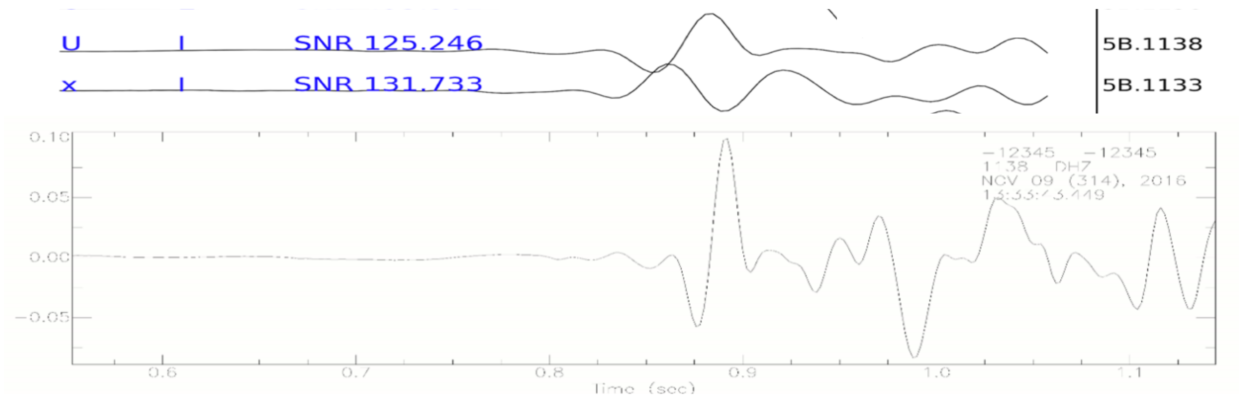

Figure 34: Example of wrongly classified "U" polarity waveform

It should also be noted that for 'X' picks with higher SNR values, some of the picks should have instead be classified as 'U' or 'D'. For example, in the plot for event 20161130235036.120 (Figure 35), the 'X' pick highlighted here is very similar to the other picks that were classified as 'D'. Plotting the waveforms from that station further supports this, as we can clearly see an initial down motion.

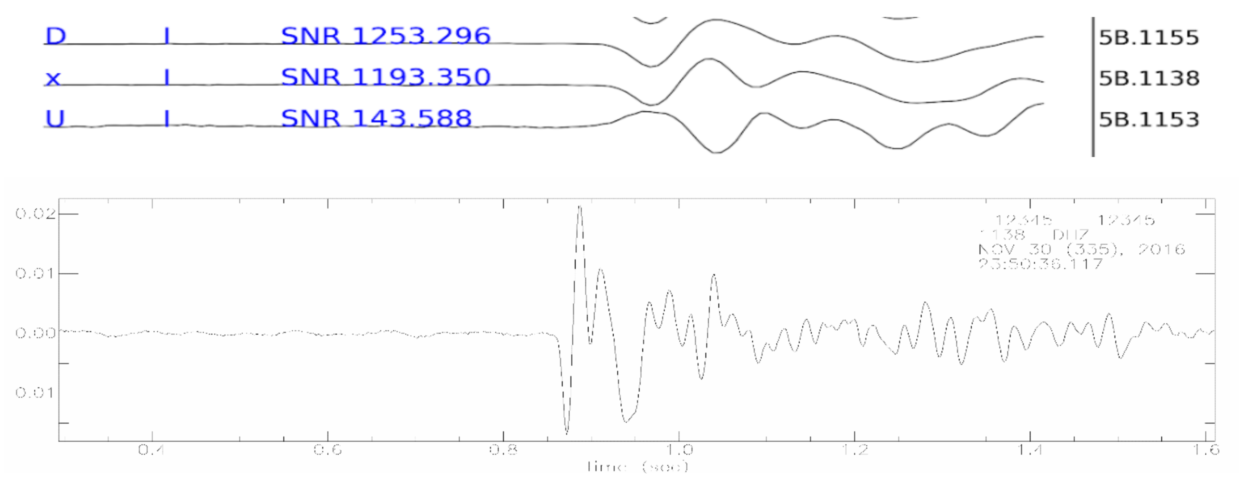

Figure 35: Example of wrongly classified "X" waveform

These results indicate that the total pick counts and averages displayed in Table 2 and Figure 17 represent estimates and are not accurate for all cases. The higher distribution of 'D' picks versus

‘U’ is likely still valid and is due to the distribution of events compared to station locations. Based on the focal mechanism solutions, we observed ‘U’ picks were received from stations roughly in the NE and SW quadrants. The number of stations in each section relative to an event is not always even and therefore can impact the distribution of received ‘U’ and ‘D’ waves. For example, by examining the cluster of events in the top right corner in Figure 11, we can see that these events have fewer stations in those directions compared to stations that would be receiving ‘D’ waves.

Overall, these discrepancies may be the results of several factors. Firstly, the low SNR values as a result of the low magnitude of events means that some polarities are difficult to determine manually and by use of machine learning. Secondly, DiTingMotion was trained using the DiTing dataset, with a sampling rate of 100 Hz, which includes epicenters up to ~330 km (Zhao et al., 2023), whereas the ToC2ME data is localized to only a few kilometers, with a sampling rate of 500 Hz. On the other hand, earthquakes in this study have much lower magnitudes than their training dataset.

The model could still benefit from improvements, especially when dealing with lower signal to noise ratios. Transfer learning could be applied to improve the model when applied to lower magnitude earthquakes, such as for hydraulic fracturing cases, however, this is out of the scope of this work.

4.2 Focal Mechanism Solutions

Running the HASH program took approximately 20 minutes to solve for 254 solutions. This is again much faster and more efficient compared to if these calculations were done by hand.

4.2.1 Distributions of All Events

Based on visual analysis, the results appear fairly consistent with the largest 100 events plotted by Igonin et al. 2021 (Figure 36). The fault planes to the left of the wells are aligned in the N-S direction for both plots. The orientation of the events in the top right corner are also similar.

Based on these clear delineations we can determine which fault plane solution most accurately describes the focal mechanism. In this case we are looking for the solution that has a strike oriented in the N-S direction rather than E-W. Based on this analysis, we find that our desired solution is fault plane 2 (i.e., N-S).

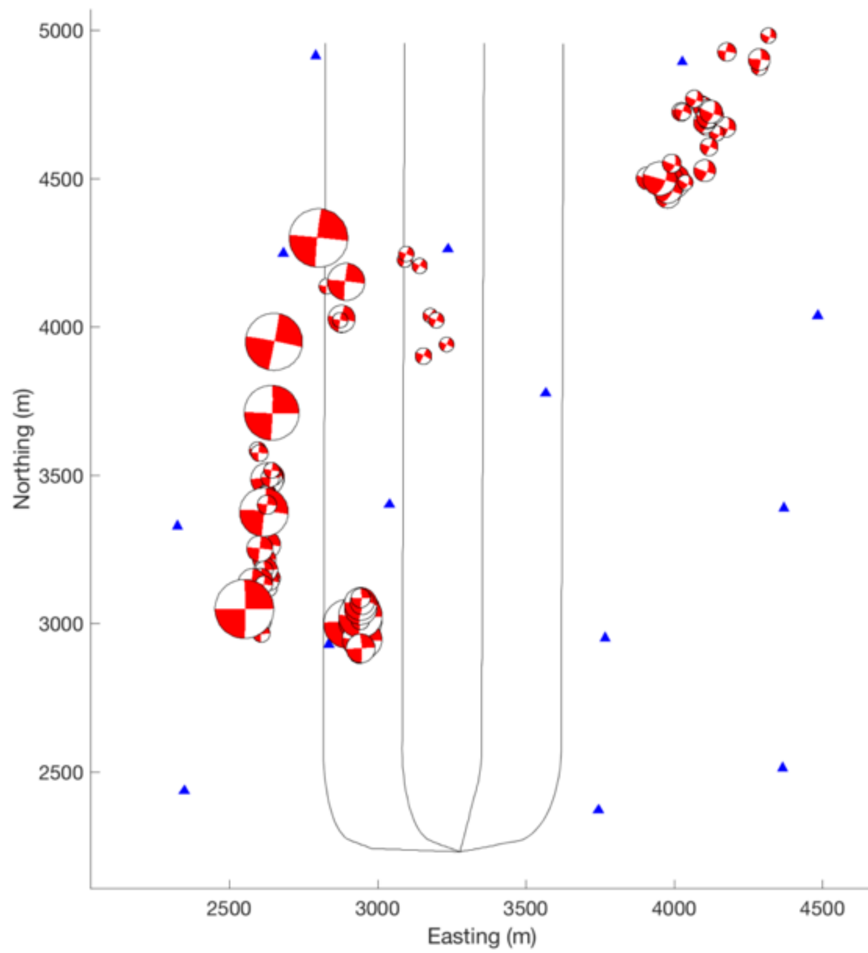

Figure 36: 100 largest event focal mechanism solution from Igonin et al 2021

4.2.2 Solution Quality Analysis

The quality of a focal mechanism result is mostly dependent on the accuracy and number of the P wave polarity picks. Table 4 shows a pair of focal mechanism solutions with good quality and poor quality. One method of analysing the quality of a solution is to take into consideration its

RMS value, which is a measure of trace error. A high RMS value indicates that there is a higher degree of variation from the averaged reported solution. Ideally the traces should be concentrated in two directions, defining the two possible fault planes. The distribution of RMS values is shown in Figure 20 and the mean was found to be 10, indicating that most solutions were fairly stable.

<table>
<tr><th>Good Quality</th><th>Poor Quality</th></tr>
<tr><td>
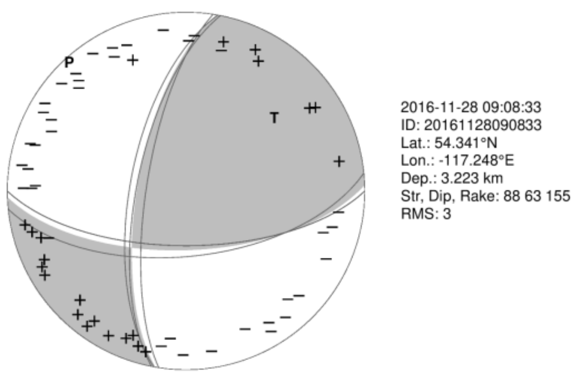

Low RMS
Polarities are representative of all directions
Traces are concentrated around two fault planes with minor variation
Fault planes well contratined to polarity data

</td><td>
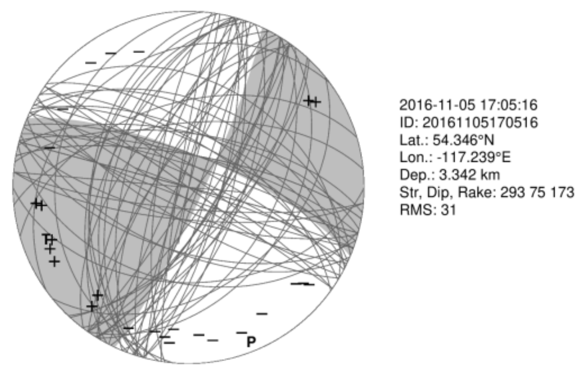

High RMS
Polarity data lacking in certain directions
Traces are not concentrated in around two planes

</td></tr>
</table>

Table 4: Comparison of good and poor quality HASH focal mechanism outputs

Based on the locations of polarity picks, many solutions are well constrained (meaning “+” picks are in the dark zones and “-“ in the white zones), however there can be instability of traces around the fault planes resulting in elevated RMS values. For example, events 20161120222605.960 and 20161108172656.100 show instability along the horizontal plane (Figure 37), which may be attributed to the distribution or availability of seismic stations.

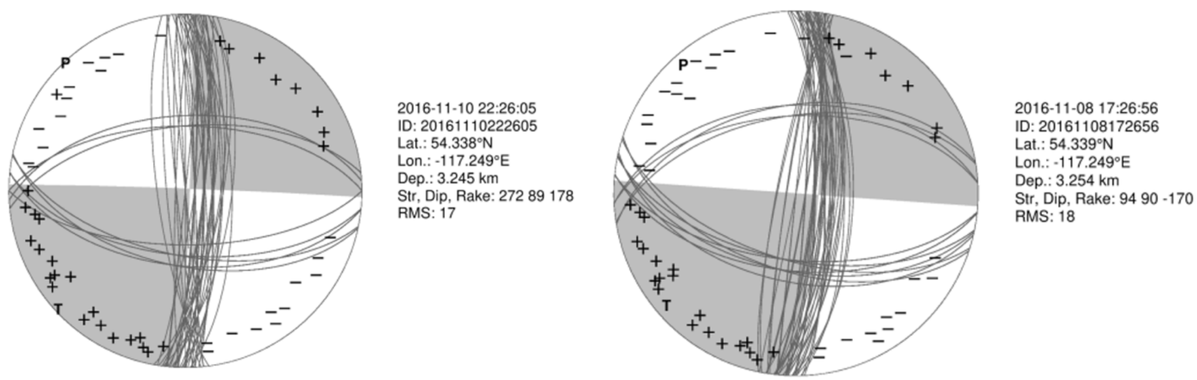

Figure 37: Focal mechanisms showing greater instability in along horizonal plane

Similarly, events 20161127105310.170 and 20161112192015.560 demonstrate examples of greater instability along the vertical plane but are well constrained by the polarities (Figure 38). These instabilities may be a result of imperfect velocity models, for instance, heterogeneity and anisotropy of the Earth. On the other hand, the inaccurate S/P amplitude ratios may also be a reason because waveforms may be clipped at some stations (Eaton et al., 2018).

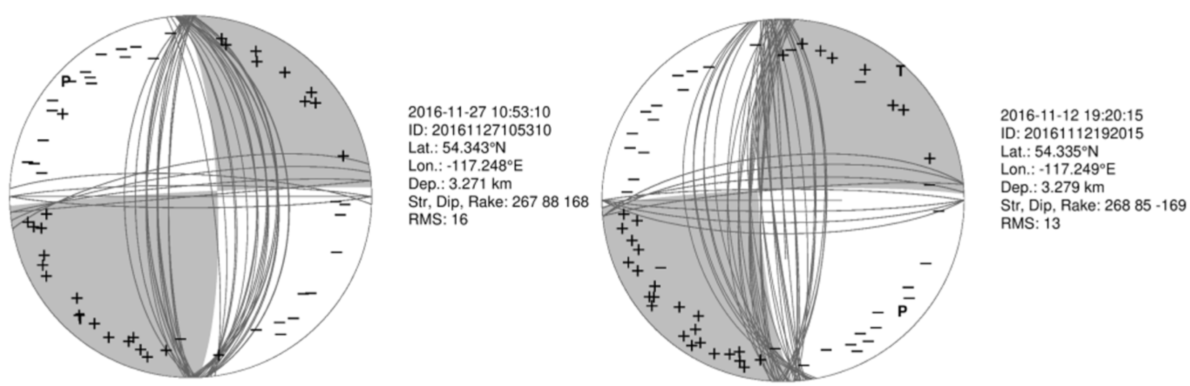

Figure 38: Focal mechanisms showing greater instability along the vertical plane

17 events had RMS values over 25 (shown in Table 3), and 12 of these all occurred on the same day, November 30th, 2016 (Figure 39). A closer look at a few of these solutions reveals that polarity data is unavailable for several directions. This is due to missing waveform data from multiple stations. This was the last day of data collection, so removal of stations had likely already begun at this point.

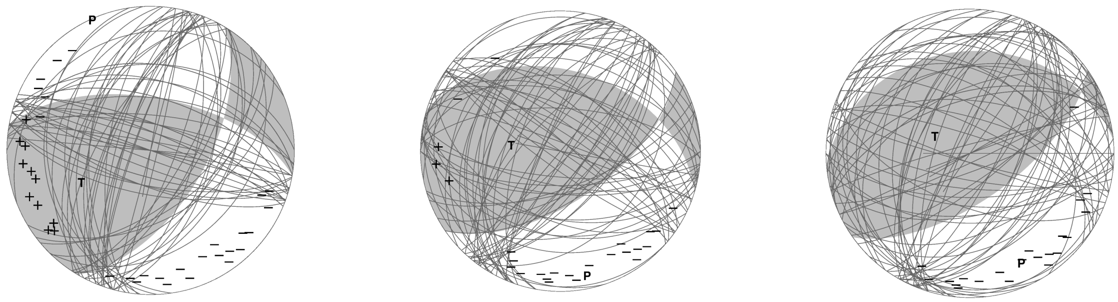

Figure 39: Examples of November 30th, 2016 events with high RMS values

4.2.3 Comparing Solutions with H Zhang et al. 2019

In order to test the reliability of our results, 166 focal mechanism solutions were compared to moment tensors which had been previously calculated by H Zhang et al. 2019, where they used the amplitude information on three components instead of first motions. The moment tensors were first converted to the two possible fault plane solutions, and their strike, dip, and rake distributions were plotted to compare to this study. In general, both fault plane solutions tended to have similar distributions. The strikes values were typically clustered in the same region. The dips and rakes for fault plane 1 also had similar clusters. There was more variation between the dips and rakes for fault plane 2 solutions, with their dataset having well defined peaks and ours have a wider distribution.

The Kagan values were calculated for fault plane 2 and their distribution is shown in Figure 26. The average value was 31.72 °. Ideally the similar solutions should be within 20° of each other. The higher Kagan values reflect a discrepancy between strike, dip, and rake values for the two solutions. A total of 34 events had Kagan values above 50°. These event locations were plotted in Figure 27, which shows that these events are part of the cluster in the top right of the study area. By examining Appendix D, we see that these events typically have similar strikes, some variation in dip, and a larger variation in rake. For these cases, one rake value was positive and the other was negative. Therefore, there must be an issue refining the rake values between the two methods in this region. This could potentially be due to the lower number of stations in the

N-E quadrant relative to each event, making it difficult to constrain the polarities from that direction.

Another possible explanation for the differences between these two methods is the way in which the focal mechanism solutions were derived. The moment tensors calculated by H Zhang et al. 2019 take into consideration double-couple components and non-double-couple components, whereas our result does not consider the non-double components. This means that their results may account for more complex fault movement. In their study, they found that most events in Group C (shown in green in Figure 40) has exhibit significant non-double couple components. These events are located in same region as the events shown in Figure 26.

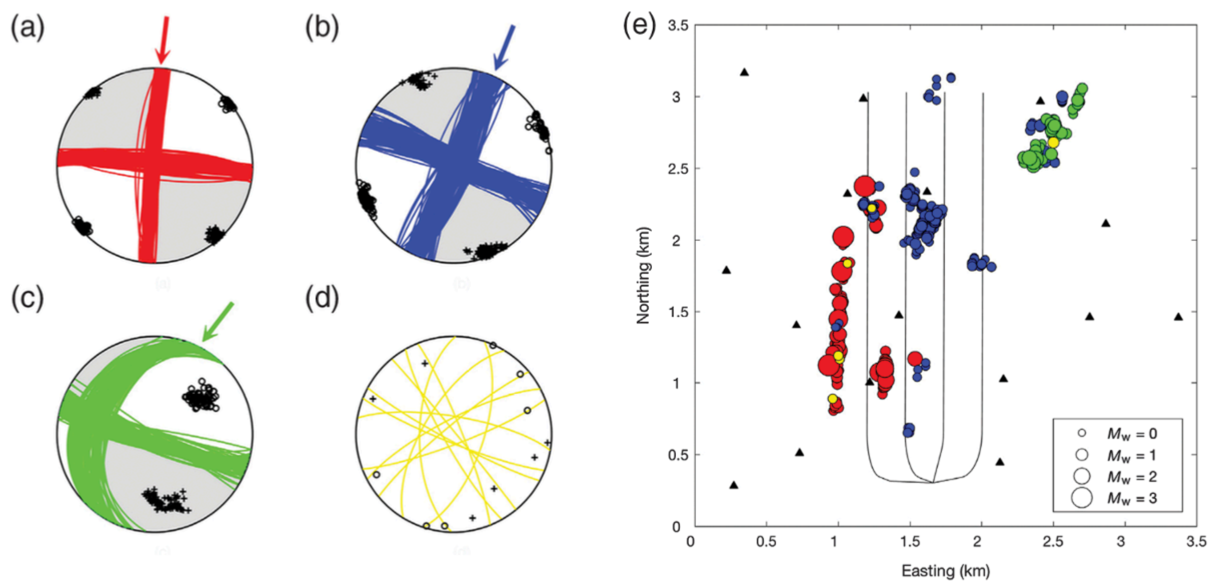

Figure 40: 530 focal mechanism solutions from H Zhang et al 2019

4.3 Triggering Mechanisms

In sequence 1 (Figure 30), we observe that most events occurred in regions of stress decrease, indicating that they are unlikely caused by coulomb stress change. Instead, due to their close proximity to the wells, pore pressure is likely the dominating mechanism. We also see that there are a cluster of events which occurred along the earthquake fault plane, and the N-S fault to the right of well D, in regions of increased stress, suggesting that coulomb stress transfer could be at play as well. The small cluster of events along well B may be a result of poroelasticity since this well was inactive at the time.

In sequences 2 (Figure 31), we see a line of smaller magnitude events which occurred along the fault plane of the largest event. Since these events also occurred along well D this suggests that both coulomb stress transfer and pore pressure could be responsible. The events next to well A are likely a result of pore pressure increase as they fall just outside the regions of increased stress and are in close proximity to a well.

In sequence 3 (Figure 31), most of the smaller magnitude events occurred directly on the major event fault plane and were within regions of increased stress. This suggests that coulomb stress transfer may have been a dominant mechanism for those events also seeing as they were not directly along the wells. We again see clusters of events occurring along the active wells, suggesting that pore pressure is also dominating this sequence.

In all sequences 2 and 3, we also see a few events occurred in the stress decreased zones and far away from the injection wells, for example, the events in the top right corner. Those earthquakes may be triggered by poroelasticity although more evidence is needed to confirm this (e.g., quantitative numerical modelling).

F Zhang et al 2022 proposed that coulomb stress transfer is the dominant mechanism for the events along the NSw fault to the left of well D. Our results, specifically sequence 3, support this hypothesis as the majority of events following the larger event fall within this plane of elevated stress. They also propose that the NSe fault near the top of well D was initiated by elevated pore pressure. Our results for sequence 2 also suggests that coulomb stress transfer may be responsible for the events along that fault.

It is necessary to acknowledge that these results do not take into consideration the coulomb stress interactions between each of the smaller events, which may also explain some events that occurred in decreased stress zones near the larger event. On the other hand, a threshold of stress change could be introduced for more quantitative and accurate investigation, which requires more information or introduces assumptions.

Chapter 5: Conclusions and Future Work

Firstly, this study aimed to demonstrate the efficiency and reliability of machine learning in classifying the polarities and characterizing the focal mechanisms of hydraulic fracturing-induced earthquakes. We have shown that DiTingMotion and HASH are quickly able to determine the polarities of P waves and focal mechanisms solutions respectively. However, the DiTingMotion model could be improved to better handle events with lower magnitudes, which could be achieved through transfer learning.

To test the reliability of the focal mechanism results obtained from the P wave polarities we first analysed the HASH RMS values. The distributions of RMS values showed that many of the solutions were fairly stable and were well constrained by the polarities. Solutions with higher RMS values and instability around the fault planes may be due to imperfect velocity models or availability of stations (e.g., the last day of the observation). Next, 166 solutions were compared to moment tensor solutions which had been calculated by H Zhang et al. 2019. Kagan values were calculated to quantify the difference between these datasets and the average was found to be 31.72 °. For fault plane solutions with Kagan values above 50°it was observed that there was some variation in their dip angles and a high variation in rake values. These events were plotted, which showed that they all belonged to the cluster in the top right corner of the study area. This suggests that there may be a lack of polarity data from the in the N-E quadrant relative to these sites, which could account for the difficulty in constraining the dip and rake of this solution. Additionally, the discrepancy may also be due to the difference in methodology for obtaining the fault plane solutions. Our method only accounts for double-couple components for the mechanisms, whereas H Zhang et al. 2019 moment tensors consider non-double-couple components as well.

Secondly, this study aimed to investigate the associated mechanisms governing earthquake triggering during hydraulic fracturing. Three major event sequences were chosen, and their coulomb stress change was calculated and analysed. Our results demonstrate that pore pressure is likely the dominant mechanism for sequence 1, whereas coulomb stress transfer and pore pressure dominate sequences 2 and 3. Events which occurred further from the well site and in regions unaffected by the coulomb stress change may be explained by poroelasticity. This suggests that the three triggering mechanisms could co-exist during hydraulic fracturing, though they dominate different event sequences at different stages and/or locations. On the other hand, geological settings, hydraulic fracturing operations, and the distribution of pre-existing faults/fractures also play important roles in earthquake triggering. Thus a comprehensive knowledge of them is critical to understand induced earthquake triggering, which is essential to mitigate the seismic hazard during hydraulic fracturing and to optimize shale gas production.

Future work could include analysing more coulomb stress change sequences, as it would be especially helpful to have examples from initial events. More calculations are necessary to gain a better overall understanding of how the different mechanisms contribute and to what stages they are most prominent. For this analysis, it may be useful to try using a different software, such as AutoCoulomb (Wang et al., 2022), as Coulomb 3.4 has a limited resolution of 0.001°.

References

Aminzadeh, F. (2018). Hydraulic Fracturing, An Overview. *Journal of Sustainable Energy Engineering*, *6*(3), 204–228. https://doi.org/10.7569/jsee.2018.629512

Atkinson, G. M., Eaton, D. W., Ghofrani, H., Walker, D., Cheadle, B., Schultz, R., Shcherbakov, R., Tiampo, K., Gu, J., Harrington, R. M., Liu, Y., Van Der Baan, M., & Kao, H. (2016). Hydraulic fracturing and seismicity in the western Canada sedimentary basin. *Seismological Research Letters*, *87*(3), 631–647. https://doi.org/10.1785/0220150263

Bao, X., & Eaton, D. W. (2016). Fault activation by hydraulic fracturing in western Canada. Science (New York, N.Y.), 354(6318), 1406–1409. https://doi.org/10.1126/science.aag2583

Cao, W., Verdon, J. P., & Tao, M. (2022). Coupled Poroelastic Modeling of Hydraulic Fracturing-Induced Seismicity: Implications for Understanding the Post Shut-In ML 2.9 Earthquake at the Preston New Road, UK. *Journal of Geophysical Research: Solid Earth*, *127*(3). https://doi.org/10.1029/2021JB023376

Chakraborty, M., Cartaya, C. Q., Li, W., Faber, J., Rümpker, G., Stoecker, H., & Srivastava, N. (2022). PolarCAP – A deep learning approach for first motion polarity classification of earthquake waveforms. *Artificial Intelligence in Geosciences*, *3*, 46–52. https://doi.org/10.1016/j.aiig.2022.08.001

Chang, K. W., & Segall, P. (2016). Injection-induced seismicity on basement faults including poroelastic stressing. *Journal of Geophysical Research: Solid Earth*, *121*(4), 2708–2726. https://doi.org/10.1002/2015JB012561

Chang, K. W., Yoon, H., Kim, Y. H., & Lee, M. Y. (2020). Operational and geological controls of coupled poroelastic stressing and pore-pressure accumulation along faults: Induced earthquakes in Pohang, South Korea. *Scientific Reports*, *10*(1). https://doi.org/10.1038/s41598-020-58881-z

Dong, T., Harris, N. B., McMillan, J. M., Twemlow, C. E., Nassichuk, B. R., & Bish, D. L. (2019). A model for porosity evolution in shale reservoirs: An example from the Upper Devonian Duvernay Formation, Western Canada Sedimentary Basin. *AAPG Bulletin*, *103*(5), 1017–1044. https://doi.org/10.1306/10261817272

Eaton, D. W., & Eyre, T. S. (2018). *Induced Seismicity in Western Canada: Causes and Consequences*. https://www.researchgate.net/publication/329630079

Ellsworth, W. L. (2013). Injection-induced earthquakes. Science (New York, N.Y.), 341(6142). https://doi.org/10.1126/science.1225942

Eyre, T. S., Eaton, D. W., Zecevic, M., D'Amico, D., & Kolos, D. (2019). Microseismicity reveals fault activation before Mw 4.1 hydraulic-fracturing induced earthquake. *Geophysical Journal International*, *218*(1), 534–546. https://doi.org/10.1093/gji/ggz168

Galderisi, A., & Galli, P. (2020). Coulomb stress transfer between parallel faults. The case of Norcia and Mt Vettore normal faults (Italy, 2016 Mw 6.6 earthquake). *Results in Geophysical Sciences*, *1–4*, 100003. https://doi.org/10.1016/j.ringps.2020.100003

Ge, S., & Saar, M. O. (2022). Review: Induced Seismicity During Geoenergy Development—A Hydromechanical Perspective. In *Journal of Geophysical Research: Solid Earth* (Vol. 127, Issue 3). John Wiley and Sons Inc. https://doi.org/10.1029/2021JB023141

Goebel, T. H. W., Weingarten, M., Chen, X., Haffener, J., & Brodsky, E. E. (2017). The 2016 Mw5.1 Fairview, Oklahoma earthquakes: Evidence for long-range poroelastic triggering at >40 km from fluid disposal wells. *Earth and Planetary Science Letters*, *472*, 50–61. https://doi.org/10.1016/j.epsl.2017.05.011

Hara, S., Fukahata, Y., & Iio, Y. (2019). P-wave first-motion polarity determination of waveform data in western Japan using deep learning. *Earth, Planets and Space*, *71*(1). https://doi.org/10.1186/s40623-019-1111-x

Hardebeck, J. L., & Shearer, P. M. (2002). A New Method for Determining First-Motion Focal Mechanisms. In *Bulletin of the Seismological Society of America* (Vol. 92, Issue 6).

Hardebeck, J. L., & Shearer, P. M. (2003). Using S/P Amplitude Ratios to Constrain the Focal Mechanisms of Small Earthquakes. *Bulletin of the Seismological Society of America* , *93*(6), 2434–2444.

Huang, W., Wang, R., Li, H., & Chen, Y. (2017). Unveiling the signals from extremely noisy microseismic data for high-resolution hydraulic fracturing monitoring. *Scientific Reports*, *7*(1). https://doi.org/10.1038/s41598-017-09711-2

Igonin, N., Verdon, J. P., Kendall, J. M., & Eaton, D. W. (2021). Large-Scale Fracture Systems Are Permeable Pathways for Fault Activation During Hydraulic Fracturing. *Journal of Geophysical Research: Solid Earth*, *126*(3). https://doi.org/10.1029/2020JB020311

Kagan, Y. Y. (2007). Simplified algorithms for calculating double-couple rotation. *Geophysical Journal International*, *171*(1), 411–418. https://doi.org/10.1111/j.1365-246X.2007.03538.x

Kong, Q., Trugman, D. T., Ross, Z. E., Bianco, M. J., Meade, B. J., & Gerstoft, P. (2019). Machine learning in seismology: Turning data into insights. *Seismological Research Letters*, *90*(1), 3–14. https://doi.org/10.1785/0220180259

Medina, F., & Cherkaoui, T.-E. (2017). The South-Western Alboran Earthquake Sequence of January-March 2016 and Its Associated Coulomb Stress Changes. *Open Journal of Earthquake Research*, *06*(01), 35–54. https://doi.org/10.4236/ojer.2017.61002

Perol, T., Gharbi, M., & Denolle, M. (2018). *Convolutional neural network for earthquake detection and location*. https://www.science.org

Ross, Z. E., Meier, M. A., & Hauksson, E. (2018). P Wave Arrival Picking and First-Motion Polarity Determination With Deep Learning. *Journal of Geophysical Research: Solid Earth*, *123*(6), 5120–5129. https://doi.org/10.1029/2017JB015251

Schultz, R., Atkinson, G., Eaton, D. W., Gu, Y. J., & Kao, H. (2018). Hydraulic fracturing volume is associated with induced earthquake productivity in the duvernay play. *Science*, *359*(6373), 304–308. https://doi.org/10.1126/science.aao0159

Schultz, R., Skoumal, R. J., Brudzinski, M. R., Eaton, D., Baptie, B., & Ellsworth, W. (2020). Hydraulic fracturing-induced seismicity. In *Reviews of Geophysics* (Vol. 58, Issue 3, pp. 1–43). Blackwell Publishing Ltd. https://doi.org/10.1029/2019RG000695

Segall, P., & Lu, S. (2015). Injection-induced seismicity: Poroelastic and earthquake nucleation effects. *Journal of Geophysical Research: Solid Earth*, *120*(7), 5082–5103. https://doi.org/10.1002/2015JB012060

Shah, A. K., & Keller, G. R. (2017). Geologic influence on induced seismicity: Constraints from potential field data in Oklahoma. *Geophysical Research Letters*, *44*(1), 152–161. https://doi.org/10.1002/2016GL071808

Sumy, D. F., Cochran, E. S., Keranen, K. M., Wei, M., & Abers, G. A. (2014). Observations of static Coulomb stress triggering of the November 2011 M5.7 Oklahoma earthquake sequence. *Journal of Geophysical Research: Solid Earth*, *119*(3), 1904–1923. https://doi.org/10.1002/2013JB010612

Switzer, S. B., W. G. Holland, D. S. Christie, G. C. Graf, A. S. Hedinger, R. J. McAuley, R. A. Wierzbicki, and J. J. Packard (1994) , Devonian Woodbend-Winterburn strata of the Western Canadian Sedimentary Basin, in G. D. Mossop and I. Shetsen, eds., Geological atlas of the Western Canada Sedimentary Basin: Calgary, Alberta, Canada, Canadian Society of Petroleum Geologists and the Alberta Research Council, p. 165–202.

Toda, Shinji, Stein, R.S., Sevilgen, Volkan, and Lin, Jian, (2011). Coulomb 3.3 Graphic-rich deformation and stress-change software for earthquake, tectonic, and volcano research and teaching—user guide: U.S. Geological Survey Open-File Report 2011–1060, 63 p., available at https://pubs.usgs.gov/of/2011/1060/

Trow, A. J., Zhang, H., Record, A. S., Mendoza, K. A., Pankow, K. L., & Wannamaker, P. E. (2018). Microseismic event detection using multiple geophone arrays in southwestern Utah. *Seismological Research Letters*, *89*(5), 1660–1670. https://doi.org/10.1785/0220180065

Uchide, T. (2020). Focal mechanisms of small earthquakes beneath the Japanese islands based on first-motion polarities picked using deep learning. *Geophysical Journal International*, *223*(3), 1658–1671. https://doi.org/10.1093/gji/ggaa401

Villa, V., & Singh, R. P. (2020). Hydraulic fracturing operation for oil and gas production and associated earthquake activities across the USA. *Environmental Earth Sciences*, *79*(11). https://doi.org/10.1007/s12665-020-09008-0

Wang, J., Xu, C., Freymueller, J. T., Wen, Y., & Xiao, Z. (2021). AutoCoulomb: An automated configurable program to calculate coulomb stress changes on receiver faults with any orientation and its application to the 2020 Mw7.8 Simeonof Island, Alaska, Earthquake. *Seismological Research Letters*, *92*(4), 2591–2609. https://doi.org/10.1785/0220200283

Yehya, A., Basbous, J., & Maalouf, E. (2022). Analysis of the Hydrogeological Conditions Affecting Fault Response to Nearby Hydraulic Fracturing. *Journal of Geophysical Research: Solid Earth*, *127*(10). https://doi.org/10.1029/2022JB024881

Yeo, I. W., Brown, M. R. M., Ge, S., & Lee, K. K. (2020). Causal mechanism of injection-induced earthquakes through the Mw 5.5 Pohang earthquake case study. *Nature Communications*, *11*(1). https://doi.org/10.1038/s41467-020-16408-0

Zhai, G., Shirzaei, M., Manga, M., & Chen, X. (2019). Pore-pressure diffusion, enhanced by poroelastic stresses, controls induced seismicity in Oklahoma. *Proceedings of the National Academy of Sciences of the United States of America*, *116*(33), 16228–16233. https://doi.org/10.1073/pnas.1819225116

Zhang, F., Wang, R., Chen, Y., & Chen, Y. (2022). Spatiotemporal Variations in Earthquake Triggering Mechanisms During Multistage Hydraulic Fracturing in Western Canada. *Journal of Geophysical Research: Solid Earth*, *127*(8). https://doi.org/10.1029/2022JB024744

Zhang, H., Eaton, D. W., Rodriguez, G., & Jia, S. Q. (2019). Source-mechanism analysis and stress inversion for hydraulic- fracturing-induced event sequences near fox Creek, Alberta. *Bulletin of the Seismological Society of America*, *109*(2), 636–651. https://doi.org/10.1785/0120180275

Zhang, M., Liu, M., Feng, T., Wang, R., & Zhu, W. (2022). LOC-FLOW: An End-to-End Machine Learning-Based High-Precision Earthquake Location Workflow. *Seismological Research Letters*, *93*(5), 2426–2438. https://doi.org/10.1785/0220220019

Zhao, M., & Xiao, Z. (2022). *DiTing: A large-scale Chinese seismic benchmark dataset for artificial intelligence in seismology*. http://creativecommons.

Zhao, M., Xiao, Z., Zhang, M., Yang, Y., Tang, L., & Chen, S. (2023). DiTingMotion: A deep-learning first-motion-polarity classifier and its application to focal mechanism inversion. *Frontiers in Earth Science*, *11*. https://doi.org/10.3389/feart.2023.1103914

Appendix A: DiTingMotion Polarity Counts

Event ID	Down	Up	Undetermined	Total Polarities
20161125212400.760	35	25	0	60
20161129101525.670	31	28	1	60
20161125053125.250	36	23	0	59
20161110030554.850	32	28	0	60
20161129041247.910	34	24	0	58
20161110030629.460	38	23	0	61
20161128065337.920	37	26	0	63
20161111112409.170	30	26	0	56
20161111023345.600	29	30	0	59
20161110095529.320	33	27	0	60
20161127145251.080	35	24	0	59
20161122100431.400	28	33	0	61
20161121213944.800	36	27	0	63
20161115132811.100	32	26	0	58
20161122181824.960	23	32	0	55
20161128153527.280	38	23	0	61
20161111150658.250	32	28	0	60
20161122131844.000	21	33	0	54
20161128124723.150	38	24	0	62
20161110142852.360	34	26	0	60
20161122112106.380	27	33	0	60
20161108042434.850	36	30	0	66
20161127071613.740	37	22	0	59
20161122115553.200	28	36	0	64
20161110055923.720	32	31	0	63
20161109133343.450	14	7	3	24
20161111124536.460	34	27	0	61
20161122094208.150	28	31	0	59
20161127140748.080	36	25	1	62
20161122095728.410	27	32	0	59
20161130113122.010	30	33	0	63
20161108085355.710	36	29	0	65
20161123082307.680	29	33	0	62
20161126224707.880	31	32	0	63
20161122122845.350	30	34	0	64
20161108131656.020	23	30	4	57
20161109080900.140	28	25	3	56
20161130174836.600	30	19	1	50
20161123233803.400	31	32	0	63
20161122172604.520	23	34	1	58
20161123053630.990	31	32	0	63

20161111075108.920	33	24	0	57
20161114225250.620	29	27	2	58
20161122170222.360	30	33	1	64
20161123072346.210	31	31	0	62
20161127022900.340	38	24	0	62
20161107124958.150	36	30	0	66
20161111204340.840	34	31	1	66
20161122141605.480	20	34	0	54
20161111031632.540	31	30	2	63
20161124153705.230	20	33	1	54
20161129164710.560	30	25	4	59
20161107134506.900	35	31	1	67
20161122210507.760	23	32	2	57
20161122095100.880	28	32	0	60
20161122105125.690	26	30	1	57
20161122162235.440	31	33	0	64
20161123133046.610	23	32	1	56
20161123181714.420	17	28	4	49
20161129055749.920	31	30	1	62
20161110053424.890	33	27	0	60
20161111135509.020	34	25	1	60
20161123231319.160	25	33	1	59
20161129040404.340	32	27	0	59
20161107160909.690	35	29	1	65
20161107205908.760	24	35	7	66
20161128150212.190	34	28	1	63
20161109022000.730	36	29	0	65
20161123115530.520	32	32	0	64
20161124204321.760	27	33	2	62
20161112192015.560	30	31	3	64
20161128080529.680	37	26	0	63
20161110070628.420	35	22	1	58
20161129013555.900	32	27	1	60
20161129023235.210	36	24	1	61
20161123123618.040	40	24	0	64
20161114022425.140	33	28	1	62
20161122100459.730	25	33	3	61
20161124063732.060	31	23	5	59
20161124153728.340	28	23	2	53
20161123190445.600	37	25	2	64
20161123054115.530	29	31	3	63
20161129002023.160	32	30	0	62
20161130195902.660	27	12	1	40
20161126042630.020	35	24	1	60
20161124173142.800	29	32	2	63
20161111113517.030	34	25	2	61

20161115133335.740	35	25	2	62
20161122114139.910	22	35	0	57
20161123054748.150	25	32	2	59
20161130004322.510	37	18	1	56
20161122082716.550	27	32	1	60
20161127053859.540	30	33	0	63
20161105190554.800	32	23	5	60
20161128103144.820	39	24	0	63
20161129062934.130	31	30	0	61
20161122124507.380	23	33	4	60
20161122234914.200	29	29	2	60
20161110095951.670	30	28	1	59
20161123162734.300	13	33	1	47
20161124114121.020	30	27	4	61
20161125033151.580	26	25	9	60
20161103103924.780	37	21	1	59
20161127174203.560	34	28	0	62
20161122054155.950	29	32	0	61
20161109225452.840	32	29	5	66
20161110045219.450	33	30	1	64
20161122100004.490	24	30	1	55
20161130204220.240	24	11	3	38
20161122094116.900	29	31	0	60
20161122201745.100	17	33	9	59
20161105142204.470	35	25	1	61
20161107190210.440	23	31	10	64
20161109043008.840	34	29	1	64
20161122104310.510	20	32	1	53
20161124041925.220	31	29	2	62
20161125103647.080	33	20	2	55
20161125220631.120	24	29	6	59
20161129232719.840	32	19	5	56
20161103092313.360	35	16	6	57
20161106081818.870	34	19	2	55
20161122133402.620	27	25	7	59
20161120174830.760	31	30	1	62
20161122025658.740	29	32	0	61
20161122193258.200	23	35	6	64
20161125022842.720	30	31	1	62
20161129024743.160	30	28	6	64
20161105170516.800	17	9	21	47
20161128152950.020	33	30	2	65
20161128232614.640	20	27	7	54
20161129043634.690	31	32	0	63
20161130192340.520	27	13	3	43
20161130212808.740	25	7	3	35

20161110090639.470	26	28	3	57
20161123031300.690	30	30	2	62
20161126165253.470	19	34	8	61
20161128090833.480	39	22	1	62
20161130061618.220	35	23	0	58
20161130231829.880	21	0	6	27
20161103090235.220	41	18	1	60
20161111114204.210	31	30	1	62
20161125080959.220	39	22	2	63
20161108213326.040	24	19	16	59
20161122110314.520	25	30	6	61
20161122142501.650	34	24	1	59
20161110031035.200	28	25	7	60
20161127070559.240	30	34	0	64
20161128100152.720	30	27	2	59
20161105210657.920	22	27	12	61
20161122120956.630	24	33	0	57
20161122125832.460	18	34	1	53
20161122131122.230	31	21	5	57
20161123142910.200	24	35	2	61
20161130000822.780	35	21	1	57
20161130190244.000	30	14	0	44
20161103091323.390	38	19	3	60
20161105210656.120	28	19	13	60
20161122153038.120	34	23	0	57
20161122220343.640	23	33	2	58
20161123123120.370	32	30	0	62
20161126090252.320	30	24	1	55
20161122200055.560	26	34	4	64
20161128070436.590	35	26	2	63
20161128223548.560	26	25	9	60
20161130184305.740	17	14	12	43
20161130222325.340	22	3	4	29
20161105181519.980	31	26	6	63
20161110234432.560	28	27	10	65
20161128013854.830	38	23	1	62
20161129222818.920	33	18	8	59
20161130121422.320	35	23	0	58
20161130194507.580	24	13	4	41
20161105213639.960	32	23	6	61
20161129162829.850	26	27	9	62
20161106004251.060	37	22	2	61
20161110143528.270	31	26	4	61
20161121232019.320	35	23	2	60
20161124030727.390	36	26	0	62
20161127192431.760	23	32	9	64

20161129123135.980	33	21	6	60
20161130202045.220	25	11	5	41
20161130215417.720	20	5	7	32
20161130224708.240	26	2	0	28
20161127105310.170	27	27	10	64
20161129040204.270	29	25	6	60
20161130112405.080	26	23	10	59
20161103093736.270	36	19	2	57
20161103100858.620	37	18	4	59
20161105165232.000	29	22	7	58
20161110093430.320	34	28	1	63
20161122135417.350	28	26	5	59
20161122155830.700	29	21	8	58
20161122171549.980	18	14	16	48
20161130191429.200	27	11	2	40
20161101014855.150	35	22	1	58
20161129090645.280	29	31	3	63
20161130235036.120	22	4	2	28
20161103095905.070	38	17	5	60
20161123005237.000	32	27	0	59
20161123041248.800	25	29	5	59
20161105174947.600	29	23	9	61
20161112171011.400	26	22	9	57
20161119043353.720	35	22	5	62
20161122092550.070	22	24	1	47
20161123080243.390	27	33	3	63
20161123172550.640	27	30	5	62
20161123194545.800	14	31	11	56
20161103113425.270	37	17	3	57
20161106023359.070	39	18	2	59
20161107112627.310	34	27	2	63
20161122112111.190	6	6	0	12
20161105145728.010	26	27	7	60
20161122110303.780	30	31	1	62
20161125002430.640	20	26	8	54
20161130193138.840	22	15	6	43
20161101033751.790	34	20	2	56
20161107110551.530	27	29	10	66
20161122213052.760	19	32	12	63
20161129104654.440	41	14	6	61
20161106044609.820	39	19	2	60
20161110103906.120	31	26	4	61
20161122050253.390	24	31	7	62
20161128151047.400	32	24	5	61
20161105161550.920	30	20	5	55
20161111091023.760	30	21	7	58

20161113060754.000	31	27	7	65
20161122043948.240	33	24	2	59
20161122125019.270	30	26	0	56
20161127020128.430	31	24	5	60
20161128004222.370	29	27	3	59
20161128045908.970	37	25	2	64
20161103084525.280	33	20	7	60
20161106025958.650	38	19	3	60
20161123002249.700	29	30	2	61
20161123023135.080	33	23	2	58
20161127042324.690	38	25	0	63
20161128101159.780	28	25	8	61
20161110094624.840	31	30	2	63
20161110222605.960	23	29	10	62
20161121232043.560	28	29	6	63
20161122131303.530	27	30	3	60
20161125045326.380	33	24	2	59
20161130183127.880	20	16	10	46
20161105195356.440	27	20	12	59
20161108172656.100	27	27	10	64
20161122041646.330	22	18	17	57
20161123130253.500	19	31	11	61
20161129035338.530	29	22	2	53
20161101180516.600	36	17	6	59
20161108054435.090	24	26	16	66
20161122091356.950	26	35	1	62
20161122113105.380	23	27	6	56
20161127213349.060	15	31	16	62
20161130193811.200	25	13	2	40

Appendix B: Focal Mechanisms for Comparison

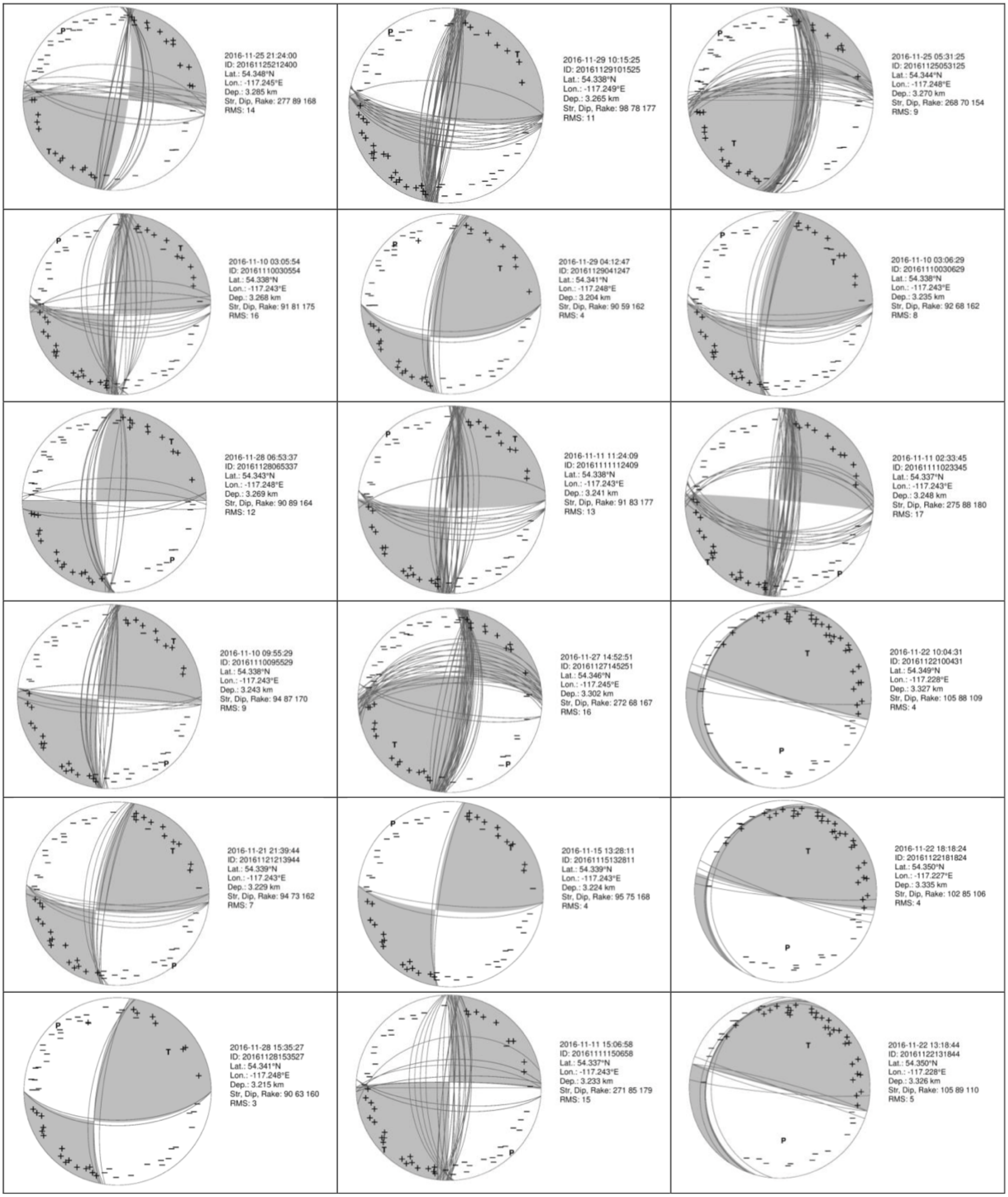

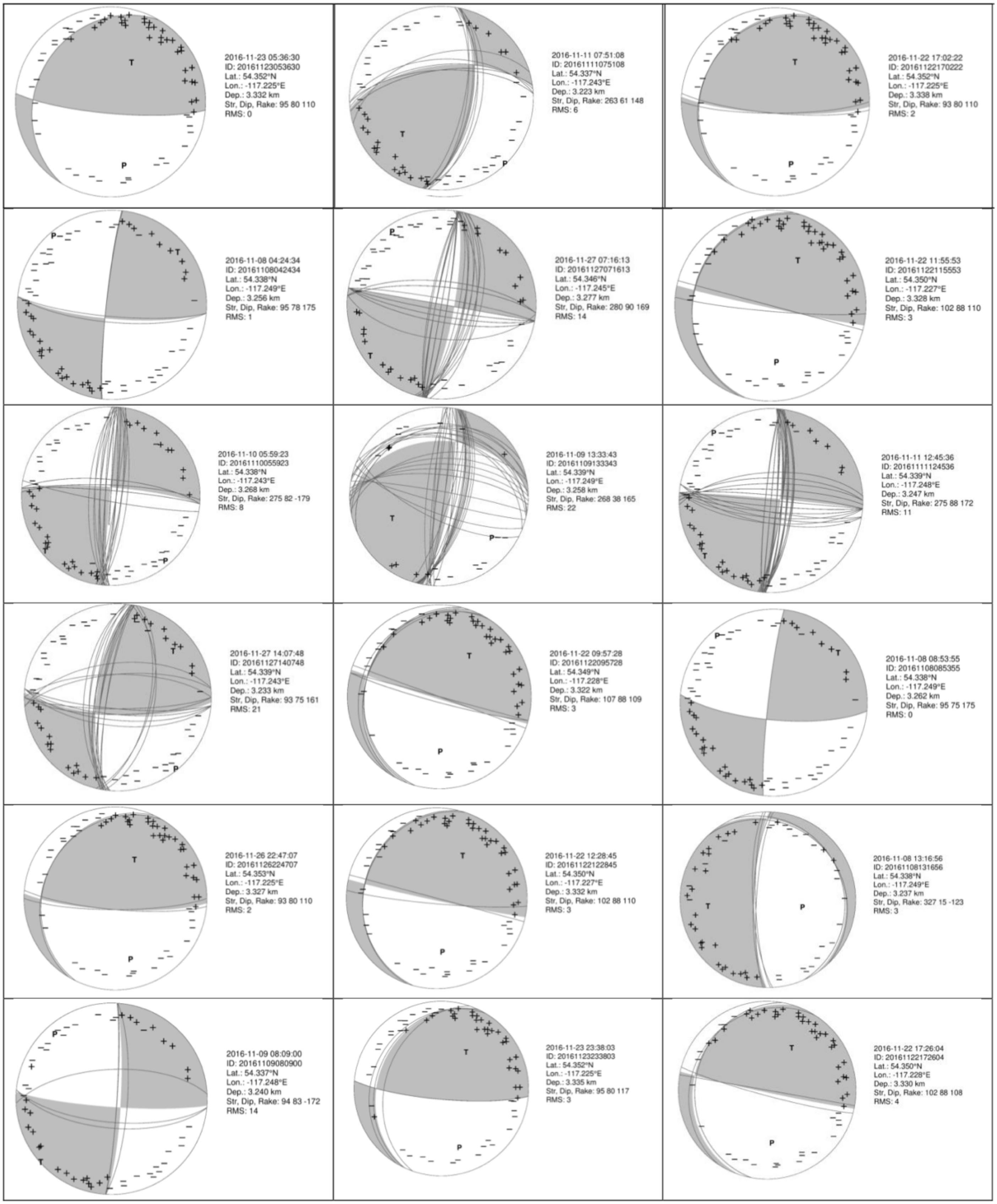
2016-11-23 05:36:30
ID: 20161123053630
Lat.: 54.352°N
Lon.: -117.225°E
Dep.: 3.332 km
Str, Dip, Rake: 95 80 110
RMS: 0
2016-11-11 07:51:08
ID: 20161111075108
Lat.: 54.337°N
Lon.: -117.243°E
Dep.: 3.223 km
Str, Dip, Rake: 263 61 148
RMS: 6
2016-11-22 17:02:22
ID: 20161122170222
Lat.: 54.352°N
Lon.: -117.225°E
Dep.: 3.338 km
Str, Dip, Rake: 93 80 110
RMS: 2
2016-11-08 04:24:34
ID: 20161108042434
Lat.: 54.338°N
Lon.: -117.249°E
Dep.: 3.256 km
Str, Dip, Rake: 95 78 175
RMS: 1
2016-11-27 07:16:13
ID: 20161127071613
Lat.: 54.346°N
Lon.: -117.245°E
Dep.: 3.277 km
Str, Dip, Rake: 280 90 169
RMS: 14
2016-11-22 11:55:53
ID: 20161122115553
Lat.: 54.350°N
Lon.: -117.227°E
Dep.: 3.328 km
Str, Dip, Rake: 102 88 110
RMS: 3
2016-11-10 05:59:23
ID: 20161110055923
Lat.: 54.338°N
Lon.: -117.243°E
Dep.: 3.268 km
Str, Dip, Rake: 275 82 -179
RMS: 8
2016-11-09 13:33:43
ID: 20161109133343
Lat.: 54.339°N
Lon.: -117.249°E
Dep.: 3.258 km
Str, Dip, Rake: 268 38 165
RMS: 22
2016-11-11 12:45:36
ID: 20161111124536
Lat.: 54.339°N
Lon.: -117.248°E
Dep.: 3.247 km
Str, Dip, Rake: 275 88 172
RMS: 11
2016-11-27 14:07:48
ID: 20161127140748
Lat.: 54.339°N
Lon.: -117.243°E
Dep.: 3.233 km
Str, Dip, Rake: 93 75 161
RMS: 21
2016-11-22 09:57:28
ID: 20161122095728
Lat.: 54.349°N
Lon.: -117.228°E
Dep.: 3.322 km
Str, Dip, Rake: 107 88 109
RMS: 3
2016-11-08 08:53:55
ID: 20161108085355
Lat.: 54.338°N
Lon.: -117.249°E
Dep.: 3.262 km
Str, Dip, Rake: 95 75 175
RMS: 0
2016-11-26 22:47:07
ID: 20161126224707
Lat.: 54.353°N
Lon.: -117.225°E
Dep.: 3.327 km
Str, Dip, Rake: 93 80 110
RMS: 2
2016-11-22 12:28:45
ID: 20161122122845
Lat.: 54.350°N
Lon.: -117.227°E
Dep.: 3.332 km
Str, Dip, Rake: 102 88 110
RMS: 3
2016-11-08 13:16:56
ID: 20161108131656
Lat.: 54.338°N
Lon.: -117.249°E
Dep.: 3.237 km
Str, Dip, Rake: 327 15 -123
RMS: 3
2016-11-09 08:09:00
ID: 20161109080900
Lat.: 54.337°N
Lon.: -117.248°E
Dep.: 3.240 km
Str, Dip, Rake: 94 83 -172
RMS: 14
2016-11-23 23:38:03
ID: 20161123233803
Lat.: 54.352°N
Lon.: -117.225°E
Dep.: 3.335 km
Str, Dip, Rake: 95 80 117
RMS: 3
2016-11-22 17:26:04
ID: 20161122172604
Lat.: 54.350°N
Lon.: -117.228°E
Dep.: 3.330 km
Str, Dip, Rake: 102 88 108
RMS: 4

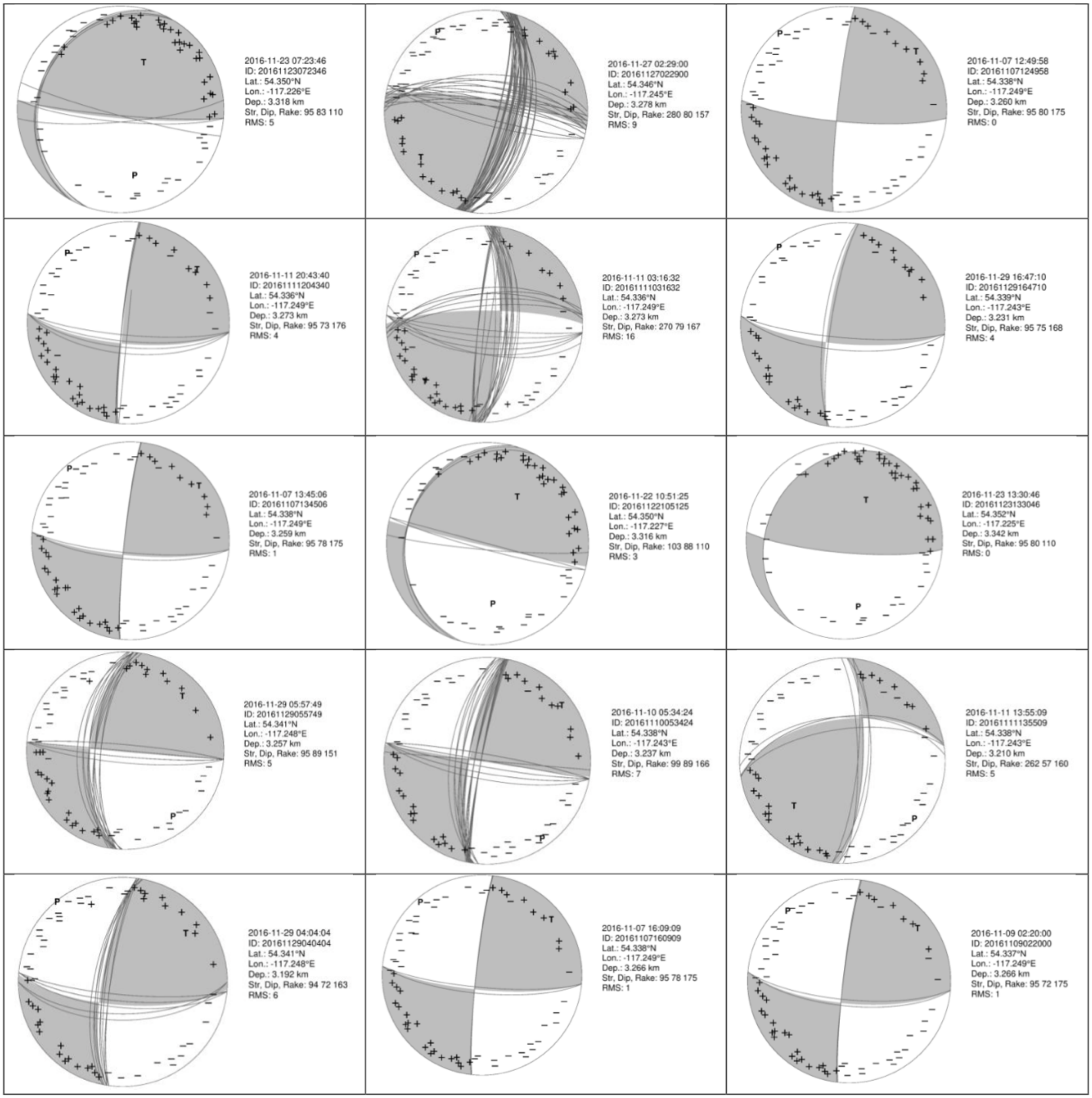

2016-11-23 07:23:46
ID: 20161123072346
Lat.: 54.350°N
Lon.: -117.226°E
Dep.: 3.318 km
Str, Dip, Rake: 95 83 110
RMS: 5
2016-11-27 02:29:00
ID: 20161127022900
Lat.: 54.346°N
Lon.: -117.245°E
Dep.: 3.278 km
Str, Dip, Rake: 280 80 157
RMS: 9
2016-11-07 12:49:58
ID: 20161107124958
Lat.: 54.338°N
Lon.: -117.249°E
Dep.: 3.260 km
Str, Dip, Rake: 95 80 175
RMS: 0
2016-11-11 20:43:40
ID: 20161111204340
Lat.: 54.336°N
Lon.: -117.249°E
Dep.: 3.273 km
Str, Dip, Rake: 95 73 176
RMS: 4
2016-11-11 03:16:32
ID: 20161111031632
Lat.: 54.336°N
Lon.: -117.249°E
Dep.: 3.273 km
Str, Dip, Rake: 270 79 167
RMS: 16
2016-11-29 16:47:10
ID: 20161129164710
Lat.: 54.339°N
Lon.: -117.243°E
Dep.: 3.231 km
Str, Dip, Rake: 95 75 168
RMS: 4
2016-11-07 13:45:06
ID: 20161107134506
Lat.: 54.338°N
Lon.: -117.249°E
Dep.: 3.259 km
Str, Dip, Rake: 95 78 175
RMS: 1
2016-11-22 10:51:25
ID: 20161122105125
Lat.: 54.350°N
Lon.: -117.227°E
Dep.: 3.316 km
Str, Dip, Rake: 103 88 110
RMS: 3
2016-11-23 13:30:46
ID: 20161123133046
Lat.: 54.352°N
Lon.: -117.225°E
Dep.: 3.342 km
Str, Dip, Rake: 95 80 110
RMS: 0
2016-11-29 05:57:49
ID: 20161129055749
Lat.: 54.341°N
Lon.: -117.248°E
Dep.: 3.257 km
Str, Dip, Rake: 95 89 151
RMS: 5
2016-11-10 05:34:24
ID: 20161110053424
Lat.: 54.338°N
Lon.: -117.243°E
Dep.: 3.237 km
Str, Dip, Rake: 99 89 166
RMS: 7
2016-11-11 13:55:09
ID: 20161111135509
Lat.: 54.338°N
Lon.: -117.243°E
Dep.: 3.210 km
Str, Dip, Rake: 262 57 160
RMS: 5
2016-11-29 04:04:04
ID: 20161129040404
Lat.: 54.341°N
Lon.: -117.248°E
Dep.: 3.192 km
Str, Dip, Rake: 94 72 163
RMS: 6
2016-11-07 16:09:09
ID: 20161107160909
Lat.: 54.338°N
Lon.: -117.249°E
Dep.: 3.266 km
Str, Dip, Rake: 95 78 175
RMS: 1
2016-11-09 02:20:00
ID: 20161109022000
Lat.: 54.337°N
Lon.: -117.249°E
Dep.: 3.266 km
Str, Dip, Rake: 95 72 175
RMS: 1

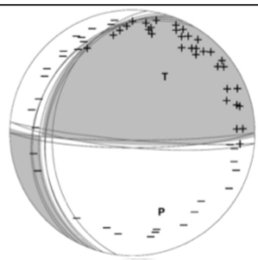

2016-11-27 05:38:59
ID: 20161127053859
Lat.: 54.353°N
Lon.: -117.225°E
Dep.: 3.343 km
Str, Dip, Rake: 92 82 117
RMS: 5

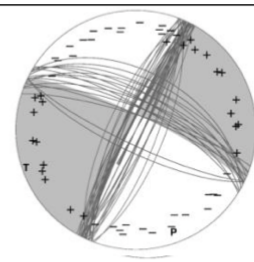

2016-11-05 19:05:54
ID: 20161105190554
Lat.: 54.346°N
Lon.: -117.239°E
Dep.: 3.410 km
Str, Dip, Rake: 296 80 -176
RMS: 12

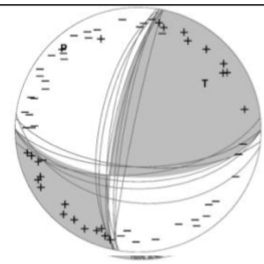

2016-11-28 10:31:44
ID: 20161128103144
Lat.: 54.341°N
Lon.: -117.248°E
Dep.: 3.212 km
Str, Dip, Rake: 91 58 162
RMS: 8

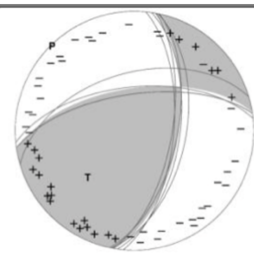

2016-11-10 07:06:28
ID: 20161110070628
Lat.: 54.337°N
Lon.: -117.243°E
Dep.: 3.223 km
Str, Dip, Rake: 261 61 145
RMS: 5

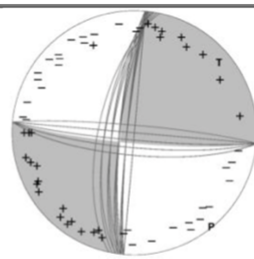

2016-11-29 01:35:55
ID: 20161129013555
Lat.: 54.341°N
Lon.: -117.248°E
Dep.: 3.251 km
Str, Dip, Rake: 95 83 171
RMS: 7

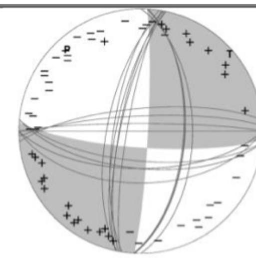

2016-11-29 02:32:35
ID: 20161129023235
Lat.: 54.341°N
Lon.: -117.248°E
Dep.: 3.230 km
Str, Dip, Rake: 94 79 -175
RMS: 21

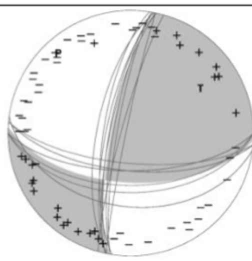

2016-11-23 12:36:18
ID: 20161123123618
Lat.: 54.341°N
Lon.: -117.248°E
Dep.: 3.248 km
Str, Dip, Rake: 93 57 165
RMS: 9

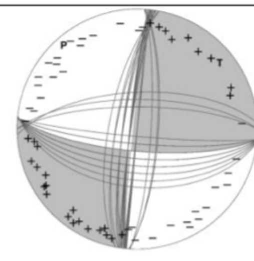

2016-11-14 02:24:25
ID: 20161114022425
Lat.: 54.338°N
Lon.: -117.249°E
Dep.: 3.227 km
Str, Dip, Rake: 95 75 177
RMS: 12

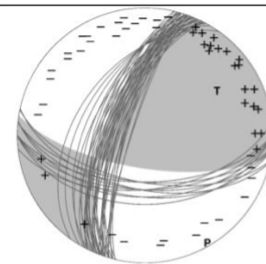

2016-11-24 06:37:32
ID: 20161124063732
Lat.: 54.352°N
Lon.: -117.227°E
Dep.: 3.276 km
Str, Dip, Rake: 99 69 153
RMS: 20

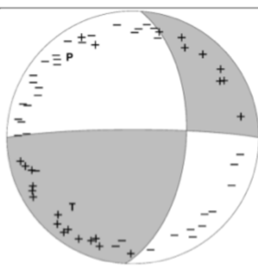

2016-11-23 19:04:45
ID: 20161123190445
Lat.: 54.341°N
Lon.: -117.248°E
Dep.: 3.248 km
Str, Dip, Rake: 270 85 145
RMS: 0

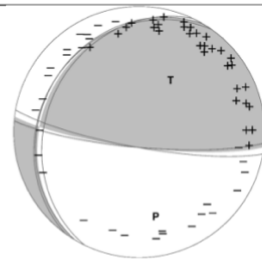

2016-11-23 05:41:15
ID: 20161123054115
Lat.: 54.352°N
Lon.: -117.225°E
Dep.: 3.348 km
Str, Dip, Rake: 97 80 112
RMS: 3

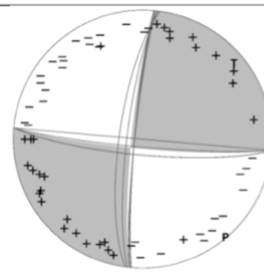

2016-11-29 00:20:23
ID: 20161129002023
Lat.: 54.341°N
Lon.: -117.248°E
Dep.: 3.248 km
Str, Dip, Rake: 95 84 173
RMS: 4

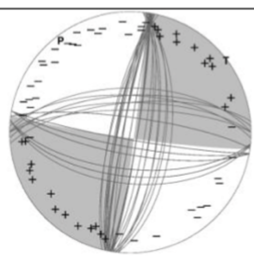

2016-11-26 04:26:30
ID: 20161126042630
Lat.: 54.346°N
Lon.: -117.245°E
Dep.: 3.250 km
Str, Dip, Rake: 98 86 -177
RMS: 16

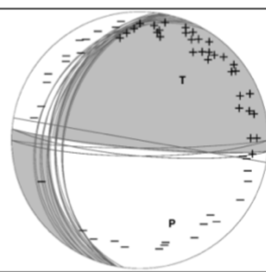

2016-11-24 17:31:42
ID: 20161124173142
Lat.: 54.352°N
Lon.: -117.225°E
Dep.: 3.328 km
Str, Dip, Rake: 95 84 122
RMS: 6

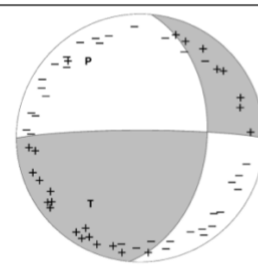

2016-11-11 11:35:17
ID: 20161111113517
Lat.: 54.339°N
Lon.: -117.243°E
Dep.: 3.209 km
Str, Dip, Rake: 270 85 135
RMS: 0

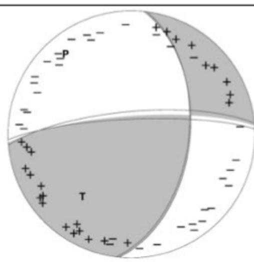

2016-11-15 13:33:35
ID: 20161115133335
Lat.: 54.339°N
Lon.: -117.243°E
Dep.: 3.247 km
Str, Dip, Rake: 266 78 140
RMS: 2

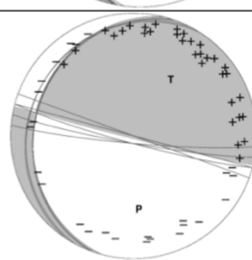

2016-11-23 05:47:48
ID: 20161123054748
Lat.: 54.350°N
Lon.: -117.227°E
Dep.: 3.326 km
Str, Dip, Rake: 104 88 109
RMS: 4

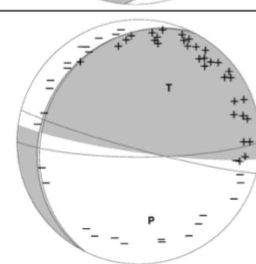

2016-11-22 08:27:16
ID: 20161122082716
Lat.: 54.352°N
Lon.: -117.225°E
Dep.: 3.323 km
Str, Dip, Rake: 98 83 110
RMS: 4

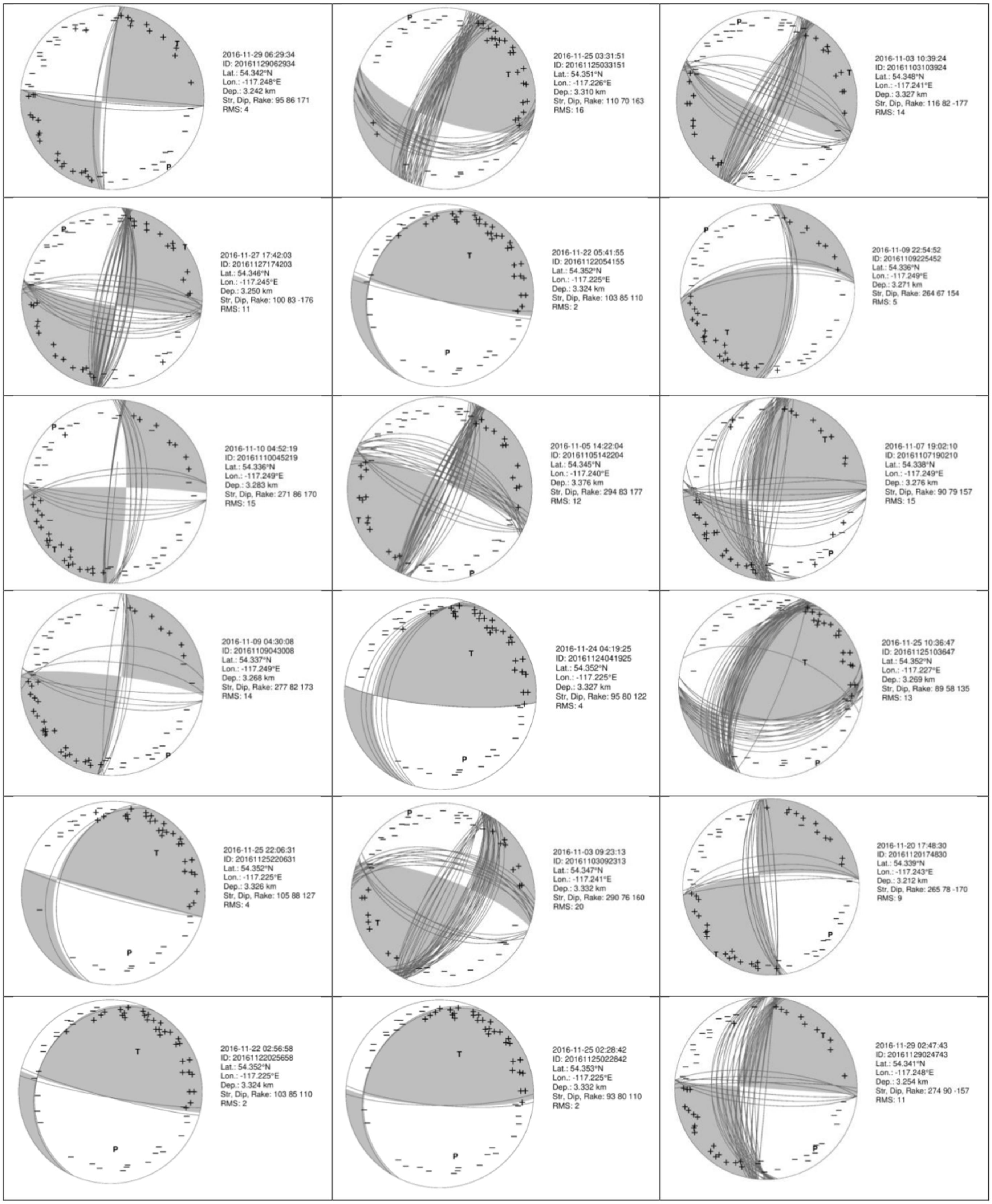
2016-11-29 06:29:34
ID: 20161129062934
Lat.: 54.342°N
Lon.: -117.248°E
Dep.: 3.242 km
Str, Dip, Rake: 95 86 171
RMS: 4
2016-11-25 03:31:51
ID: 20161125033151
Lat.: 54.351°N
Lon.: -117.226°E
Dep.: 3.310 km
Str, Dip, Rake: 110 70 163
RMS: 16
2016-11-03 10:39:24
ID: 20161103103924
Lat.: 54.348°N
Lon.: -117.241°E
Dep.: 3.327 km
Str, Dip, Rake: 116 82 -177
RMS: 14
2016-11-27 17:42:03
ID: 20161127174203
Lat.: 54.346°N
Lon.: -117.245°E
Dep.: 3.250 km
Str, Dip, Rake: 100 83 -176
RMS: 11
2016-11-22 05:41:55
ID: 20161122054155
Lat.: 54.352°N
Lon.: -117.225°E
Dep.: 3.324 km
Str, Dip, Rake: 103 85 110
RMS: 2
2016-11-09 22:54:52
ID: 20161109225452
Lat.: 54.336°N
Lon.: -117.249°E
Dep.: 3.271 km
Str, Dip, Rake: 264 67 154
RMS: 5
2016-11-10 04:52:19
ID: 20161110045219
Lat.: 54.336°N
Lon.: -117.249°E
Dep.: 3.283 km
Str, Dip, Rake: 271 86 170
RMS: 15
2016-11-05 14:22:04
ID: 20161105142204
Lat.: 54.345°N
Lon.: -117.240°E
Dep.: 3.376 km
Str, Dip, Rake: 294 83 177
RMS: 12
2016-11-07 19:02:10
ID: 20161107190210
Lat.: 54.338°N
Lon.: -117.249°E
Dep.: 3.276 km
Str, Dip, Rake: 90 79 157
RMS: 15
2016-11-09 04:30:08
ID: 20161109043008
Lat.: 54.337°N
Lon.: -117.249°E
Dep.: 3.268 km
Str, Dip, Rake: 277 82 173
RMS: 14
2016-11-24 04:19:25
ID: 20161124041925
Lat.: 54.352°N
Lon.: -117.225°E
Dep.: 3.327 km
Str, Dip, Rake: 95 80 122
RMS: 4
2016-11-25 10:36:47
ID: 20161125103647
Lat.: 54.352°N
Lon.: -117.227°E
Dep.: 3.269 km
Str, Dip, Rake: 89 58 135
RMS: 13
2016-11-25 22:06:31
ID: 20161125220631
Lat.: 54.352°N
Lon.: -117.225°E
Dep.: 3.326 km
Str, Dip, Rake: 105 88 127
RMS: 4
2016-11-03 09:23:13
ID: 20161103092313
Lat.: 54.347°N
Lon.: -117.241°E
Dep.: 3.332 km
Str, Dip, Rake: 290 76 160
RMS: 20
2016-11-20 17:48:30
ID: 20161120174830
Lat.: 54.339°N
Lon.: -117.243°E
Dep.: 3.212 km
Str, Dip, Rake: 265 78 -170
RMS: 9
2016-11-22 02:56:58
ID: 20161122025658
Lat.: 54.352°N
Lon.: -117.225°E
Dep.: 3.324 km
Str, Dip, Rake: 103 85 110
RMS: 2
2016-11-25 02:28:42
ID: 20161125022842
Lat.: 54.353°N
Lon.: -117.225°E
Dep.: 3.332 km
Str, Dip, Rake: 93 80 110
RMS: 2
2016-11-29 02:47:43
ID: 20161129024743
Lat.: 54.341°N
Lon.: -117.248°E
Dep.: 3.254 km
Str, Dip, Rake: 274 90 -157
RMS: 11

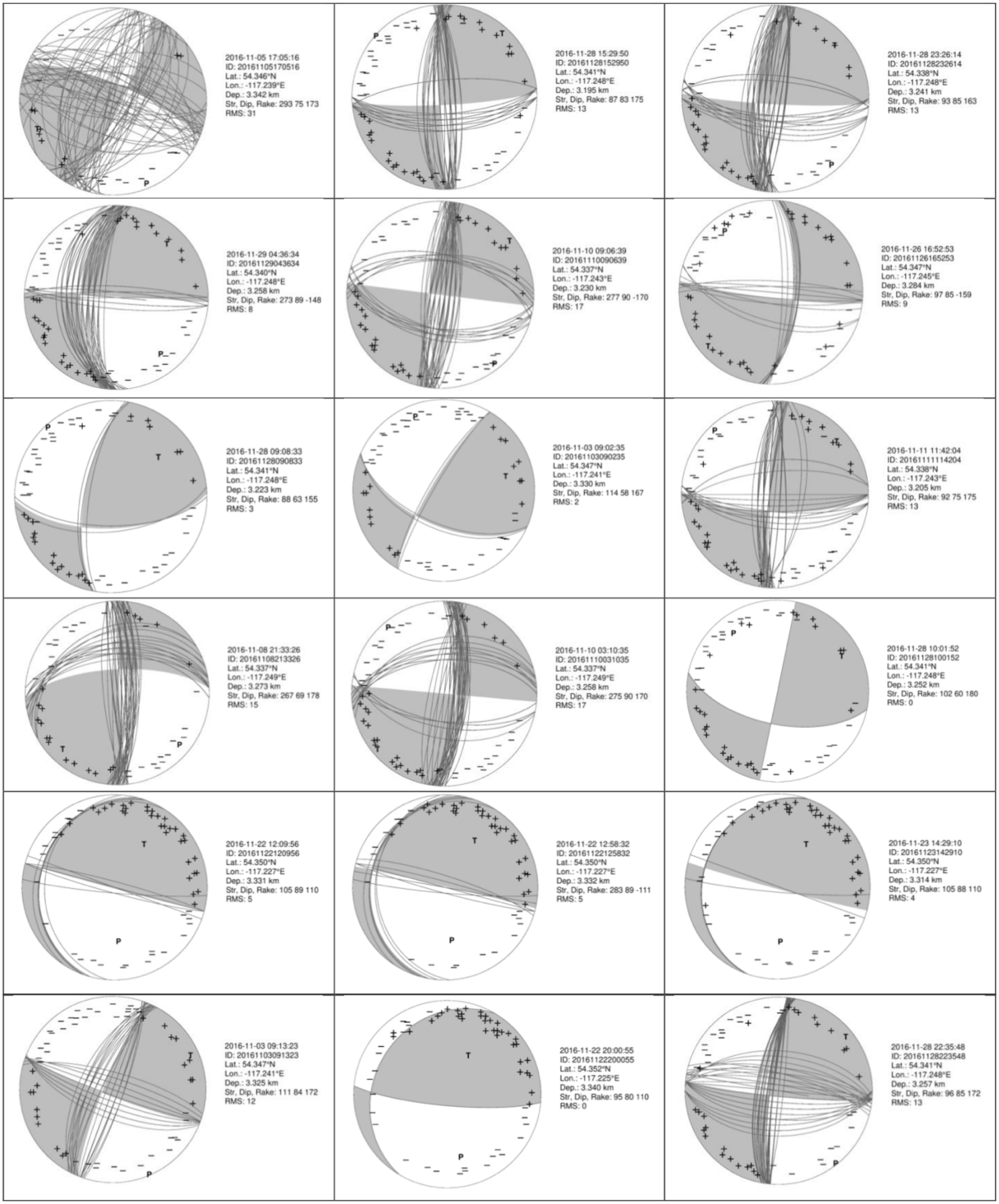
2016-11-05 17:05:16
ID: 20161105170516
Lat.: 54.346°N
Lon.: -117.239°E
Dep.: 3.342 km
Str, Dip, Rake: 293 75 173
RMS: 31
2016-11-28 15:29:50
ID: 20161128152950
Lat.: 54.341°N
Lon.: -117.248°E
Dep.: 3.195 km
Str, Dip, Rake: 87 83 175
RMS: 13
2016-11-28 23:26:14
ID: 20161128232614
Lat.: 54.338°N
Lon.: -117.248°E
Dep.: 3.241 km
Str, Dip, Rake: 93 85 163
RMS: 13
2016-11-29 04:36:34
ID: 20161129043634
Lat.: 54.340°N
Lon.: -117.248°E
Dep.: 3.258 km
Str, Dip, Rake: 273 89 -148
RMS: 8
2016-11-10 09:06:39
ID: 20161110090639
Lat.: 54.337°N
Lon.: -117.243°E
Dep.: 3.230 km
Str, Dip, Rake: 277 90 -170
RMS: 17
2016-11-26 16:52:53
ID: 20161126165253
Lat.: 54.347°N
Lon.: -117.245°E
Dep.: 3.284 km
Str, Dip, Rake: 97 85 -159
RMS: 9
2016-11-28 09:08:33
ID: 20161128090833
Lat.: 54.341°N
Lon.: -117.248°E
Dep.: 3.223 km
Str, Dip, Rake: 88 63 155
RMS: 3
2016-11-03 09:02:35
ID: 20161103090235
Lat.: 54.347°N
Lon.: -117.241°E
Dep.: 3.330 km
Str, Dip, Rake: 114 58 167
RMS: 2
2016-11-11 11:42:04
ID: 20161111114204
Lat.: 54.338°N
Lon.: -117.243°E
Dep.: 3.205 km
Str, Dip, Rake: 92 75 175
RMS: 13
2016-11-08 21:33:26
ID: 20161108213326
Lat.: 54.337°N
Lon.: -117.249°E
Dep.: 3.273 km
Str, Dip, Rake: 267 69 178
RMS: 15
2016-11-10 03:10:35
ID: 20161110031035
Lat.: 54.337°N
Lon.: -117.249°E
Dep.: 3.258 km
Str, Dip, Rake: 275 90 170
RMS: 17
2016-11-28 10:01:52
ID: 20161128100152
Lat.: 54.341°N
Lon.: -117.248°E
Dep.: 3.252 km
Str, Dip, Rake: 102 60 180
RMS: 0
2016-11-22 12:09:56
ID: 20161122120956
Lat.: 54.350°N
Lon.: -117.227°E
Dep.: 3.331 km
Str, Dip, Rake: 105 89 110
RMS: 5
2016-11-22 12:58:32
ID: 20161122125832
Lat.: 54.350°N
Lon.: -117.227°E
Dep.: 3.332 km
Str, Dip, Rake: 283 89 -111
RMS: 5
2016-11-23 14:29:10
ID: 20161123142910
Lat.: 54.350°N
Lon.: -117.227°E
Dep.: 3.314 km
Str, Dip, Rake: 105 88 110
RMS: 4
2016-11-03 09:13:23
ID: 20161103091323
Lat.: 54.347°N
Lon.: -117.241°E
Dep.: 3.325 km
Str, Dip, Rake: 111 84 172
RMS: 12
2016-11-22 20:00:55
ID: 20161122200055
Lat.: 54.352°N
Lon.: -117.225°E
Dep.: 3.340 km
Str, Dip, Rake: 95 80 110
RMS: 0
2016-11-28 22:35:48
ID: 20161128223548
Lat.: 54.341°N
Lon.: -117.248°E
Dep.: 3.257 km
Str, Dip, Rake: 96 85 172
RMS: 13

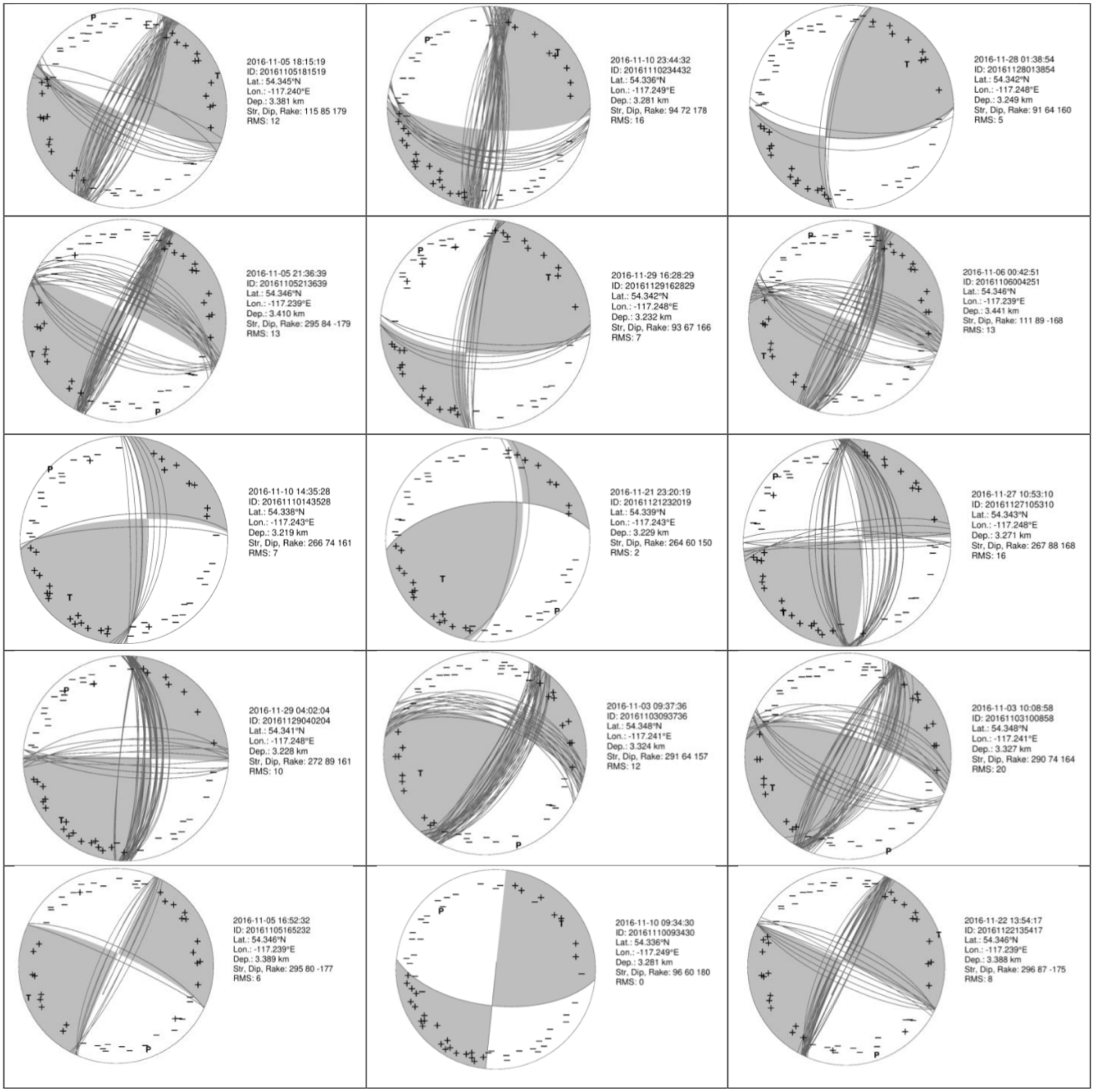
2016-11-05 18:15:19
ID: 20161105181519
Lat.: 54.345°N
Lon.: -117.240°E
Dep.: 3.381 km
Str, Dip, Rake: 115 85 179
RMS: 12
2016-11-10 23:44:32
ID: 20161110234432
Lat.: 54.336°N
Lon.: -117.249°E
Dep.: 3.281 km
Str, Dip, Rake: 94 72 178
RMS: 16
2016-11-28 01:38:54
ID: 20161128013854
Lat.: 54.342°N
Lon.: -117.248°E
Dep.: 3.249 km
Str, Dip, Rake: 91 64 160
RMS: 5
2016-11-05 21:36:39
ID: 20161105213639
Lat.: 54.346°N
Lon.: -117.239°E
Dep.: 3.410 km
Str, Dip, Rake: 295 84 -179
RMS: 13
2016-11-29 16:28:29
ID: 20161129162829
Lat.: 54.342°N
Lon.: -117.248°E
Dep.: 3.232 km
Str, Dip, Rake: 93 67 166
RMS: 7
2016-11-06 00:42:51
ID: 20161106004251
Lat.: 54.346°N
Lon.: -117.239°E
Dep.: 3.441 km
Str, Dip, Rake: 111 89 -168
RMS: 13
2016-11-10 14:35:28
ID: 20161110143528
Lat.: 54.338°N
Lon.: -117.243°E
Dep.: 3.219 km
Str, Dip, Rake: 266 74 161
RMS: 7
2016-11-21 23:20:19
ID: 20161121232019
Lat.: 54.339°N
Lon.: -117.243°E
Dep.: 3.229 km
Str, Dip, Rake: 264 60 150
RMS: 2
2016-11-27 10:53:10
ID: 20161127105310
Lat.: 54.343°N
Lon.: -117.248°E
Dep.: 3.271 km
Str, Dip, Rake: 267 88 168
RMS: 16
2016-11-29 04:02:04
ID: 20161129040204
Lat.: 54.341°N
Lon.: -117.248°E
Dep.: 3.228 km
Str, Dip, Rake: 272 89 161
RMS: 10
2016-11-03 09:37:36
ID: 20161103093736
Lat.: 54.348°N
Lon.: -117.241°E
Dep.: 3.324 km
Str, Dip, Rake: 291 64 157
RMS: 12
2016-11-03 10:08:58
ID: 20161103100858
Lat.: 54.348°N
Lon.: -117.241°E
Dep.: 3.327 km
Str, Dip, Rake: 290 74 164
RMS: 20
2016-11-05 16:52:32
ID: 20161105165232
Lat.: 54.346°N
Lon.: -117.239°E
Dep.: 3.389 km
Str, Dip, Rake: 295 80 -177
RMS: 6
2016-11-10 09:34:30
ID: 20161110093430
Lat.: 54.336°N
Lon.: -117.249°E
Dep.: 3.281 km
Str, Dip, Rake: 96 60 180
RMS: 0
2016-11-22 13:54:17
ID: 20161122135417
Lat.: 54.346°N
Lon.: -117.239°E
Dep.: 3.388 km
Str, Dip, Rake: 296 87 -175
RMS: 8

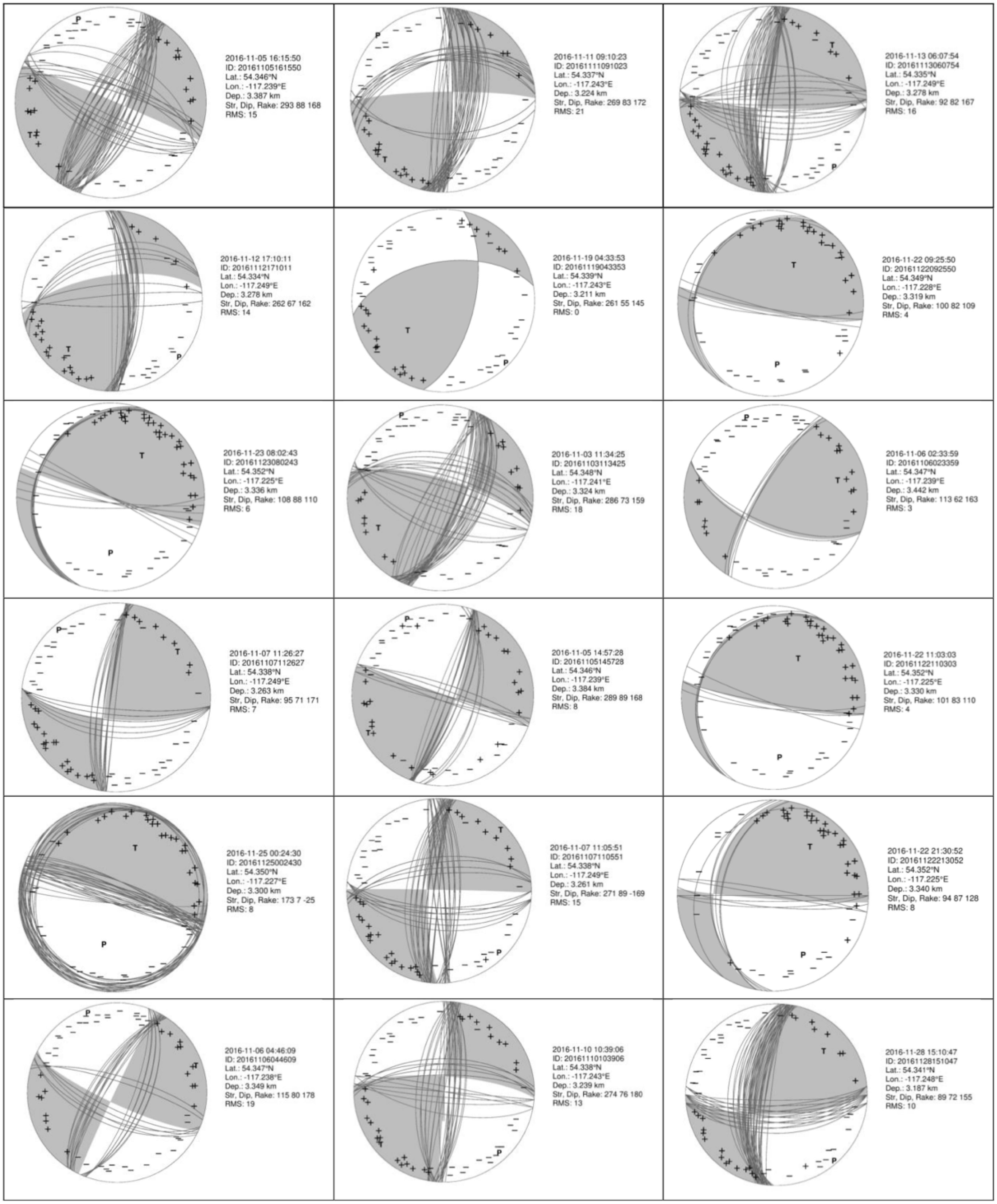
2016-11-05 16:15:50
ID: 20161105161550
Lat.: 54.346°N
Lon.: -117.239°E
Dep.: 3.387 km
Str, Dip, Rake: 293 88 168
RMS: 15
2016-11-11 09:10:23
ID: 20161111091023
Lat.: 54.337°N
Lon.: -117.243°E
Dep.: 3.224 km
Str, Dip, Rake: 269 83 172
RMS: 21
2016-11-13 06:07:54
ID: 20161113060754
Lat.: 54.335°N
Lon.: -117.249°E
Dep.: 3.278 km
Str, Dip, Rake: 92 82 167
RMS: 16
2016-11-12 17:10:11
ID: 20161112171011
Lat.: 54.334°N
Lon.: -117.249°E
Dep.: 3.278 km
Str, Dip, Rake: 262 67 162
RMS: 14
2016-11-19 04:33:53
ID: 20161119043353
Lat.: 54.339°N
Lon.: -117.243°E
Dep.: 3.211 km
Str, Dip, Rake: 261 55 145
RMS: 0
2016-11-22 09:25:50
ID: 20161122092550
Lat.: 54.349°N
Lon.: -117.228°E
Dep.: 3.319 km
Str, Dip, Rake: 100 82 109
RMS: 4
2016-11-23 08:02:43
ID: 20161123080243
Lat.: 54.352°N
Lon.: -117.225°E
Dep.: 3.336 km
Str, Dip, Rake: 108 88 110
RMS: 6
2016-11-03 11:34:25
ID: 20161103113425
Lat.: 54.348°N
Lon.: -117.241°E
Dep.: 3.324 km
Str, Dip, Rake: 286 73 159
RMS: 18
2016-11-06 02:33:59
ID: 20161106023359
Lat.: 54.347°N
Lon.: -117.239°E
Dep.: 3.442 km
Str, Dip, Rake: 113 62 163
RMS: 3
2016-11-07 11:26:27
ID: 20161107112627
Lat.: 54.338°N
Lon.: -117.249°E
Dep.: 3.263 km
Str, Dip, Rake: 95 71 171
RMS: 7
2016-11-05 14:57:28
ID: 20161105145728
Lat.: 54.346°N
Lon.: -117.239°E
Dep.: 3.384 km
Str, Dip, Rake: 289 89 168
RMS: 8
2016-11-22 11:03:03
ID: 20161122110303
Lat.: 54.352°N
Lon.: -117.225°E
Dep.: 3.330 km
Str, Dip, Rake: 101 83 110
RMS: 4
2016-11-25 00:24:30
ID: 20161125002430
Lat.: 54.350°N
Lon.: -117.227°E
Dep.: 3.300 km
Str, Dip, Rake: 173 7 -25
RMS: 8
2016-11-07 11:05:51
ID: 20161107110551
Lat.: 54.338°N
Lon.: -117.249°E
Dep.: 3.261 km
Str, Dip, Rake: 271 89 -169
RMS: 15
2016-11-22 21:30:52
ID: 20161122213052
Lat.: 54.352°N
Lon.: -117.225°E
Dep.: 3.340 km
Str, Dip, Rake: 94 87 128
RMS: 8
2016-11-06 04:46:09
ID: 20161106044609
Lat.: 54.347°N
Lon.: -117.238°E
Dep.: 3.349 km
Str, Dip, Rake: 115 80 178
RMS: 19
2016-11-10 10:39:06
ID: 20161110103906
Lat.: 54.338°N
Lon.: -117.243°E
Dep.: 3.239 km
Str, Dip, Rake: 274 76 180
RMS: 13
2016-11-28 15:10:47
ID: 20161128151047
Lat.: 54.341°N
Lon.: -117.248°E
Dep.: 3.187 km
Str, Dip, Rake: 89 72 155
RMS: 10

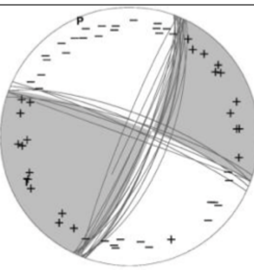

2016-11-22 04:39:48
ID: 20161122043948
Lat.: 54.346°N
Lon.: -117.239°E
Dep.: 3.420 km
Str, Dip, Rake: 291 82 168
RMS: 6

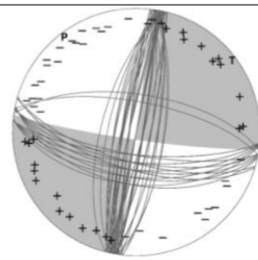

2016-11-27 02:01:28
ID: 20161127020128
Lat.: 54.346°N
Lon.: -117.245°E
Dep.: 3.275 km
Str, Dip, Rake: 98 85 180
RMS: 15

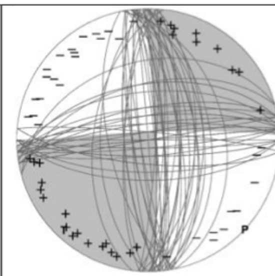

2016-11-28 00:42:22
ID: 20161128004222
Lat.: 54.343°N
Lon.: -117.248°E
Dep.: 3.233 km
Str, Dip, Rake: 268 85 175
RMS: 19

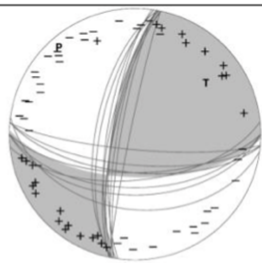

2016-11-28 04:59:08
ID: 20161128045908
Lat.: 54.342°N
Lon.: -117.248°E
Dep.: 3.209 km
Str, Dip, Rake: 92 62 163
RMS: 9

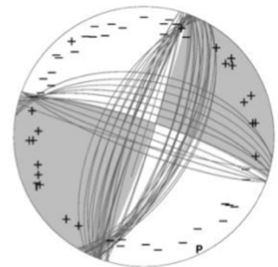

2016-11-03 08:45:25
ID: 20161103084525
Lat.: 54.347°N
Lon.: -117.241°E
Dep.: 3.325 km
Str, Dip, Rake: 289 80 176
RMS: 17

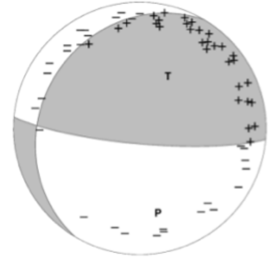

2016-11-23 00:22:49
ID: 20161123002249
Lat.: 54.352°N
Lon.: -117.225°E
Dep.: 3.328 km
Str, Dip, Rake: 95 80 110
RMS: 0

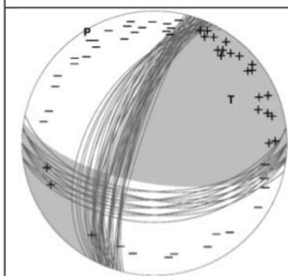

2016-11-23 02:31:35
ID: 20161123023135
Lat.: 54.352°N
Lon.: -117.227°E
Dep.: 3.271 km
Str, Dip, Rake: 99 65 156
RMS: 23

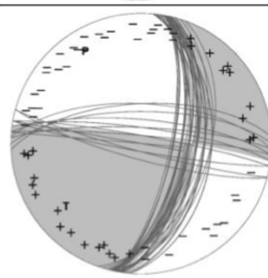

2016-11-27 04:23:24
ID: 20161127042324
Lat.: 54.346°N
Lon.: -117.245°E
Dep.: 3.268 km
Str, Dip, Rake: 278 85 148
RMS: 9

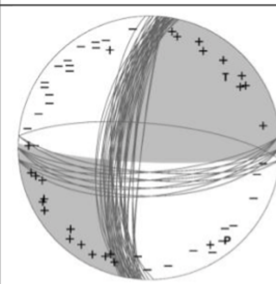

2016-11-28 10:11:59
ID: 20161128101159
Lat.: 54.342°N
Lon.: -117.248°E
Dep.: 3.180 km
Str, Dip, Rake: 92 81 158
RMS: 11

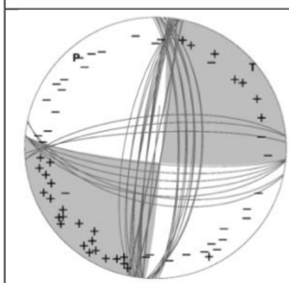

2016-11-10 09:46:24
ID: 20161110094624
Lat.: 54.335°N
Lon.: -117.249°E
Dep.: 3.281 km
Str, Dip, Rake: 95 81 -176
RMS: 18

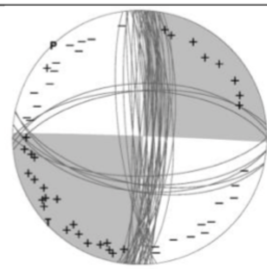

2016-11-10 22:26:05
ID: 20161110222605
Lat.: 54.338°N
Lon.: -117.249°E
Dep.: 3.245 km
Str, Dip, Rake: 272 89 178
RMS: 17

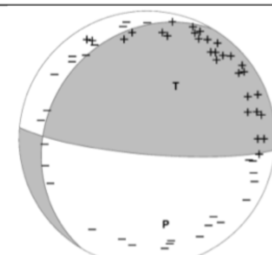

2016-11-21 23:20:43
ID: 20161121232043
Lat.: 54.352°N
Lon.: -117.226°E
Dep.: 3.323 km
Str, Dip, Rake: 95 80 110
RMS: 0

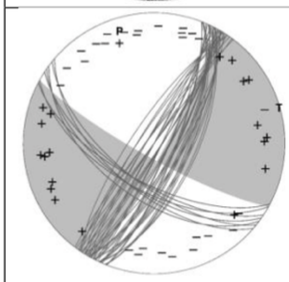

2016-11-05 19:53:56
ID: 20161105195356
Lat.: 54.346°N
Lon.: -117.239°E
Dep.: 3.361 km
Str, Dip, Rake: 119 81 -173
RMS: 14

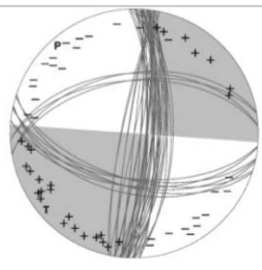

2016-11-08 17:26:56
ID: 20161108172656
Lat.: 54.339°N
Lon.: -117.249°E
Dep.: 3.254 km
Str, Dip, Rake: 94 90 -170
RMS: 18

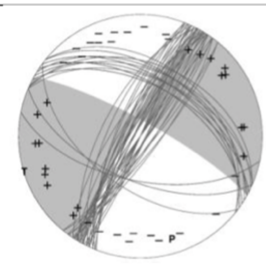

2016-11-22 04:16:46
ID: 20161122041646
Lat.: 54.347°N
Lon.: -117.238°E
Dep.: 3.422 km
Str, Dip, Rake: 299 80 -172
RMS: 16

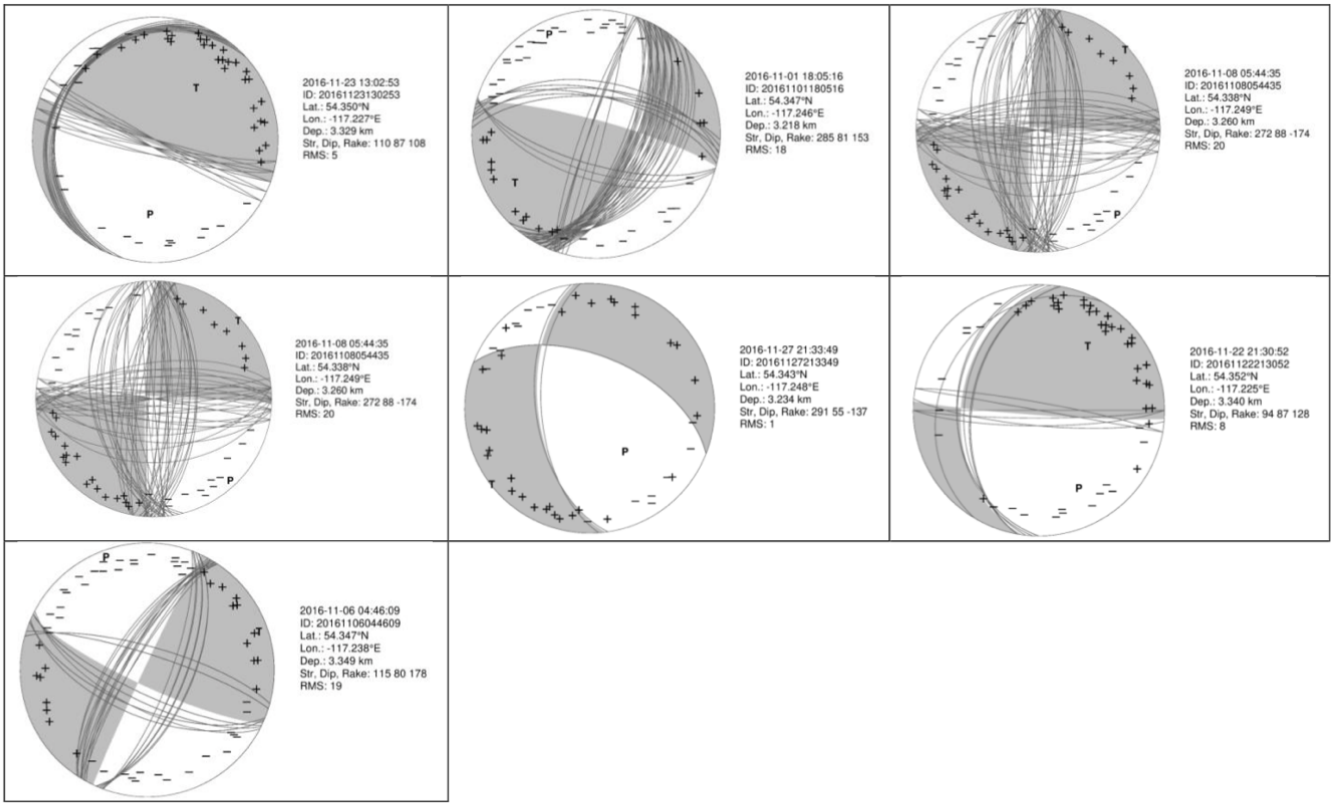
2016-11-23 13:02:53
ID: 20161123130253
Lat.: 54.350°N
Lon.: -117.227°E
Dep.: 3.329 km
Str, Dip, Rake: 110 87 108
RMS: 5
2016-11-01 18:05:16
ID: 20161101180516
Lat.: 54.347°N
Lon.: -117.246°E
Dep.: 3.218 km
Str, Dip, Rake: 285 81 153
RMS: 18
2016-11-08 05:44:35
ID: 20161108054435
Lat.: 54.338°N
Lon.: -117.249°E
Dep.: 3.260 km
Str, Dip, Rake: 272 88 -174
RMS: 20
2016-11-08 05:44:35
ID: 20161108054435
Lat.: 54.338°N
Lon.: -117.249°E
Dep.: 3.260 km
Str, Dip, Rake: 272 88 -174
RMS: 20
2016-11-27 21:33:49
ID: 20161127213349
Lat.: 54.343°N
Lon.: -117.248°E
Dep.: 3.234 km
Str, Dip, Rake: 291 55 -137
RMS: 1
2016-11-22 21:30:52
ID: 20161122213052
Lat.: 54.352°N
Lon.: -117.225°E
Dep.: 3.340 km
Str, Dip, Rake: 94 87 128
RMS: 8
2016-11-06 04:46:09
ID: 20161106044609
Lat.: 54.347°N
Lon.: -117.238°E
Dep.: 3.349 km
Str, Dip, Rake: 115 80 178
RMS: 19

Appendix C: Remaining Focal Mechanisms

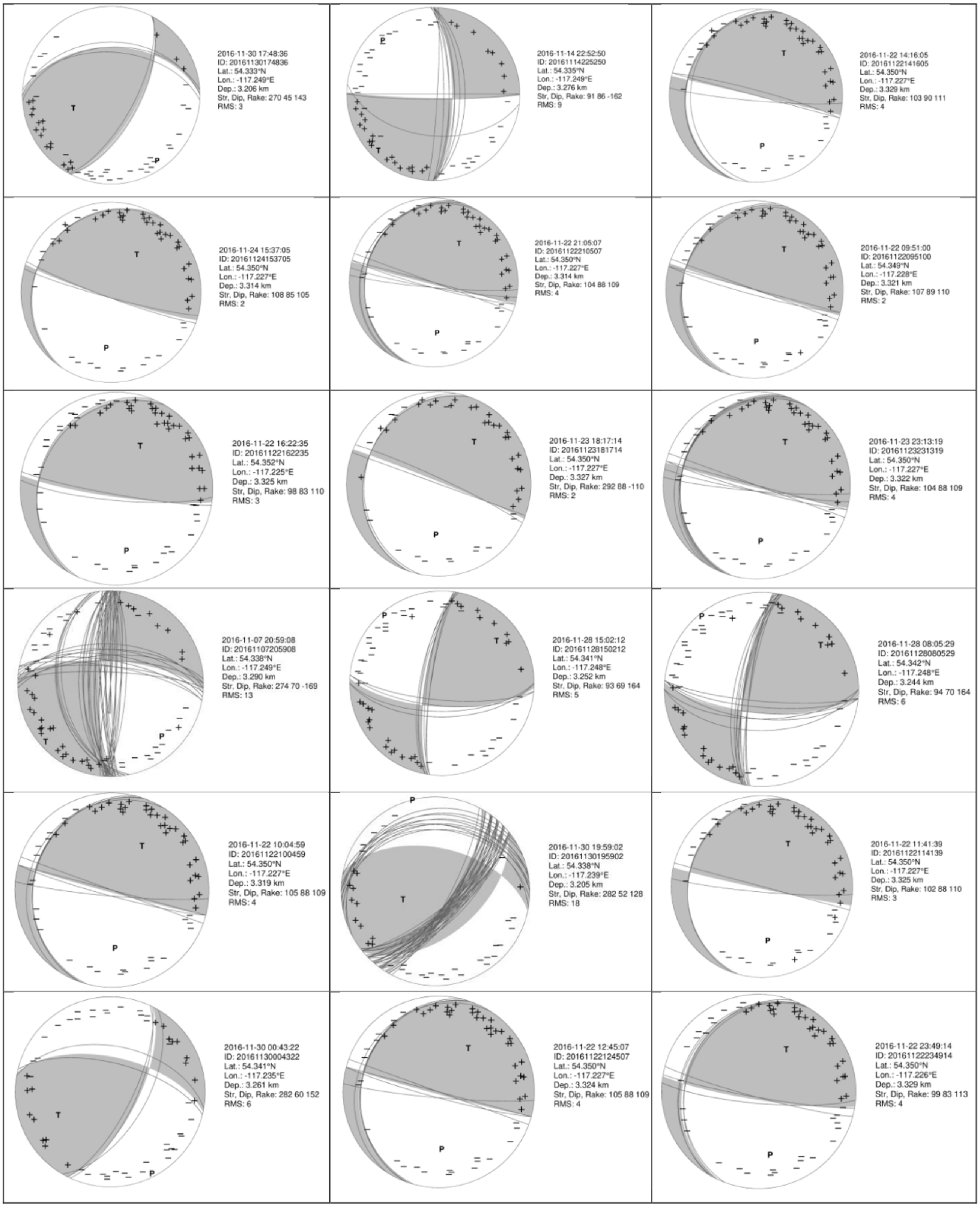

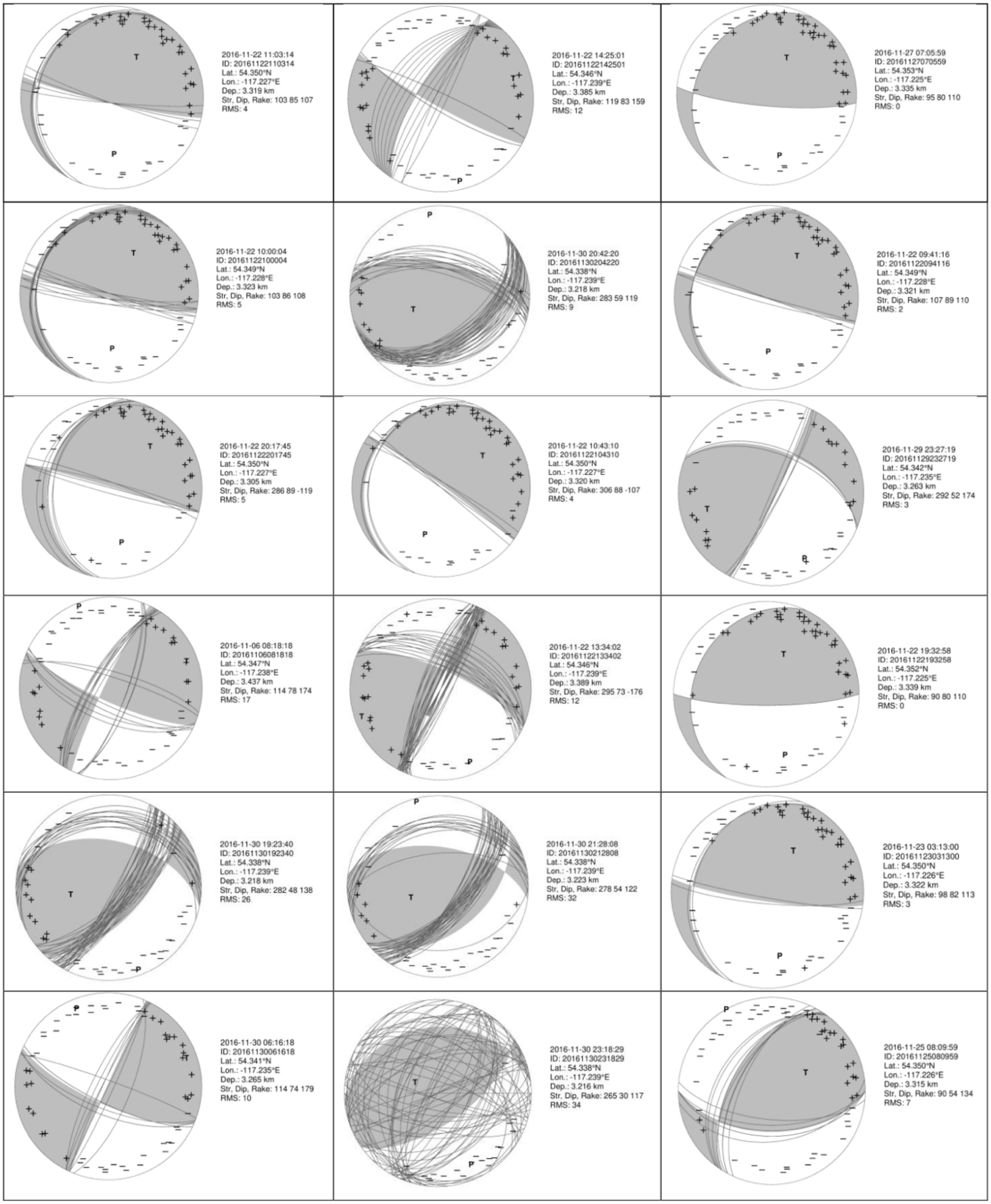

T
P
2016-11-22 11:03:14
ID: 20161122110314
Lat.: 54.350°N
Lon.: -117.227°E
Dep.: 3.319 km
Str, Dip, Rake: 103 85 107
RMS: 4
2016-11-22 14:25:01
ID: 20161122142501
Lat.: 54.346°N
Lon.: -117.239°E
Dep.: 3.385 km
Str, Dip, Rake: 119 83 159
RMS: 12
2016-11-27 07:05:59
ID: 20161127070559
Lat.: 54.353°N
Lon.: -117.225°E
Dep.: 3.335 km
Str, Dip, Rake: 95 80 110
RMS: 0
2016-11-22 10:00:04
ID: 20161122100004
Lat.: 54.349°N
Lon.: -117.228°E
Dep.: 3.323 km
Str, Dip, Rake: 103 86 108
RMS: 5
2016-11-30 20:42:20
ID: 20161130204220
Lat.: 54.338°N
Lon.: -117.239°E
Dep.: 3.218 km
Str, Dip, Rake: 283 59 119
RMS: 9
2016-11-22 09:41:16
ID: 20161122094116
Lat.: 54.349°N
Lon.: -117.228°E
Dep.: 3.321 km
Str, Dip, Rake: 107 89 110
RMS: 2
2016-11-22 20:17:45
ID: 20161122201745
Lat.: 54.350°N
Lon.: -117.227°E
Dep.: 3.305 km
Str, Dip, Rake: 286 89 -119
RMS: 5
2016-11-22 10:43:10
ID: 20161122104310
Lat.: 54.350°N
Lon.: -117.239°E
Dep.: 3.320 km
Str, Dip, Rake: 306 88 -107
RMS: 4
2016-11-29 23:27:19
ID: 20161129232719
Lat.: 54.342°N
Lon.: -117.235°E
Dep.: 3.263 km
Str, Dip, Rake: 292 52 174
RMS: 3
2016-11-06 08:18:18
ID: 20161106081818
Lat.: 54.347°N
Lon.: -117.238°E
Dep.: 3.437 km
Str, Dip, Rake: 114 78 174
RMS: 17
2016-11-22 13:34:02
ID: 20161122133402
Lat.: 54.346°N
Lon.: -117.239°E
Dep.: 3.389 km
Str, Dip, Rake: 295 73 -176
RMS: 12
2016-11-22 19:32:58
ID: 20161122193258
Lat.: 54.352°N
Lon.: -117.225°E
Dep.: 3.339 km
Str, Dip, Rake: 90 80 110
RMS: 0
2016-11-30 19:23:40
ID: 20161130192340
Lat.: 54.338°N
Lon.: -117.239°E
Dep.: 3.218 km
Str, Dip, Rake: 282 48 138
RMS: 26
2016-11-30 21:28:08
ID: 20161130212808
Lat.: 54.338°N
Lon.: -117.239°E
Dep.: 3.223 km
Str, Dip, Rake: 278 54 122
RMS: 32
2016-11-23 03:13:00
ID: 20161123031300
Lat.: 54.350°N
Lon.: -117.226°E
Dep.: 3.322 km
Str, Dip, Rake: 98 82 113
RMS: 3
2016-11-30 06:16:18
ID: 20161130061618
Lat.: 54.341°N
Lon.: -117.235°E
Dep.: 3.265 km
Str, Dip, Rake: 114 74 179
RMS: 10
2016-11-30 23:18:29
ID: 20161130231829
Lat.: 54.338°N
Lon.: -117.239°E
Dep.: 3.216 km
Str, Dip, Rake: 265 30 117
RMS: 34
2016-11-25 08:09:59
ID: 20161125080959
Lat.: 54.350°N
Lon.: -117.226°E
Dep.: 3.315 km
Str, Dip, Rake: 90 54 134
RMS: 7

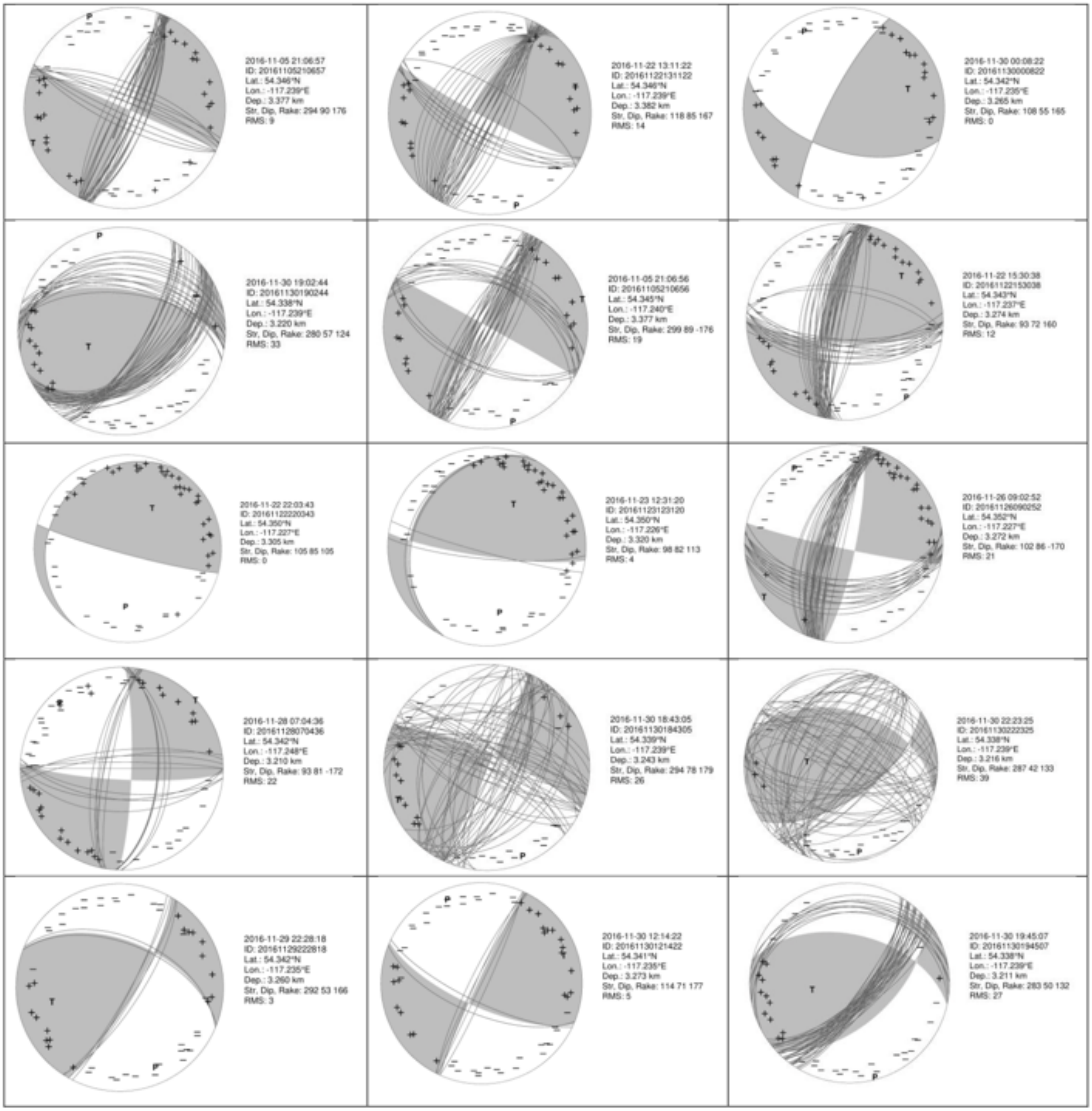
2016-11-05 21:06:57
ID: 20161105210657
Lat.: 54.346°N
Lon.: -117.239°E
Dep.: 3.377 km
Str, Dip, Rake: 294 90 176
RMS: 9
P
T
2016-11-22 13:11:22
ID: 20161122131122
Lat.: 54.346°N
Lon.: -117.239°E
Dep.: 3.382 km
Str, Dip, Rake: 118 85 167
RMS: 14
T
P
2016-11-30 00:08:22
ID: 20161130000822
Lat.: 54.342°N
Lon.: -117.235°E
Dep.: 3.265 km
Str, Dip, Rake: 108 55 165
RMS: 0
P
T
2016-11-30 19:02:44
ID: 20161130190244
Lat.: 54.338°N
Lon.: -117.239°E
Dep.: 3.220 km
Str, Dip, Rake: 280 57 124
RMS: 33
P
T
2016-11-05 21:06:56
ID: 20161105210656
Lat.: 54.345°N
Lon.: -117.240°E
Dep.: 3.377 km
Str, Dip, Rake: 299 89 -176
RMS: 19
T
P
2016-11-22 15:30:38
ID: 20161122153038
Lat.: 54.343°N
Lon.: -117.237°E
Dep.: 3.274 km
Str, Dip, Rake: 93 72 160
RMS: 12
T
P
2016-11-22 22:03:43
ID: 20161122220343
Lat.: 54.350°N
Lon.: -117.227°E
Dep.: 3.305 km
Str, Dip, Rake: 105 85 105
RMS: 0
T
P
2016-11-23 12:31:20
ID: 20161123123120
Lat.: 54.350°N
Lon.: -117.226°E
Dep.: 3.320 km
Str, Dip, Rake: 98 82 113
RMS: 4
T
P
2016-11-26 09:02:52
ID: 20161126090252
Lat.: 54.352°N
Lon.: -117.227°E
Dep.: 3.272 km
Str, Dip, Rake: 102 86 -170
RMS: 21
P
T
2016-11-28 07:04:36
ID: 20161128070436
Lat.: 54.342°N
Lon.: -117.248°E
Dep.: 3.210 km
Str, Dip, Rake: 93 81 -172
RMS: 22
T
2016-11-30 18:43:05
ID: 20161130184305
Lat.: 54.339°N
Lon.: -117.239°E
Dep.: 3.243 km
Str, Dip, Rake: 294 78 179
RMS: 26
P
2016-11-30 22:23:25
ID: 20161130222325
Lat.: 54.338°N
Lon.: -117.239°E
Dep.: 3.216 km
Str, Dip, Rake: 287 42 133
RMS: 39
T
P
2016-11-29 22:28:18
ID: 20161129222818
Lat.: 54.342°N
Lon.: -117.235°E
Dep.: 3.260 km
Str, Dip, Rake: 292 53 166
RMS: 3
T
P
2016-11-30 12:14:22
ID: 20161130121422
Lat.: 54.341°N
Lon.: -117.235°E
Dep.: 3.273 km
Str, Dip, Rake: 114 71 177
RMS: 5
P
2016-11-30 19:45:07
ID: 20161130194507
Lat.: 54.338°N
Lon.: -117.239°E
Dep.: 3.211 km
Str, Dip, Rake: 283 50 132
RMS: 27
T
P

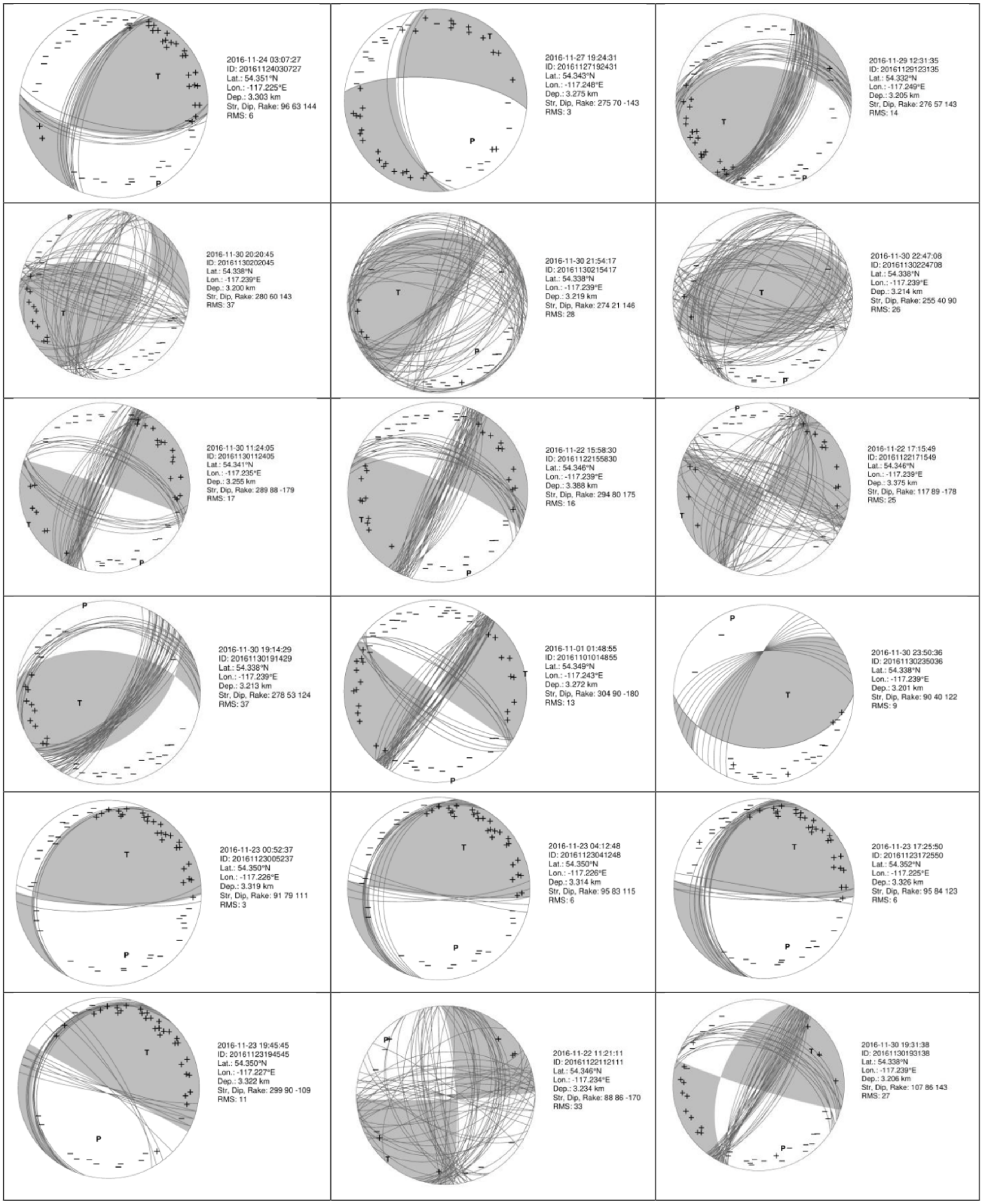
2016-11-24 03:07:27
ID: 20161124030727
Lat.: 54.351°N
Lon.: -117.225°E
Dep.: 3.303 km
Str, Dip, Rake: 96 63 144
RMS: 6
2016-11-27 19:24:31
ID: 20161127192431
Lat.: 54.343°N
Lon.: -117.248°E
Dep.: 3.275 km
Str, Dip, Rake: 275 70 -143
RMS: 3
2016-11-29 12:31:35
ID: 20161129123135
Lat.: 54.332°N
Lon.: -117.249°E
Dep.: 3.205 km
Str, Dip, Rake: 276 57 143
RMS: 14
2016-11-30 20:20:45
ID: 20161130202045
Lat.: 54.338°N
Lon.: -117.239°E
Dep.: 3.200 km
Str, Dip, Rake: 280 60 143
RMS: 37
2016-11-30 21:54:17
ID: 20161130215417
Lat.: 54.338°N
Lon.: -117.239°E
Dep.: 3.219 km
Str, Dip, Rake: 274 21 146
RMS: 28
2016-11-30 22:47:08
ID: 20161130224708
Lat.: 54.338°N
Lon.: -117.239°E
Dep.: 3.214 km
Str, Dip, Rake: 255 40 90
RMS: 26
2016-11-30 11:24:05
ID: 20161130112405
Lat.: 54.341°N
Lon.: -117.235°E
Dep.: 3.255 km
Str, Dip, Rake: 289 88 -179
RMS: 17
2016-11-22 15:58:30
ID: 20161122155830
Lat.: 54.346°N
Lon.: -117.239°E
Dep.: 3.388 km
Str, Dip, Rake: 294 80 175
RMS: 16
2016-11-22 17:15:49
ID: 20161122171549
Lat.: 54.346°N
Lon.: -117.239°E
Dep.: 3.375 km
Str, Dip, Rake: 117 89 -178
RMS: 25
2016-11-30 19:14:29
ID: 20161130191429
Lat.: 54.338°N
Lon.: -117.239°E
Dep.: 3.213 km
Str, Dip, Rake: 278 53 124
RMS: 37
2016-11-01 01:48:55
ID: 20161101014855
Lat.: 54.349°N
Lon.: -117.243°E
Dep.: 3.272 km
Str, Dip, Rake: 304 90 -180
RMS: 13
2016-11-30 23:50:36
ID: 20161130235036
Lat.: 54.338°N
Lon.: -117.239°E
Dep.: 3.201 km
Str, Dip, Rake: 90 40 122
RMS: 9
2016-11-23 00:52:37
ID: 20161123005237
Lat.: 54.350°N
Lon.: -117.226°E
Dep.: 3.319 km
Str, Dip, Rake: 91 79 111
RMS: 3
2016-11-23 04:12:48
ID: 20161123041248
Lat.: 54.350°N
Lon.: -117.226°E
Dep.: 3.314 km
Str, Dip, Rake: 95 83 115
RMS: 6
2016-11-23 17:25:50
ID: 20161123172550
Lat.: 54.352°N
Lon.: -117.225°E
Dep.: 3.326 km
Str, Dip, Rake: 95 84 123
RMS: 6
2016-11-23 19:45:45
ID: 20161123194545
Lat.: 54.350°N
Lon.: -117.227°E
Dep.: 3.322 km
Str, Dip, Rake: 299 90 -109
RMS: 11
2016-11-22 11:21:11
ID: 20161122112111
Lat.: 54.346°N
Lon.: -117.234°E
Dep.: 3.234 km
Str, Dip, Rake: 88 86 -170
RMS: 33
2016-11-30 19:31:38
ID: 20161130193138
Lat.: 54.338°N
Lon.: -117.239°E
Dep.: 3.206 km
Str, Dip, Rake: 107 86 143
RMS: 27

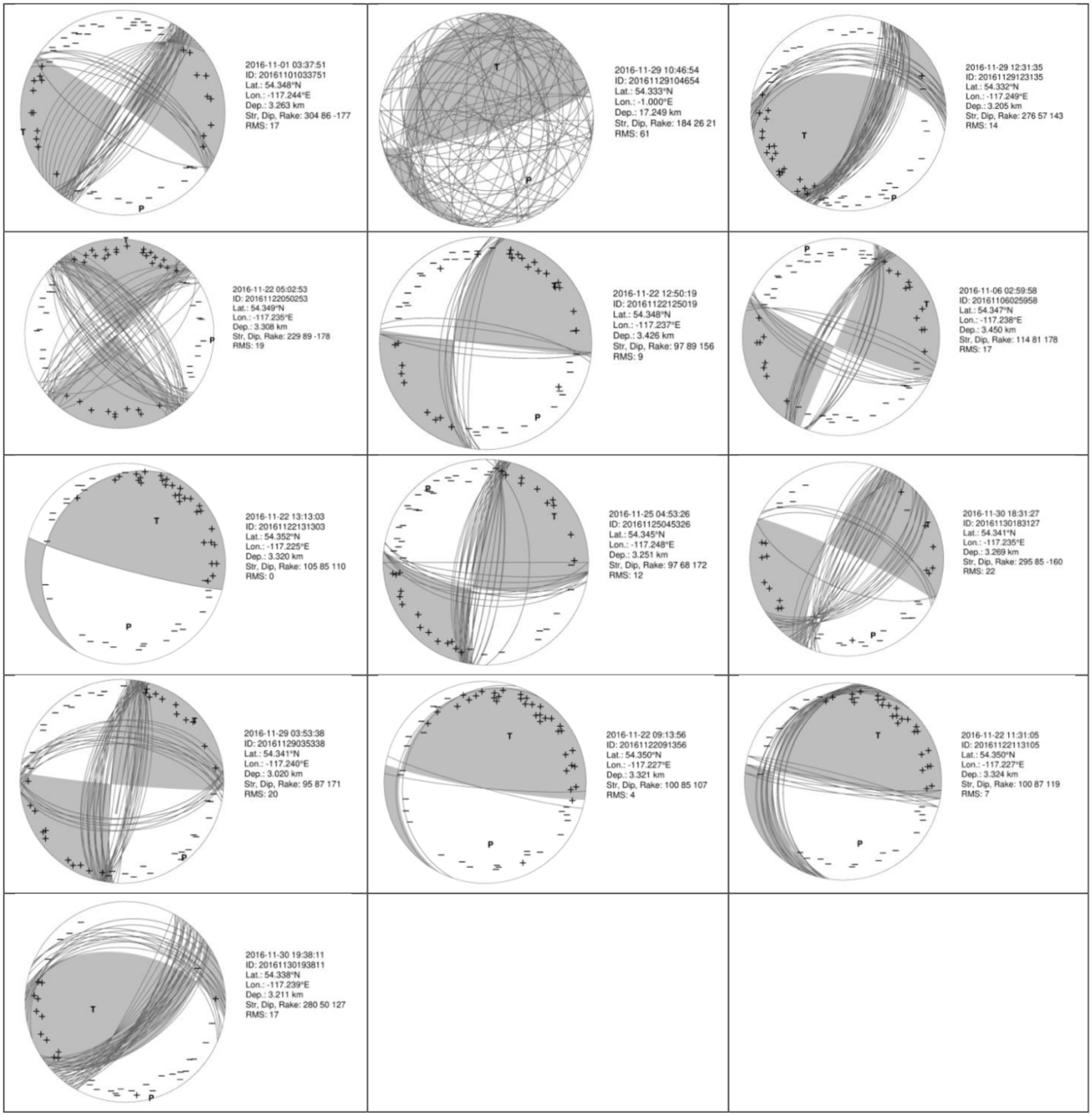
2016-11-01 03:37:51
ID: 20161101033751
Lat.: 54.348°N
Lon.: -117.244°E
Dep.: 3.263 km
Str, Dip, Rake: 304 86 -177
RMS: 17
2016-11-29 10:46:54
ID: 20161129104654
Lat.: 54.333°N
Lon.: -1.000°E
Dep.: 17.249 km
Str, Dip, Rake: 184 26 21
RMS: 61
2016-11-29 12:31:35
ID: 20161129123135
Lat.: 54.332°N
Lon.: -117.249°E
Dep.: 3.205 km
Str, Dip, Rake: 276 57 143
RMS: 14
2016-11-22 05:02:53
ID: 20161122050253
Lat.: 54.349°N
Lon.: -117.235°E
Dep.: 3.308 km
Str, Dip, Rake: 229 89 -178
RMS: 19
2016-11-22 12:50:19
ID: 20161122125019
Lat.: 54.348°N
Lon.: -117.237°E
Dep.: 3.426 km
Str, Dip, Rake: 97 89 156
RMS: 9
2016-11-06 02:59:58
ID: 20161106025958
Lat.: 54.347°N
Lon.: -117.238°E
Dep.: 3.450 km
Str, Dip, Rake: 114 81 178
RMS: 17
2016-11-22 13:13:03
ID: 20161122131303
Lat.: 54.352°N
Lon.: -117.225°E
Dep.: 3.320 km
Str, Dip, Rake: 105 85 110
RMS: 0
2016-11-25 04:53:26
ID: 20161125045326
Lat.: 54.345°N
Lon.: -117.248°E
Dep.: 3.251 km
Str, Dip, Rake: 97 68 172
RMS: 12
2016-11-30 18:31:27
ID: 20161130183127
Lat.: 54.341°N
Lon.: -117.235°E
Dep.: 3.269 km
Str, Dip, Rake: 295 85 -160
RMS: 22
2016-11-29 03:53:38
ID: 20161129035338
Lat.: 54.341°N
Lon.: -117.240°E
Dep.: 3.020 km
Str, Dip, Rake: 95 87 171
RMS: 20
2016-11-22 09:13:56
ID: 20161122091356
Lat.: 54.350°N
Lon.: -117.227°E
Dep.: 3.321 km
Str, Dip, Rake: 100 85 107
RMS: 4
2016-11-22 11:31:05
ID: 20161122113105
Lat.: 54.350°N
Lon.: -117.227°E
Dep.: 3.324 km
Str, Dip, Rake: 100 87 119
RMS: 7
2016-11-30 19:38:11
ID: 20161130193811
Lat.: 54.338°N
Lon.: -117.239°E
Dep.: 3.211 km
Str, Dip, Rake: 280 50 127
RMS: 17

Appendix D: Fault Plane Solutions for Comparison

Event ID	My FP1	H Zhang FP1	My FP2	H Zhang FP2
20161125212400.760	277/89/168	277/87/-177	7/78/1	7/88/-1
20161129101525.670	98/78/177	276/85/174	188/87/12	185/77/12
20161125053125.250	268/70/154	275/86/176	7/65/22	185/81/8
20161110030554.850	91/81/175	95/88/-178	181/85/9	185/89/0
20161129041247.910	90/59/162	97/83/173	189/74/32	7/89/0
20161110030629.460	92/68/162	274/86/176	188/73/23	184/85/4
20161128065337.920	90/89/164	272/81/171	180/74/1	181/84/5
20161111112409.170	91/83/177	94/87/177	181/87/7	4/89/0
20161111023345.600	275/88/180	274/85/175	4/90/2	184/89/0
20161110095529.320	94/87/170	94/88/178	184/80/3	4/89/0
20161127145251.080	272/68/167	272/79/169	6/77/22	182/89/0
20161122100431.400	105/88/109	114/82/-166	200/19/6	216/32/-57
20161121213944.800	94/73/162	273/88/-178	189/72/17	3/88/-1
20161115132811.100	95/75/168	273/89/179	188/78/15	183/89/0
20161122181824.960	102/85/106	113/87/-174	208/16/17	207/28/-61
20161128153527.280	90/63/160	273/89/179	189/72/28	183/88/1
20161111150658.250	271/85/179	273/89/179	1/89/5	183/86/3
20161122131844.000	105/89/110	98/80/-163	197/20/2	202/37/-53
20161128124723.150	90/65/157	274/85/175	190/69/26	184/87/2
20161110142852.360	95/80/165	273/86/176	187/75/10	183/89/0
20161122112106.380	105/88/109	111/87/-174	200/19/6	207/22/-67
20161108042434.850	95/78/175	272/76/166	186/85/12	182/87/2
20161127071613.740	280/90/169	277/84/174	9/78/0	187/89/0
20161122115553.200	102/88/110	109/82/-163	197/20/5	214/28/-62
20161110055923.720	275/82/-179	275/85/-175	184/89/-8	5/89/0
20161109133343.450	268/38/165	273/87/-177	9/80/52	3/89/0
20161111124536.460	275/88/172	271/79/169	5/82/2	180/83/6
20161127140748.080	93/75/161	273/88/178	188/71/15	183/88/1
20161122095728.410	107/88/109	108/77/-155	202/19/6	219/31/-60
20161108085355.710	95/75/175	272/80/170	186/85/15	182/87/2
20161126224707.880	93/80/110	103/78/-164	208/22/27	204/46/-44
20161122122845.350	102/88/110	114/81/-160	197/20/5	222/25/-66
20161108131656.020	327/15/-123	96/78/-168	180/77/-81	186/89/0
20161109080900.140	94/83/-172	97/84/174	3/82/-7	6/87/2
20161123233803.400	95/80/117	104/79/-165	203/28/21	205/44/-45
20161122172604.520	102/88/108	115/86/-172	198/18/6	212/23/-66
20161123053630.990	95/80/110	282/89/179	210/22/27	192/48/41
20161111075108.920	263/61/148	91/88/178	9/62/33	1/88/1
20161122170222.360	93/80/110	105/78/-160	208/22/27	211/37/-54
20161123072346.210	95/83/110	107/84/-172	203/21/19	202/47/-42
20161127022900.340	280/80/157	277/81/171	14/67/10	187/87/2
20161107124958.150	95/80/175	273/83/173	185/85/10	183/88/1

20161111204340.840	95/73/176	273/82/-172	186/86/17	3/89/0
20161111031632.540	270/79/167	273/80/-170	2/77/11	3/89/0
20161129164710.560	95/75/168	273/89/179	188/78/15	183/89/0
20161107134506.900	95/78/175	272/85/175	186/85/12	182/88/1
20161122105125.690	103/88/110	304/89/179	198/20/5	214/39/50
20161123133046.610	95/80/110	105/81/-167	210/22/27	205/42/-48
20161129055749.920	95/89/151	273/84/174	185/61/1	183/81/8
20161110053424.890	99/89/166	276/87/177	189/76/1	186/84/5
20161111135509.020	262/57/160	90/89/-179	3/73/34	180/87/-2
20161129040404.340	94/72/163	273/87/177	189/73/18	183/88/1
20161107160909.690	95/78/175	272/85/175	186/85/12	182/87/2
20161109022000.730	95/72/175	272/79/169	186/85/18	182/88/1
20161123115530.520	95/80/112	102/78/-163	208/24/25	204/44/-46
20161124204321.760	90/80/110	104/79/-164	205/22/27	205/43/-47
20161112192015.560	268/85/-169	272/82/172	177/79/-5	182/89/0
20161110070628.420	261/61/145	273/89/-179	9/59/34	3/87/-2
20161129013555.900	95/83/171	274/86/176	186/81/7	183/87/2
20161129023235.210	94/79/-175	95/89/179	3/85/-11	5/89/0
20161123123618.040	93/57/165	95/89/179	191/77/33	5/89/0
20161114022425.140	95/75/177	273/87/177	185/87/15	183/89/0
20161124063732.060	99/69/153	285/87/177	199/64/23	194/85/4
20161123190445.600	270/85/145	95/88/178	3/55/6	5/89/0
20161123054115.530	97/80/112	103/81/-166	210/24/25	203/42/-48
20161129002023.160	95/84/173	273/85/175	185/83/6	183/87/2
20161126042630.020	98/86/-177	272/85/175	7/87/-4	182/89/0
20161124173142.800	95/84/122	103/78/-164	194/32/11	204/46/-44
20161111113517.030	270/85/135	274/88/178	4/45/7	184/88/1
20161115133335.740	266/78/140	273/87/177	5/51/15	183/88/1
20161123054748.150	104/88/109	120/87/-176	199/19/6	213/38/-51
20161122082716.550	98/83/110	113/81/-167	206/21/19	213/42/-47
20161127053859.540	92/82/117	105/86/-173	197/28/17	200/36/-53
20161105190554.800	296/80/-176	296/84/174	205/86/-10	205/87/2
20161128103144.820	91/58/162	274/89/179	190/74/33	184/89/0
20161129062934.130	95/86/171	277/88/178	185/81/4	187/88/1
20161125033151.580	110/70/163	118/84/-173	205/74/20	211/64/-25
20161103103924.780	116/82/-177	292/85/175	25/87/-8	202/89/0
20161127174203.560	100/83/-176	272/83/173	9/86/-7	182/88/1
20161122054155.950	103/85/110	290/89/179	206/20/14	200/39/50
20161109225452.840	264/67/154	273/85/-175	4/66/25	3/87/-2
20161110045219.450	271/86/170	272/84/-174	1/80/4	2/89/0
20161105142204.470	294/83/177	296/87/177	24/87/7	206/88/1
20161107190210.440	90/79/157	271/83/173	184/67/11	181/86/3
20161109043008.840	277/82/173	273/80/170	7/83/8	183/88/1
20161124041925.220	95/80/122	108/83/-171	200/33/18	204/48/-41
20161125103647.080	89/58/135	289/86/176	206/53/41	199/85/4
20161125220631.120	105/88/127	107/83/-171	197/37/3	202/53/-36

20161103092313.360	290/76/160	293/89/179	25/70/14	203/89/0
20161120174830.760	265/78/-170	91/89/179	172/80/-12	1/89/0
20161122025658.740	103/85/110	291/88/177	206/20/14	199/39/50
20161125022842.720	93/80/110	286/87/177	208/22/27	194/44/45
20161129024743.160	274/90/-157	274/85/175	183/67/0	183/87/2
20161105170516.800	293/75/173	297/83/173	24/83/15	206/84/5
20161128152950.020	87/83/175	272/88/178	177/85/7	182/89/0
20161128232614.640	93/85/163	272/76/166	184/73/5	181/88/1
20161129043634.690	273/89/-148	273/84/174	182/58/-1	182/74/15
20161110090639.470	277/90/-170	276/89/179	187/80/0	186/86/3
20161126165253.470	97/85/-159	274/87/177	5/69/-5	184/89/0
20161128090833.480	88/63/155	273/88/178	189/67/29	183/88/1
20161103090235.220	114/58/167	293/88/-178	210/79/32	23/89/0
20161111114204.210	92/75/175	271/89/-179	183/85/15	1/88/-1
20161108213326.040	267/69/178	272/88/178	357/88/21	182/87/2
20161110031035.200	275/90/170	273/87/177	4/80/0	183/89/0
20161128100152.720	102/60/180	275/87/177	11/90/-29	185/88/1
20161122120956.630	105/89/110	112/86/-168	197/20/2	213/18/-71
20161122125832.460	283/89/-111	109/87/-175	190/21/-2	202/32/-57
20161123142910.200	105/88/110	294/89/177	200/20/5	202/25/64
20161103091323.390	111/84/172	292/86/176	201/82/6	202/89/0
20161122200055.560	95/80/110	103/78/-161	210/22/27	208/38/-53
20161128223548.560	96/85/172	273/86/176	186/82/5	183/87/2
20161105181519.980	115/85/179	296/86/176	205/89/5	206/88/1
20161110234432.560	94/72/178	273/82/172	184/88/18	183/89/0
20161128013854.830	91/64/160	273/89/179	190/72/27	183/88/1
20161105213639.960	295/84/-179	294/81/171	204/89/-6	204/85/4
20161129162829.850	93/67/166	277/89/-179	188/77/23	7/89/0
20161106004251.060	111/89/-168	295/86/176	20/78/-1	205/89/0
20161110143528.270	266/74/161	272/88/-178	1/71/16	2/87/-2
20161121232019.320	264/60/150	274/89/-179	10/64/33	4/89/0
20161127105310.170	267/88/168	274/83/173	357/78/2	183/87/2
20161129040204.270	272/89/161	273/87/177	2/71/1	183/89/0
20161103093736.270	291/64/157	293/87/177	31/69/27	203/89/0
20161103100858.620	290/74/164	292/85/175	24/74/16	202/88/1
20161105165232.000	295/80/-177	295/83/173	204/87/-10	204/86/3
20161110093430.320	96/60/180	93/85/175	5/90/-30	3/88/1
20161122135417.350	296/87/-175	296/85/175	205/85/-3	205/87/2
20161129090645.280	95/75/167	272/84/174	188/77/15	181/81/8
20161103095905.070	113/78/174	292/85/175	204/84/12	202/88/1
20161105174947.600	296/82/-177	296/80/170	205/87/-8	205/82/7
20161112171011.400	262/67/162	92/89/179	359/73/24	2/89/0
20161119043353.720	261/55/145	272/88/178	12/61/40	182/89/0
20161122092550.070	100/82/109	109/81/-164	212/20/23	212/33/-57
20161123080243.390	108/88/110	285/87/176	203/20/5	192/39/50
20161103113425.270	286/73/159	293/86/176	22/69/18	203/89/0

20161106023359.070	113/62/163	295/82/172	211/75/29	204/85/4
20161107112627.310	95/71/171	271/84/174	187/81/19	181/87/2
20161105145728.010	289/89/168	294/84/174	19/78/1	204/84/5
20161122110303.780	101/83/110	113/79/-163	209/21/19	216/39/-51
20161125002430.640	173/7/-25	121/85/-172	173/7/-25	217/33/-56
20161107110551.530	271/89/-169	272/85/175	180/79/-1	182/85/4
20161122213052.760	94/87/128	285/87/176	187/38/4	192/43/46
20161106044609.820	115/80/178	296/83/173	205/88/10	205/86/3
20161110103906.120	274/76/180	274/85/175	4/90/13	184/89/0
20161128151047.400	89/72/155	273/88/178	187/66/19	183/86/3
20161105161550.920	293/88/168	296/86/176	23/78/2	206/89/0
20161111091023.760	269/83/172	93/88/178	359/82/7	3/88/1
20161113060754.000	92/82/167	272/84/-174	183/77/8	2/89/0
20161122043948.240	291/82/168	294/85/175	22/78/8	204/88/1
20161127020128.430	98/85/180	276/80/170	8/90/-4	186/85/4
20161128004222.370	268/85/175	272/79/169	358/85/5	182/87/2
20161128045908.970	92/62/163	95/88/178	190/75/29	5/89/0
20161103084525.280	289/80/176	292/86/-176	19/86/10	22/89/0
20161123002249.700	95/80/110	102/78/-164	210/22/27	203/49/-42
20161123023135.080	99/65/156	104/88/-178	199/68/27	194/85/-4
20161127042324.690	278/85/148	277/85/-175	11/58/5	7/89/0
20161128101159.780	92/81/158	276/86/176	185/68/9	186/86/3
20161110094624.840	95/81/-176	272/84/-174	4/86/-9	2/89/0
20161110222605.960	272/89/178	273/85/-175	2/88/1	3/89/0
20161121232043.560	95/80/110	109/83/-171	210/22/27	205/45/-44
20161105195356.440	119/81/-173	296/81/171	27/83/-9	206/85/4
20161108172656.100	94/90/-170	273/87/177	3/80/0	183/89/0
20161122041646.330	299/80/-172	294/79/169	207/82/-10	203/84/5
20161123130253.500	110/87/108	117/84/-170	209/18/9	215/35/-54
20161101180516.600	285/81/153	112/84/173	19/63/10	21/78/11
20161108054435.090	272/88/-174	274/88/-178	181/84/-2	4/85/-4
20161127213349.060	291/55/-137	272/77/167	172/56/-43	182/88/1

Appendix E: Kagan Value Solutions

Event ID	Kagan Value	Event ID	Kagan Value
20161125212400.760	10.20	20161110070628.420	44.28
20161129101525.670	10.44	20161129013555.900	8.17
20161125053125.250	44.90	20161129023235.210	11.77
20161110030554.850	10.80	20161123123618.040	35.68
20161129041247.910	35.95	20161114022425.140	15.19
20161110030629.460	22.15	20161124063732.060	27.77
20161128065337.920	10.74	20161123190445.600	34.67
20161111112409.170	8.64	20161123054115.530	69.24
20161111023345.600	2.24	20161129002023.160	5.88
20161110095529.320	11.40	20161126042630.020	7.59
20161127145251.080	25.98	20161124173142.800	64.49
20161122100431.400	78.70	20161111113517.030	47.64
20161121213944.800	25.73	20161115133335.740	43.69
20161115132811.100	18.79	20161123054748.150	71.96
20161122181824.960	77.85	20161122082716.550	74.74
20161128153527.280	30.97	20161127053859.540	72.94
20161111150658.250	9.60	20161105190554.800	12.04
20161122131844.000	61.65	20161128103144.820	35.83
20161128124723.150	29.50	20161129062934.130	7.95
20161110142852.360	17.33	20161125033151.580	48.45
20161122112106.380	79.64	20161103103924.780	9.48
20161108042434.850	10.69	20161127174203.560	11.06
20161127071613.740	13.15	20161122054155.950	45.37
20161122115553.200	83.13	20161109225452.840	33.91
20161110055923.720	8.31	20161110045219.450	9.94
20161109133343.450	52.47	20161105142204.470	9.66
20161111124536.460	17.68	20161107190210.440	20.54
20161127140748.080	21.97	20161109043008.840	13.21
20161122095728.410	82.48	20161124041925.220	63.73
20161108085355.710	13.48	20161125103647.080	47.07
20161126224707.880	71.29	20161125220631.120	45.48
20161122122845.350	94.63	20161103092313.360	25.09
20161108131656.020	81.19	20161120174830.760	18.11
20161109080900.140	10.48	20161122025658.740	46.19
20161123233803.400	69.29	20161125022842.720	37.71
20161122172604.520	85.36	20161129024743.160	20.10
20161123053630.990	40.04	20161105170516.800	23.91
20161111075108.920	40.12	20161128152950.020	9.67
20161122170222.360	84.73	20161128232614.640	15.68
20161123072346.210	65.04	20161129043634.690	22.59
20161127022900.340	28.92	20161110090639.470	6.84
20161107124958.150	9.58	20161126165253.470	22.61
20161111204340.840	17.89	20161128090833.480	34.32

20161111031632.540	16.38	20161103090235.220	34.24
20161129164710.560	18.79	20161111114204.210	15.72
20161107134506.900	11.86	20161108213326.040	24.01
20161122105125.690	36.87	20161110031035.200	11.05
20161123133046.610	73.15	20161128100152.720	28.59
20161129055749.920	21.49	20161122120956.630	88.28
20161110053424.890	9.65	20161122125832.460	66.79
20161111135509.020	37.40	20161123142910.200	57.36
20161129040404.340	22.67	20161103091323.390	9.32
20161107160909.690	10.69	20161122200055.560	79.62
20161109022000.730	17.48	20161112192015.560	6.42
20161123115530.520	70.22	20161128223548.560	44.28
20161112192015.560	76.51	20161105181519.980	4.27
20161110234432.560	18.03	20161107110551.530	7.89
20161128013854.830	30.20	20161122213052.760	38.64
20161105213639.960	10.77	20161106044609.820	7.28
20161129162829.850	26.81	20161110103906.120	13.04
20161106004251.060	13.93	20161128151047.400	25.26
20161110143528.270	24.20	20161105161550.920	13.53
20161121232019.320	40.47	20161111091023.760	9.60
20161127105310.170	16.75	20161113060754.000	16.09
20161129040204.270	20.06	20161122043948.240	16.84
20161103093736.270	34.50	20161127020128.430	5.38
20161103100858.620	24.62	20161128004222.370	11.40
20161105165232.000	13.04	20161128045908.970	32.87
20161110093430.320	31.16	20161103084525.280	10.98
20161122135417.350	5.38	20161123002249.700	68.21
20161129090645.280	9.76	20161123023135.080	34.56
20161103095905.070	11.74	20161127042324.690	31.46
20161105174947.600	15.81	20161128101159.780	19.06
20161112171011.400	29.32	20161110094624.840	9.77
20161119043353.720	48.59	20161110222605.960	1.75
20161122092550.070	80.87	20161121232043.560	70.20
20161123080243.390	57.89	20161105195356.440	13.04
20161103113425.270	28.48	20161108172656.100	11.00
20161106023359.070	26.66	20161122041646.330	16.11
20161107112627.310	18.41	20161123130253.500	70.30
20161105145728.010	19.69	20161101180516.600	15.12
20161122110303.780	77.98	20161108054435.090	12.87
20161125002430.640	78.12	20161127213349.060	52.22

Appendix F: Final Catalog

Event ID	Latitude	Longitude	Depth	M	RMS	FP1	FP2
20161125212400.760	54.347937	-117.245207	3.285	3.21	14	277/89/168	7/78/1
20161129101525.670	54.337606	-117.248543	3.265	3.2	11	98/78/177	188/87/12
20161125053125.250	54.344124	-117.248193	3.27	3.15	09	268/70/154	7/65/22
20161110030554.850	54.33776	-117.243392	3.268	2.82	16	91/81/175	181/85/9
20161129041247.910	54.34056	-117.248429	3.204	2.69	04	90/59/162	189/74/32
20161110030629.460	54.33772	-117.243368	3.235	2.51	08	92/68/162	188/73/23
20161128065337.920	54.343429	-117.248145	3.269	2.5	12	90/89/164	180/74/1
20161111112409.170	54.338261	-117.243343	3.241	2.44	13	91/83/177	181/87/7
20161111023345.600	54.33741	-117.243416	3.248	2.23	17	275/88/180	4/90/2
20161110095529.320	54.33835	-117.243408	3.243	2.02	09	94/87/170	184/80/3
20161127145251.080	54.346004	-117.24541	3.302	1.88	16	272/68/167	6/77/22
20161122100431.400	54.349463	-117.227539	3.327	1.87	04	105/88/109	200/19/6
20161121213944.800	54.338713	-117.243278	3.229	1.75	07	94/73/162	189/72/17
20161115132811.100	54.338643	-117.243278	3.224	1.69	04	95/75/168	188/78/15
20161122181824.960	54.349809	-117.227303	3.335	1.67	04	102/85/106	208/16/17
20161128153527.280	54.341349	-117.248437	3.215	1.6	03	90/63/160	189/72/28
20161111150658.250	54.337252	-117.243441	3.233	1.45	15	271/85/179	1/89/5
20161122131844.000	54.349666	-117.227507	3.326	1.43	05	105/89/110	197/20/2
20161128124723.150	54.341345	-117.248372	3.236	1.38	01	90/65/157	190/69/26
20161110142852.360	54.338428	-117.243311	3.229	1.36	00	95/80/165	187/75/10
20161122112106.380	54.349748	-117.227311	3.319	1.35	04	105/88/109	200/19/6
20161108042434.850	54.338098	-117.24856	3.256	1.28	01	95/78/175	186/85/12
20161127071613.740	54.345793	-117.245296	3.277	1.24	14	280/90/169	9/78/0
20161122115553.200	54.349727	-117.227417	3.328	1.22	03	102/88/110	197/20/5
20161110055923.720	54.337651	-117.2434	3.268	1.21	08	275/82/-179	184/89/-8
20161109133343.450	54.338623	-117.248503	3.258	1.13	22	268/38/165	9/80/52
20161111124536.460	54.338546	-117.248429	3.247	1.08	11	275/88/172	5/82/2
20161122094208.150	54.349296	-117.227572	3.32	1.05	02	107/89/110	199/20/2
20161127140748.080	54.338839	-117.243278	3.233	1	21	93/75/161	188/71/15
20161122095728.410	54.349231	-117.227629	3.322	0.99	03	107/88/109	202/19/6
20161130113122.010	54.352755	-117.225244	3.347	0.98	00	95/80/115	205/26/22
20161108085355.710	54.337756	-117.248576	3.262	0.93	00	95/75/175	186/85/15
20161123082307.680	54.349662	-117.22736	3.319	0.89	00	105/85/110	208/20/14
20161126224707.880	54.352547	-117.225203	3.327	0.89	02	93/80/110	208/22/27
20161122122845.350	54.349931	-117.227336	3.332	0.87	03	102/88/110	197/20/5
20161108131656.020	54.337581	-117.248543	3.237	0.86	03	327/15/-123	180/77/-81
20161109080900.140	54.337097	-117.248494	3.24	0.85	14	94/83/-172	3/82/-7
20161130174836.600	54.332841	-117.249007	3.206	0.83	03	270/45/143	28/64/51
20161123233803.400	54.352266	-117.225399	3.335	0.82	03	95/80/117	203/28/21
20161122172604.520	54.349801	-117.227547	3.33	0.8	04	102/88/108	198/18/6
20161123053630.990	54.352144	-117.225431	3.332	0.79	00	95/80/110	210/22/27
20161111075108.920	54.337207	-117.243433	3.223	0.78	06	263/61/148	9/62/33
20161114225250.620	54.334648	-117.249251	3.276	0.77	09	91/86/-162	359/72/-4
20161122170222.360	54.352193	-117.225472	3.338	0.76	02	93/80/110	208/22/27
20161123072346.210	54.35002	-117.225887	3.318	0.76	05	95/83/110	203/21/19
20161127022900.340	54.345732	-117.245288	3.278	0.74	09	280/80/157	14/67/10
20161107124958.150	54.338159	-117.248535	3.26	0.71	00	95/80/175	185/85/10
20161111204340.840	54.335563	-117.248869	3.273	0.71	04	95/73/176	186/86/17
20161122141605.480	54.350094	-117.227344	3.329	0.68	04	103/90/111	193/21/0
20161111031632.540	54.335905	-117.248739	3.273	0.67	16	270/79/167	2/77/11
20161124153705.230	54.349829	-117.227165	3.314	0.65	02	108/85/105	216/15/18
20161129164710.560	54.338875	-117.243254	3.231	0.63	04	95/75/168	188/78/15
20161107134506.900	54.338009	-117.248543	3.259	0.62	01	95/78/175	186/85/12
20161122210507.760	54.34989	-117.227214	3.314	0.62	04	104/88/109	199/19/6
20161122095100.880	54.349377	-117.227547	3.321	0.6	02	107/89/110	199/20/2
20161122105125.690	54.349792	-117.227246	3.316	0.59	03	103/88/110	198/20/5
20161122162235.440	54.351876	-117.225423	3.325	0.59	03	98/83/110	206/21/19
20161123133046.610	54.35249	-117.225326	3.342	0.59	00	95/80/110	210/22/27

20161123181714.420	54.350187	-117.227246	3.327	0.58	02	292/88/-110	196/20/-5
20161129055749.920	54.340568	-117.248397	3.257	0.58	05	95/89/151	185/61/1
20161110053424.890	54.338261	-117.243327	3.237	0.57	07	99/89/166	189/76/1
20161111135509.020	54.338151	-117.243343	3.21	0.57	05	262/57/160	3/73/34
20161123231319.160	54.349854	-117.227091	3.322	0.56	04	104/88/109	199/19/6
20161129040404.340	54.341463	-117.248307	3.192	0.56	06	94/72/163	189/73/18
20161107160909.690	54.337903	-117.248568	3.266	0.53	01	95/78/175	186/85/12
20161107205908.760	54.337907	-117.248527	3.29	0.53	13	274/70/-169	180/79/-20
20161128150212.190	54.341044	-117.248348	3.252	0.53	05	93/69/164	188/75/21
20161109022000.730	54.33739	-117.248608	3.266	0.52	01	95/72/175	186/85/18
20161123115530.520	54.352254	-117.225407	3.335	0.52	01	95/80/112	208/24/25
20161124204321.760	54.352563	-117.225269	3.332	0.52	00	90/80/110	205/22/27
20161112192015.560	54.335372	-117.248901	3.279	0.51	13	268/85/-169	177/79/-5
20161128080529.680	54.341516	-117.248283	3.244	0.5	06	94/70/164	189/74/20
20161110070628.420	54.337313	-117.243416	3.223	0.49	05	261/61/145	9/59/34
20161129013555.900	54.340869	-117.248356	3.251	0.49	07	95/83/171	186/81/7
20161129023235.210	54.341496	-117.248324	3.23	0.49	21	94/79/-175	3/85/-11
20161123123618.040	54.341475	-117.248348	3.248	0.48	09	93/57/165	191/77/33
20161114022425.140	54.338228	-117.248535	3.227	0.47	12	95/75/177	185/87/15
20161122100459.730	54.349854	-117.227295	3.319	0.47	04	105/88/109	200/19/6
20161124063732.060	54.352352	-117.226823	3.276	0.47	20	99/69/153	199/64/23
20161124153728.340	54.341374	-117.248291	3.248	0.45	00	270/85/145	3/55/6
20161123190445.600	54.35247	-117.225448	3.348	0.44	03	97/80/112	210/24/25
20161123054115.530	54.340951	-117.24834	3.248	0.44	04	95/84/173	185/83/6
20161129002023.160	54.338334	-117.238957	3.205	0.44	18	282/52/128	50/51/51
20161130195902.660	54.345886	-117.24528	3.25	0.43	16	98/86/-177	7/87/-4
20161126042630.020	54.352482	-117.225228	3.328	0.42	06	95/84/122	194/32/11
20161124173142.800	54.338566	-117.243286	3.209	0.39	00	270/85/135	4/45/7
20161111113517.030	54.338741	-117.243319	3.247	0.39	02	266/78/140	5/51/15
20161115133335.740	54.349817	-117.227441	3.325	0.39	03	102/88/110	197/20/5
20161122114139.910	54.349992	-117.227197	3.326	0.39	04	104/88/109	199/19/6
20161123054748.150	54.341443	-117.234717	3.261	0.39	06	282/60/152	26/66/33
20161130004322.510	54.351933	-117.225431	3.323	0.37	04	98/83/110	206/21/19
20161122082716.550	54.352751	-117.225212	3.343	0.37	05	92/82/117	197/28/17
20161127053859.540	54.345699	-117.239372	3.41	0.36	12	296/80/-176	205/86/-10
20161105190554.800	54.341471	-117.248307	3.212	0.36	08	91/58/162	190/74/33
20161128103144.820	54.341614	-117.248315	3.242	0.36	04	95/86/171	185/81/4
20161129062934.130	54.350094	-117.227222	3.324	0.34	04	105/88/109	200/19/6
20161122124507.380	54.350073	-117.225993	3.329	0.34	04	99/83/113	205/23/17
20161122234914.200	54.338436	-117.243294	3.237	0.33	12	275/78/178	5/88/12
20161110095951.670	54.349972	-117.227368	3.328	0.33	16	286/84/-113	182/23/-15
20161123162734.300	54.352332	-117.225269	3.319	0.33	35	97/80/115	207/26/22
20161124114121.020	54.350688	-117.225578	3.31	0.33	16	110/70/163	205/74/20
20161125033151.580	54.347583	-117.24104	3.327	0.32	14	116/82/-177	25/87/-8
20161103103924.780	54.345789	-117.245296	3.25	0.32	11	100/83/-176	9/86/-7
20161127174203.560	54.351835	-117.225496	3.324	0.31	02	103/85/110	206/20/14
20161122054155.950	54.335767	-117.248804	3.271	0.3	05	264/67/154	4/66/25
20161109225452.840	54.335628	-117.248836	3.283	0.3	15	271/86/170	1/80/4
20161110045219.450	54.349422	-117.227572	3.323	0.3	05	103/86/108	205/18/12
20161122100004.490	54.338216	-117.239079	3.218	0.3	09	283/59/119	55/41/51
20161130204220.240	54.349227	-117.227629	3.321	0.28	02	107/89/110	199/20/2
20161122094116.900	54.34954	-117.227173	3.305	0.28	05	286/89/-119	194/29/-2
20161122201745.100	54.345406	-117.239551	3.376	0.27	12	294/83/177	24/87/7
20161105142204.470	54.33807	-117.248568	3.276	0.27	15	90/79/157	184/67/11
20161107190210.440	54.337288	-117.248617	3.268	0.27	14	277/82/173	7/83/8
20161109043008.840	54.349792	-117.22736	3.32	0.27	04	306/88/-107	209/17/-6
20161122104310.510	54.352466	-117.225326	3.327	0.27	04	95/80/122	200/33/18
20161124041925.220	54.352401	-117.226864	3.269	0.27	13	89/58/135	206/53/41
20161125103647.080	54.352368	-117.225309	3.326	0.27	04	105/88/127	197/37/3
20161125220631.120	54.341504	-117.234725	3.263	0.27	03	292/52/174	25/85/38
20161129232719.840	54.347485	-117.241203	3.332	0.26	20	290/76/160	25/70/14
20161103092313.360	54.346871	-117.238354	3.437	0.26	17	114/78/174	205/84/12
20161106081818.870	54.345549	-117.239437	3.389	0.26	12	295/73/-176	203/86/-17

20161122133402.620	54.338611	-117.24327	3.212	0.25	09	265/78/-170	172/80/-12
20161120174830.760	54.351876	-117.225456	3.324	0.25	02	103/85/110	206/20/14
20161122025658.740	54.352177	-117.22548	3.339	0.25	00	90/80/110	205/22/27
20161122193258.200	54.352661	-117.225236	3.332	0.25	02	93/80/110	208/22/27
20161125022842.720	54.340743	-117.248372	3.254	0.25	11	274/90/-157	183/67/0
20161129024743.160	54.345634	-117.239396	3.342	0.24	31	293/75/173	24/83/15
20161105170516.800	54.341471	-117.24834	3.195	0.24	13	87/83/175	177/85/7
20161128152950.020	54.337602	-117.248478	3.241	0.24	13	93/85/163	184/73/5
20161128232614.640	54.340405	-117.248397	3.258	0.24	08	273/89/-148	182/58/-1
20161129043634.690	54.33842	-117.238875	3.218	0.24	26	282/48/138	43/60/50
20161130192340.520	54.338269	-117.239006	3.223	0.24	32	278/54/122	51/46/53
20161130212808.740	54.33726	-117.243416	3.23	0.23	17	277/90/-170	187/80/0
20161110090639.470	54.350033	-117.225895	3.322	0.23	03	98/82/113	206/24/19
20161123031300.690	54.346611	-117.245215	3.284	0.23	09	97/85/-159	5/69/-5
20161126165253.470	54.341439	-117.248307	3.223	0.23	03	88/63/155	189/67/29
20161128090833.480	54.341423	-117.234709	3.265	0.23	10	114/74/179	204/89/16
20161130061618.220	54.338078	-117.239054	3.216	0.23	34	265/30/117	265/30/117
20161130231829.880	54.347428	-117.241235	3.33	0.22	02	114/58/167	210/79/32
20161103090235.220	54.338481	-117.243302	3.205	0.22	13	92/75/175	183/85/15
20161111114204.210	54.349805	-117.225659	3.315	0.22	07	90/54/134	211/54/46
20161125080959.220	54.337496	-117.248633	3.273	0.21	15	267/69/178	357/88/21
20161108213326.040	54.34974	-117.227271	3.319	0.21	04	103/85/107	208/17/16
20161122110314.520	54.345658	-117.239388	3.385	0.21	12	119/83/159	211/69/7
20161122142501.650	54.336894	-117.248665	3.258	0.2	17	275/90/170	4/80/0
20161110031035.200	54.352828	-117.225203	3.335	0.2	00	95/80/110	210/22/27
20161127070559.240	54.34126	-117.248348	3.252	0.2	00	102/60/180	11/90/-29
20161128100152.720	54.345638	-117.239388	3.377	0.19	09	294/90/176	23/86/0
20161105210657.920	54.349923	-117.227393	3.331	0.19	05	105/89/110	197/20/2
20161122120956.630	54.349894	-117.227498	3.332	0.19	05	283/89/-111	190/21/-2
20161122125832.460	54.34565	-117.239347	3.382	0.19	14	118/85/167	209/77/5
20161122131122.230	54.349719	-117.226929	3.314	0.19	04	105/88/110	200/20/5
20161123142910.200	54.341541	-117.234619	3.265	0.19	00	108/55/165	206/77/35
20161130000822.780	54.33822	-117.239054	3.22	0.19	33	280/57/124	48/45/49
20161130190244.000	54.347457	-117.241178	3.325	0.18	12	111/84/172	201/82/6
20161103091323.390	54.345284	-117.239551	3.377	0.18	19	299/89/-176	208/86/-1
20161105210656.120	54.343404	-117.237207	3.274	0.18	12	93/72/160	189/71/19
20161122153038.120	54.349862	-117.227002	3.305	0.18	00	105/85/105	213/15/18
20161122220343.640	54.350146	-117.225781	3.32	0.18	04	98/82/113	206/24/19
20161123123120.370	54.352307	-117.226888	3.272	0.18	21	102/86/-170	11/80/-4
20161126090252.320	54.352266	-117.225472	3.34	0.17	00	95/80/110	210/22/27
20161122200055.560	54.341545	-117.248291	3.21	0.17	22	93/81/-172	1/82/-9
20161128070436.590	54.341073	-117.24834	3.257	0.17	13	96/85/172	186/82/5
20161128223548.560	54.338525	-117.238867	3.243	0.17	26	294/78/179	24/89/12
20161130184305.740	54.338245	-117.238973	3.216	0.17	39	287/42/133	286/42/132
20161130222325.340	54.345422	-117.239535	3.381	0.16	12	115/85/179	205/89/5
20161105181519.980	54.335706	-117.24882	3.281	0.16	16	94/72/178	184/88/18
20161110234432.560	54.341626	-117.248283	3.249	0.16	05	91/64/160	190/72/27
20161128013854.830	54.341504	-117.234757	3.26	0.16	03	292/53/166	30/78/37
20161129222818.920	54.341439	-117.234668	3.273	0.16	05	114/71/177	204/87/19
20161130121422.320	54.338371	-117.238949	3.211	0.16	27	283/50/132	48/55/51
20161130194507.580	54.34633	-117.238859	3.41	0.15	13	295/84/-179	204/89/-6
20161105213639.960	54.341614	-117.248315	3.232	0.15	07	93/67/166	188/77/23
20161129162829.850	54.34644	-117.238713	3.441	0.14	13	111/89/-168	20/78/-1
20161106004251.060	54.338318	-117.243278	3.219	0.14	07	266/74/161	1/71/16
20161110143528.270	54.338822	-117.243205	3.229	0.14	02	264/60/150	10/64/33
20161121232019.320	54.351388	-117.224984	3.303	0.14	06	96/63/144	204/58/32
20161124030727.390	54.343331	-117.248161	3.275	0.14	03	275/70/-143	170/55/-24
20161127192431.760	54.331999	-117.2493	3.205	0.14	14	276/57/143	28/59/39
20161129123135.980	54.338302	-117.238932	3.2	0.14	37	280/60/143	30/58/35
20161130202045.220	54.338228	-117.239095	3.219	0.14	28	274/21/146	274/21/145
20161130215417.720	54.338094	-117.239168	3.214	0.14	26	255/40/90	255/40/90
20161130224708.240	54.343294	-117.248055	3.271	0.13	16	267/88/168	357/78/2
20161127105310.170	54.341166	-117.248332	3.228	0.13	10	272/89/161	2/71/1

20161129040204.270	54.341418	-117.234741	3.255	0.13	17	289/88/-179	198/89/-2
20161130112405.080	54.347583	-117.241081	3.324	0.12	12	291/64/157	31/69/27
20161103093736.270	54.347579	-117.241048	3.327	0.12	20	290/74/164	24/74/16
20161103100858.620	54.345654	-117.239372	3.389	0.12	06	295/80/-177	204/87/-10
20161105165232.000	54.335929	-117.248787	3.281	0.12	00	96/60/180	5/90/-30
20161110093430.320	54.34578	-117.23925	3.388	0.12	08	296/87/-175	205/85/-3
20161122135417.350	54.345679	-117.239307	3.388	0.12	16	277/89/168	7/78/1
20161122155830.700	54.345597	-117.239404	3.375	0.12	25	98/78/177	188/87/12
20161122171549.980	54.338338	-117.238997	3.213	0.12	37	268/70/154	7/65/22
20161130191429.200	54.348523	-117.243441	3.272	0.11	13	91/81/175	181/85/9
20161101014855.150	54.340234	-117.248405	3.251	0.11	04	90/59/162	189/74/32
20161129090645.280	54.338387	-117.23894	3.201	0.11	09	92/68/162	188/73/23
20161130235036.120	54.34764	-117.241024	3.322	0.1	16	90/89/164	180/74/1
20161103095905.070	54.350049	-117.225871	3.319	0.1	03	91/83/177	181/87/7
20161123005237.000	54.349874	-117.225887	3.314	0.1	06	275/88/180	4/90/2
20161123041248.800	54.345658	-117.239347	3.382	0.09	16	94/87/170	184/80/3
20161105174947.600	54.333785	-117.24895	3.278	0.09	14	272/68/167	6/77/22
20161112171011.400	54.338729	-117.24327	3.211	0.09	00	105/88/109	200/19/6
20161119043353.720	54.349227	-117.227661	3.319	0.09	04	94/73/162	189/72/17
20161122092550.070	54.352482	-117.22535	3.336	0.09	06	95/75/168	188/78/15
20161123080243.390	54.352437	-117.225212	3.326	0.09	06	102/85/106	208/16/17
20161123172550.640	54.349662	-117.227002	3.322	0.09	11	90/63/160	189/72/28
20161123194545.800	54.347632	-117.241032	3.324	0.08	18	271/85/179	1/89/5
20161103113425.270	54.346672	-117.238534	3.442	0.08	03	105/89/110	197/20/2
20161106023359.070	54.338037	-117.248535	3.263	0.08	07	90/65/157	190/69/26
20161107112627.310	54.345561	-117.23422	3.234	0.08	33	95/80/165	187/75/10
20161122112111.190	54.345667	-117.239355	3.384	0.07	08	105/88/109	200/19/6
20161105145728.010	54.35186	-117.225431	3.33	0.07	04	95/78/175	186/85/12
20161122110303.780	54.34974	-117.226912	3.3	0.07	08	280/90/169	9/78/0
20161125002430.640	54.338314	-117.238957	3.206	0.07	27	102/88/110	197/20/5
20161130193138.840	54.348376	-117.24362	3.263	0.06	17	275/82/-179	184/89/-8
20161101033751.790	54.33807	-117.248519	3.261	0.06	15	268/38/165	9/80/52
20161107110551.530	54.352226	-117.225439	3.34	0.06	08	275/88/172	5/82/2
20161122213052.760	54.333	-117.248958	3.213	0.06	61	107/89/110	199/20/2
20161129104654.440	54.34683	-117.238346	3.349	0.05	19	93/75/161	188/71/15
20161106044609.820	54.338464	-117.243286	3.239	0.05	13	107/88/109	202/19/6
20161110103906.120	54.349255	-117.234855	3.308	0.05	19	95/80/115	205/26/22
20161122050253.390	54.341284	-117.248381	3.187	0.05	10	95/75/175	186/85/15
20161128151047.400	54.34554	-117.239478	3.387	0.04	15	105/85/110	208/20/14
20161105161550.920	54.337158	-117.243441	3.224	0.04	21	93/80/110	208/22/27
20161111091023.760	54.335193	-117.248861	3.278	0.04	16	102/88/110	197/20/5
20161113060754.000	54.346391	-117.238745	3.42	0.04	06	327/15/-123	180/77/-81
20161122043948.240	54.348104	-117.236825	3.426	0.04	09	94/83/-172	3/82/-7
20161122125019.270	54.345723	-117.245329	3.275	0.04	15	270/45/143	28/64/51
20161127020128.430	54.343237	-117.248096	3.233	0.04	19	95/80/117	203/28/21
20161128004222.370	54.341536	-117.248299	3.209	0.04	09	102/88/108	198/18/6
20161128045908.970	54.34742	-117.241211	3.325	0.03	17	95/80/110	210/22/27
20161103084525.280	54.346741	-117.238477	3.45	0.03	17	263/61/148	9/62/33
20161106025958.650	54.352153	-117.225382	3.328	0.03	00	91/86/-162	359/72/-4
20161123002249.700	54.352201	-117.226912	3.271	0.03	23	93/80/110	208/22/27
20161123023135.080	54.345671	-117.245321	3.268	0.03	09	95/83/110	203/21/19
20161127042324.690	54.341532	-117.248283	3.18	0.03	11	280/80/157	14/67/10
20161128101159.780	54.335474	-117.248853	3.281	0.02	18	95/80/175	185/85/10
20161110094624.840	54.337781	-117.248519	3.245	0.02	17	95/73/176	186/86/17
20161110222605.960	54.351847	-117.225513	3.323	0.02	00	103/90/111	193/21/0
20161121232043.560	54.351847	-117.225431	3.32	0.02	00	270/79/167	2/77/11
20161122131303.530	54.344718	-117.247949	3.251	0.02	12	108/85/105	216/15/18
20161125045326.380	54.341309	-117.234741	3.269	0.02	22	95/75/168	188/78/15
20161130183127.880	54.345622	-117.239299	3.361	0.01	14	95/78/175	186/85/12
20161105195356.440	54.338505	-117.248519	3.254	0.01	18	104/88/109	199/19/6
20161108172656.100	54.34672	-117.238493	3.422	0.01	16	107/89/110	199/20/2
20161122041646.330	54.349849	-117.226986	3.329	0.01	05	103/88/110	198/20/5
20161123130253.500	54.340828	-117.240243	3.02	0.01	20	98/83/110	206/21/19

20161129035338.530	54.346871	-117.245776	3.218	0	18	95/80/110	210/22/27
20161101180516.600	54.337895	-117.24856	3.26	0	20	292/88/-110	196/20/-5
20161108054435.090	54.350122	-117.227165	3.321	0	04	95/89/151	185/61/1
20161122091356.950	54.349988	-117.227344	3.324	0	07	99/89/166	189/76/1

Appendix G: Supplementary Material

DiTingMotion: https://github.com/mingzhaochina/DiTing-FOCALFLOW

Full ToC2ME Earthquake Catalog: http://doi.org/10.5281/zenodo.6826326

DiTingMotion picks per station waveform plots:
https://drive.google.com/drive/folders/1zRqcm8vv3KL1ZwvzjNWHhxiGCVCTYWna?usp=sharing